RICE UNIVERSITY

In Situ Quantitative Mechanical Characterization and Integration of One Dimensional Metallic Nanostructures

by

Yang Lu

A THESIS SUBMITTED
IN PARTIAL FULFILLMENT OF THE
REQUIREMENTS FOR THE DEGREE

Doctor of Philosophy

APPROVED, THESIS COMMITTEE:

Dr. Jun Lou, Chair
Assistant Professor of Mechanical Engineering and Materials Science

Dr. Pulickel M. Ajayan
Benjamin M. and Mary Greenwood Anderson Professor in Engineering
Materials Science and Nanotechnology

Dr. Boris I. Yakobson
Karl F. Hasselmann Chair Professor of Mechanical Engineering and Materials Science
Professor of Chemistry

Dr. Qianfan Xu
Assistant Professor of Electrical and Computer Engineering

HOUSTON, TEXAS
2010

ABSTRACT

In Situ Quantitative Mechanical Characterization and Integration of One Dimensional Metallic Nanostructures

by

Yang Lu

One dimensional (1-D) metallic nanostructures (e.g. nanowires, nanorods) have stimulated great interest recently as important building blocks for future nanoscale electronic and electromechanical devices. In this thesis work, gold and nickel nanowires with various diameters were successfully fabricated, and two dedicated platforms, based on (1) a novel micro mechanical device (MMD) assisted with a quantitative nanoindenter and (2) a TEM-AFM sample holder system, were developed and adopted to perform in situ tensile tests inside SEM and TEM on samples with diameter ranging from a few nanometers to hundreds nanometers. Size-dependent mechanical behavior and different fracture mechanisms of gold nanowires had been revealed and discussed. In addition, we discovered cold welding phenomenon for ultrathin gold nanowires (diameter < 10nm), which is anticipated to have potential applications in the future bottom-up integration of metallic 1-D nanostructures and next-generation interconnects for extremely dense logic circuits.

Acknowledgements

I am deeply grateful to my thesis advisor, Professor Jun Lou, for his mentoring throughout my PhD study at Rice. It is his invaluable guidance that allows me to reach this point of my academic career. He has generously provided everything I could ever expect. Constantly, he shares his unusual wealth of knowledge and experience; he encourages to motivate; and he criticizes to perfect. It is truly a privilege I can have him as my advisor and his mentoring will be a lifelong fortune for me.

I would also like to thank the other members, Prof. Pulickel M. Ajayan, Prof. Boris I. Yakobson and Prof. Qianfan Xu, of my thesis committee for reviewing this work, and more importantly, for kindly supporting me over various stages of my study and research at Rice. Their interest and appreciation gave me incredible impetus and confidence to carry on this research.

During the four years at Rice, I have the opportunity to learn from many other distinguished scholars, including Prof. Enrique V. Barrera, Prof. Rex B. McLellan, Prof. Andrew J. Meade, Dr. Peter Loos, Dr. Robert Vajtai, Dr. Wenhua Guo, Dr. Angelo Benedetto and many more. I could not list them all, but I thank them all.

In addition, I feel very lucky to have the opportunity to collaborate with Dr. JianYu Huang at Center for Integrated Nanotechnologies (CINT), Sandia National Laboratories and Prof. Sarah E. Bondos Department of Molecular and Cellular Medicine, Texas A&M Health Science Center. Dr. JianYu Huang of CINT generously provides access to the *in situ* HRTEM faculties used throughout this work and Dr. Bondos's Ubx fibers opened the door for my biomaterial research. I benefit tremendously from their rich experience and unique insight and their help on my research is sincerely appreciated.

During the past four years, I would like to thank my colleagues in Lou research group, Yogeeswaran Ganesan, Hao Lu, Yongjie Zhan, Cheng Peng, Jiangnan Zhang, Pei Dong, Phillip E. Loya, Yezeng Cheng, Sina Najmaei, Zheng Liu and more, for your generous help in many ways. They assisted and collaborated with me in various aspects and there was so much fun to stay in the lab days and nights because of them.

Last but certainly not least, it is my family who has always been there for me with unconditional love and support. This dissertation is dedicated to them. To my parents, I simply could not owe more. They bring me to the world and make me who I am. I am proud of them as they are proud of me, or maybe more.

Table of Contents

List of Figures

List of Tables

Chapter 1

Introduction

The mystery of measured mechanical strength for crystalline material lower than their predicted theoretical value has long been attributed to the dislocation mediated plastic deformation leading to the final failure [1]. Namely, the plastic deformation of crystalline material is thought to be controlled by dislocation processes such as multiplication, storage and interactions. When the volume of a crystalline sample gets smaller and smaller, such as in micro- and nano-scale metallic structures, two important changes start to emerge. The first one is the lower probability of pre-existing dislocations and less available dislocation sources. The second one is the increasing difficulty for dislocation multiplication, storage and interaction, due to the geometrical constraints. As a result, the conventional dislocation mediated plasticity is very likely no longer the dominant deformation process in geometrically-confined metals (such as metallic nanostructures) and contributions from other deformation mechanisms such as dislocation nucleation [2-4], twinning [5-7], interactions between twin and dislocations [5, 7] and stress assisted phase transformation [8-9] become increasingly important. These nanoscale deformation mechanisms represent a completely different paradigm compared to bulk scale dislocation multiplication and interaction based plastic deformation mechanisms.

It is also well recognized that many other mechanical properties of materials deviate largely from their bulk counterparts when characteristic dimensions become sufficiently small [10]. Size-dependence in mechanical properties for metals at micron scale has been

well documented [11-15] in recent years. Size dependent plasticity and fracture behaviors of one-dimensional (1-D) metallic materials, especially at the nanometer length scale, have generated great interests [3, 8, 15-19] because of their important effects on assembly, performance and reliability of functional nano-electronic and nano-electromechanical-systems (NEMS) devices. Size-dependent mechanical study of 1-D metallic nanostructures also possess exciting potentials for revealing the fundamental mechanisms responsible for physical origins of size effects in many important processes such as deformation, fracture and fatigue, as the length scale approaches atomic spacing. Therefore, the overall goal of this research is to systematically probe mechanical behaviors of 1-D metallic structures at nanometer length scale (with diameters from a few nanometers to hundreds of nanometers) using advanced *in situ* quantitative characterization methodologies. Systematic studies of samples with different diameters using advanced *in situ* characterization tools capable of observing and following the initiation and evolution of these mechanical processes provide valuable insights into discoveries of how atomic structures could be manipulated in a predicable manner to enable development of new materials and novel functional structures, with performance close to ideal strength and high ductility and facture resistance which could function under extreme conditions with little property (mechanical, electrical..) degradation.

1.1. One Dimensional Metallic Nanostructures

Due to their interesting electrical, chemical, magnetic, optical and mechanical properties, one dimensional (1-D) nanoscale materials and structures (Figure 1-1), such as nanowires [20-26], nanobelts [25, 27-28], nanorods [29-31] and nanotubes [26, 32-35],

have been extensively investigated in the past two decades and widely considered as ideal candidates to be used in miniaturized devices such as sensors/detectors, actuators, electronic/optoelectronic devices, solar-cells/power generators, carriers of drugs [20-35].

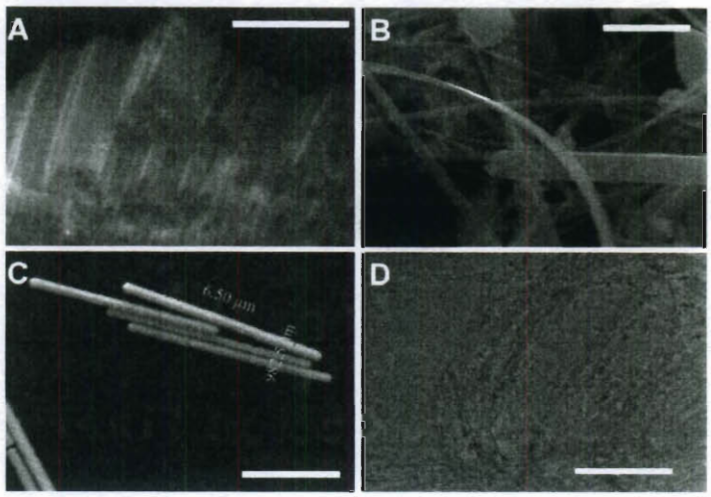

Figure 1-1 One-dimensional nanomaterials in our lab: (a) TiO_2 nanotubes (scale bar 1um); (b) copper nanobelt (scale bar 2um); (c) gold nanorods (scale bar 3um); (d) single-wall carbon nanotubes (SWCNTs) (scale bar 200nm)

In particular, metallic 1-D nanostructure, such as metallic nanowires (NWs) and nanorods (NRs), with diameters ranging from tens to hundreds nanometers, have stimulated great interest recently as important building blocks for future nanoscale electronic and electromechanical devices in various applications [36-38]. Recently, as current lithography for micro/nanofabrication industry may encounter a barrier when the critical feature size was approaching the limit (~20nm) [39], "ultrathin" metallic nanowires [40], such as gold [41-44], silver [45-47], tellurium [48-49] palladium and platinum [49-50] nanowires with diameters less than 15nm, have been discovered and expected to potentially satisfy the stringent nanoelectronics requirements. Especially,

ultrathin gold nanowire with diameter less than 10nm has drawn considerable interest and been widely considered as promising candidate for next-generation interconnects and as active components in future nanoscale devices [38, 41, and 51], owing to its excellent electrical and mechanical properties as well as desired chemical inertness (Figure 1-2).

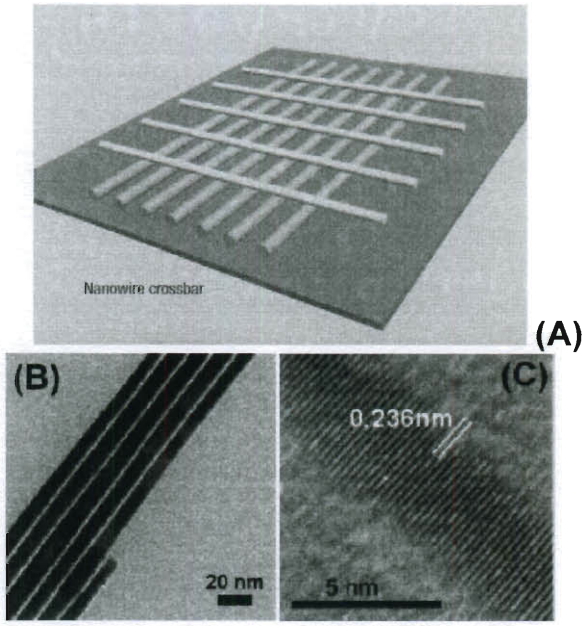

Figure 1-2 Nanowire crossbar memory and ultrathin gold nanowires: (a) schematic illustration of a nanowire crossbar memory [38]; (b) TEM image of six ultrathin gold nanowires with diameters ~9nm [41]; (c) high resolution TEM image of an individual ultrathin gold nanowire with <111> growth orientation [41]

In addition, the novel physical properties also make 1-D metallic nanostructures ideal candidates for other important applications in biological/chemical sensors [52-53], gene/drug delivery [54], photonic/waveguiding [55-56], and energy conversion devices [57]. For example, short gold nanowires (also known as "gold nanorods") have been extensively studied for their unique surface plasmon resonance and photothermal properties and already used in biosensing, molecular imaging and selective photothermal

therapy [58]. While for nickel nanowire, due to its unique magnetic properties, individual nickel nanowire can be precisely controlled and manipulated by external magnetic field, as shown in Figure 1-3, to serve various applications such as drug delivery and cell manipulation [59-61].

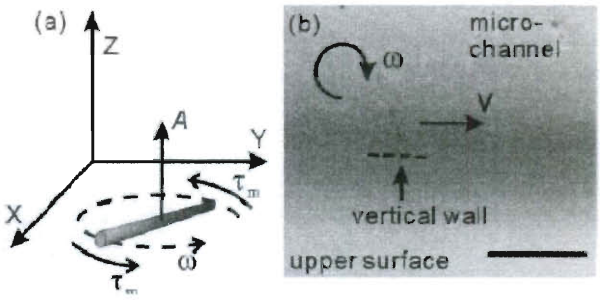

Figure 1-3 Manipulation of nickel nanowires with controllable magnetic field: (a) Schematic of a Ni nanowire rotating horizontally in the X-Y plane; (b) A Ni nanowire is propelled near a vertical wall (The scale bar is 50 μm). [60]

Furthermore, by using their different surface binding effects for specific chemical or biological targets, researchers combined multiple metal segments into single 1-D metallic nanostructures (such as gold and nickel bimetal nanowires) to achieve remarkable new features that can be used in novel biomedical applications [62-64], such as controllable gene delivery [62] shown in Figure 1-4.

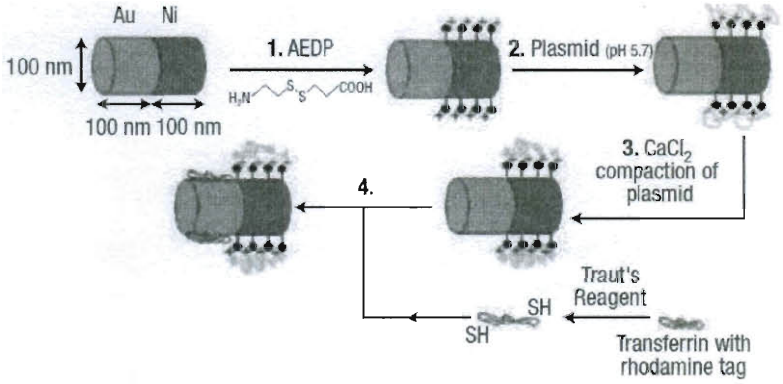

Figure 1-4 Illustration of multicomponent nanorod functionalization: spatially selective binding of DNA plasmids and transferring to Au/Ni multicomponent nanorods [62]

However, the ability to achieve the full potential of aforementioned 1-D metallic nanostructures and their related fascinating applications is ultimately limited by how these one-dimensional building blocks will behave at relevant length scales, in particular, their mechanical performance and reliability.

1.2. Size-Dependent Mechanical Behavior

In order to fully understand size effects in plastic deformation and fracture of low dimensional metallic nanomaterials and their related structures, it is necessary to review past work on metal whiskers, cylindrical pillars, micro-wires and nanowires. Early studies have shown that iron and copper whiskers with diameter down to a few micrometers have yield strengths that are over ten times that of the corresponding bulk materials [65]. This effect was interpreted as a decreased defect (dislocations) density resulting from reduced wire sizes [66]. In 1994, Fleck et al. [67] revisited this classical

experiment by performing tension and torsion experiments on copper wires of different diameters at micro-scales and observed strong size effects of yielding in torsion experiments but negligible effects in tension experiments. These observations were explained by non-local effects introduced by inhomogeneous deformation of torsion, and have stimulated large interests in the mechanics and materials community to investigate the effects of strain gradients on size dependent plasticity behavior and promoted the development of phenomenological strain gradient plasticity (SGP) theories [67-70]. The apparent discrepancy in tensile results of copper whisker [65] and copper wires [67] was attributed to the extremely low densities of stored dislocations in whiskers as a function of whisker diameter due to processing, which promoted dislocation initiation mediated yielding behavior as compared to dislocation multiplication induced yielding behavior in copper wires.

To further investigate this hypothesis and also to uncover the transitions between these two mechanisms without the complications of strain gradients (loading conditions such as indentation, bending and torsion) and grain boundary (microstructural constraint) induced size effects, Nix group [15, 17, 18] and other researchers [71] recently performed a series of elegant experiments using micro-machined single crystal gold and nickel pillars with diameters ranging from a few microns to hundreds of nanometers that were uni-axially compressed by a flat nanoindenter punch. Again, it showed strong size effects with much higher yield stress for smaller pillars than the larger ones and their bulk counterpart without the presence of strain gradients (Figure 1-5).

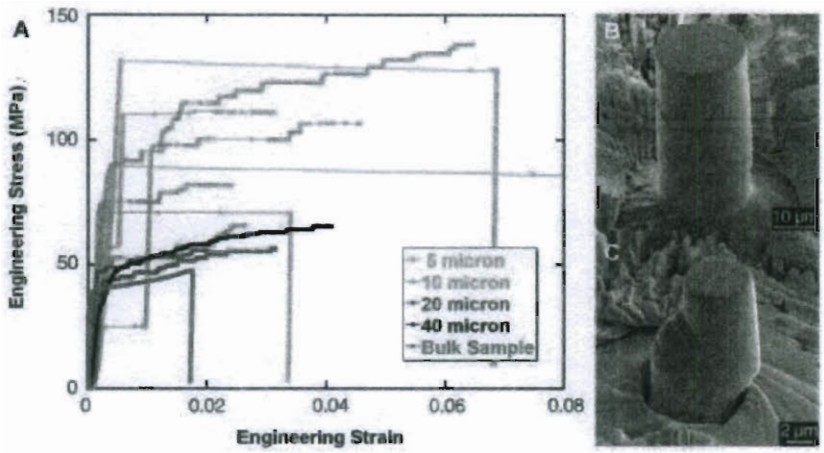

Figure 1-5 Size effect in mechanical behavior for nickel pillar under compression loading: (a) Stress-strain curves for sample ranging from 40 to 5μm in diameter, as well as the stress-strain curve for a bulk single crystal sample; (b) A scanning electron micrograph (SEM) image of a 20μm-diameter microsample tested to ~4% strain; (c) A SEM image of 5μm-diameter microsample after testing, where the sample achieved ~19% strain. [15]

Based on these experiments, a conceptual postulation of "dislocation starvation" [18] was thought to be responsible for this apparent size dependent behavior, based on Gilman's (1953) description of dislocation multiplication [72] which requires a critical traveling distance of dislocation before it can replicate itself. The smaller the pillar (especially below this critical length scale), the lower the probability of dislocation multiplication process will be, resulting higher yield stress which needs to be sustained by continuous dislocation nucleation events. Although it seems to be a plausible explanation to some observed experimental results, many important questions such as the exact type and location of dislocation sources, mechanisms by which mobile dislocations

interact with defects including processing induced surface defects and pre-existing dislocations, existence and mechanisms of hardening behavior especially under reversed loading, strain rate effects on yielding and flow behavior, as well as understanding of mechanism transitions from dislocation substructure to surface dislocation nucleation [2] remain unclear at the moment. Additionally, there have been concerns raised regarding to the sample preparation technique [73-74], experimental details [71, 75-76] for these micro-pillar compression experiments. Meanwhile, existing experiments on metal nanowires have largely focused on bending of suspended nanowires using AFM [16, 77-78] and nanoindenter [79] which is non-ideal to identify underlying mechanisms as discussed earlier. Therefore, it is very important to develop robust uni-axial testing techniques for metal nanowires with well controlled crystalline structures and geometries, to unveil many important deformation and damage mechanisms at the nanoscale.

1.3. Quantitative Mechanical Testing of 1-D Nanostructures

Before designing and developing systematic mechanical testing methodologies for 1-D metallic nanostructures, it is necessary to review and understand the three major factors affecting size effects in mechanical behavior of metals: *microstructural constraint*, *geometry constraint* and *loading configuration*. Among these, the *microstructural constraint* is due to grain size effects described by the famous "Hall-Petch" relationship (the smaller the grain size, the stronger the materials) or the inversed "Hall-Petch" relationship for grain size of a few nanometers which have been extensively studied for bulk nanocrystalline materials [80-81]. Twin boundary effects [82-83] and phase transformation effects [84] are also important mechanisms in this category. The

geometry constraint is normally due to substrate/thin film interface and/or free surface effects, such as sample dimensions effects (wire diameters, film thicknesses, indenter penetrating depth etc.). It has recently been suggested that similar "Hall-Petch" type of relationship (with slope of -0.6 to -0.8 for FCC metals as compared to -0.5 of the regular "Hall-Petch" slope) also exists when one plots the normalized yield strength against the wire/pillar diameter [71]. A significant decrease in this slope has been predicted for nanowires with diameters below a few tens of nanometers due to the transition from collective dislocation dynamics to surface dislocation nucleation controlled plasticity by atomic simulations [4]. Finally, the proven effects of *loading configuration* or imposed strain gradient (i.e. in case of indentation loading, bending or torsion configurations) have been shown for metallic samples at meso and micron scales [14, 67, 85 and 86]. To get a clear understanding of their individual contribution and therefore unambiguous underlying mechanisms, experiments need to be carefully designed to decouple the influences of the three factors whenever it is possible.

For the first two factors, the template-based synthetic approach [60] was chosen for gold (Au) and nickel (Ni) nanowire fabrication for better control of the physical dimensions and crystalline structures (as discussed in detail in Chapter 2). This versatile method uses a porous membrane, such as anodized aluminum oxide (AAO) templates with diameters ranging from 20nm-300nm, as a scaffold to precisely control the size (including diameter and length) of one-dimensional wires made of many different types of materials. Later on, chemically synthesized ultrathin gold nanowires [41] were also used in this study, as they have with much smaller diameters and same <111> crystalline

orientation as the larger gold nanowires synthesized by the template method (see Chapter 2).

On the other hand, *loading configuration* poses more challenges as the traditional tensile testing for bulk metal samples cannot be simply adopted for nanowires due to their extreme small sample sizes, although significant progresses had been made in the past two decades for testing nanomaterials in various loading configuration. Here we firstly review some earlier experiments on quantitative tests of individual 1-D nanostructures with different loading geometries rather than tensile testing:

Resonance and Vibration

Due to the extreme small sizes of 1-D nanomaterials, direct mechanical testing was rather difficult. Earlier researchers developed some indirect measurements, for example, vibration test and resonance test. Treacy et al. [87] estimated the Young's modulus of multi-wall carbon nanotubes (NWCNTs) by measuring the amplitude of their thermal vibrations during in situ TEM imaging (Figure 1-6). In the test, the nanotubes were attached to the edge of a hole in 3mm-diameter nickel ring for TEM observation, with one end clamped and the other end free. The blurring of free end was monitored as a function of temperature on the nanotube. The Young's modulus was estimated from the envelop of the thermal vibration. On the other hand, based on mechanical resonance of the nanotube, Poncharal et al. measure the Young's modulus of MWCNTs [88]. In their experiment, AC voltage was applied to cause a time-dependent deflection. The elastic modulus was then estimated from the observed resonance frequencies.

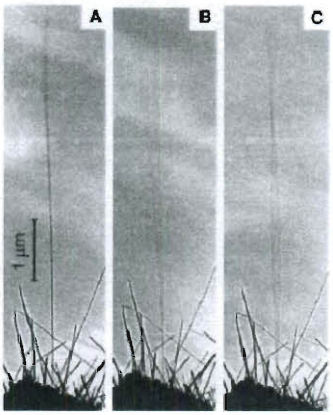

Figure 1-6 Multi-wall carbon nanotube resonance test: Dynamic responses to alternate applied potentials, (a) absence of a potential, (b) at fundamental mode, and (c) at second harmonic mode [88]

One of important applications of the nano-resonance is nanobalance. By attaching the nanoparticle on the tip of the free end of the nanoresonator, Huang et al. [89] successfully measured the mass of a nanoparticle with very high accuracy. Actually, nanoresonator balance had the highest resolution in nanoscale mass measurement.

Bending and Curvature

For direct measurement, one of the difficulties is to precisely align the sample. So by just fixing one end and performing mechanical actuation on another end, the difficulty of direct mechanical testing can be significantly reduced. So bending or curvature tests were of most popular measurement techniques in earlier years. For nano bending test, atomic force microscopy (AFM) is widely used. Generally, one can use atomic force microscope (AFM) to manipulate the 1-D nanostructure sample, such as CNT, and bend it with its cantilever. The AFM was used on contact mode, and the tip of probe was used to apply lateral force at location along the tube to produce bending effect.

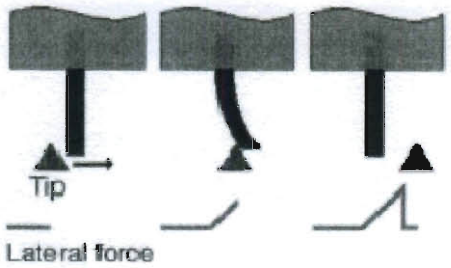

Figure 1-7 using AFM to conduct bending test on a nanotube [90]

In Figure 1-7, we showed the concept how Wong et al. [90] measured the Young's modulus, strength and toughness of NWCNTs and SiC nanorods using AFM in lateral force mode. In their tests, nanotubes or nanorods were dispersed randomly on a flat surface and pinned to the substrate by means of microfabricated patches. Then AFM probe select those well-fixed nanostructures and bended them transversely. Although this method is relatively easier to handle, it introduced the effect of adhesion and friction from substrate. Later on Walters et al. suspended the nanotube over a microfabricated trench and deflected the nanotubes vertically [91].

Compression and Buckling

Aforementioned indentation/compression tests on micro- and submicron- sized metal pillars can be considered as a type of compression tests. Compression (or buckling) test, while fixing one end and deforming another end along the longitudinal direction, is more difficult than above bending/curvature tests. Shen et al. [92] used AFM to perform a compression test on MWCNTs. However, unlike metal pillars, CNT (or other sample with high aspect ratio), to maintain loading radical is very challenging and the accuracy then will be a problem in these tests using AFM cantilever. Recently, due to the development of nanoindenter, people can conduct better compression (buckling) tests on

the nanotubes with this new tool. Waters et al. [93] conducted the first shell buckling test on individual free standing MWCNT, by axial compression using a nanoindenter (Figure 1-8).

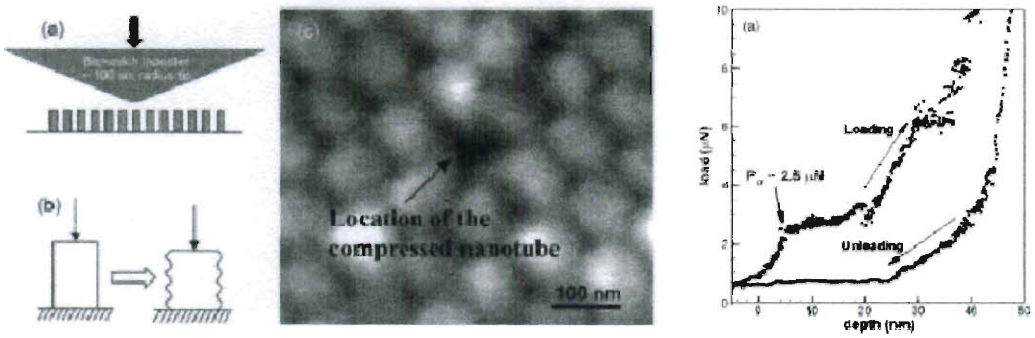

Figure 1-8 Shell buckling test of MWCNT with a nanoindenter: (a) illustration of the test;(b) a CNT being deformed; (c) the SEM image of a compressed nanotube; (d) the resultant indentation depth vs. load curve [93]

Deflection and Torsion

Once individual 1-D nanostructure sample was clamped firmly on both ends, which was also challenging, deflection and torsion test could then be made possible. Wu et al. (Figure 1-9) performed systematically study on the mechanical properties by deflecting the center of gold nanowires which were crossed a trench and clamped by FIB on both ends [16].

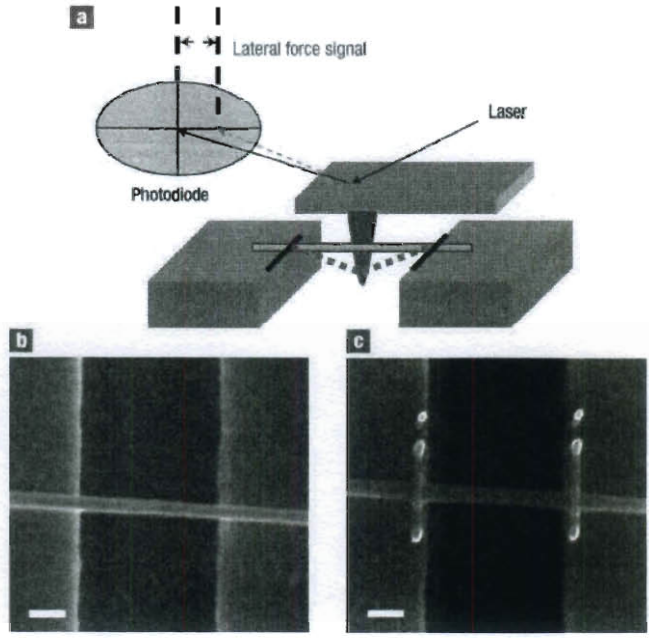

Figure 1-9 Deflection of a gold nanowire with AFM: (a) Schematic of fixed wire in a lateral bending test with an AFM tip; (b) SEM image of a 200-nm Au nanowire suspended on a trench; (c) SEM image of a Au nanowire mechanically fixed by electron-beam-induced deposition of Pt lines. The scale bars on both images are 500 nm. [16]

On the other hand, Williams et al. [94] introduced a microfabricated device which offers the possibility to conduct torsion test. They started with depositing metal pads by photolithography and alignment marks by electron beam lithography (EBL). The dispersion of the MWCNTs onto surface followed. Under scanning electron microscope (SEM), the location of the paddles can be determined carefully. The suspended paddles were deflected with an AFM installed inside the SEM (Figure 1-10). With the combination of AFM and SEM, applied force and paddle deflection could be measured directly. Assuming no bending, one could calculate the torque and corresponding rotation of nanotubes (However, apparently, applied force by AFM did introduce bending effect).

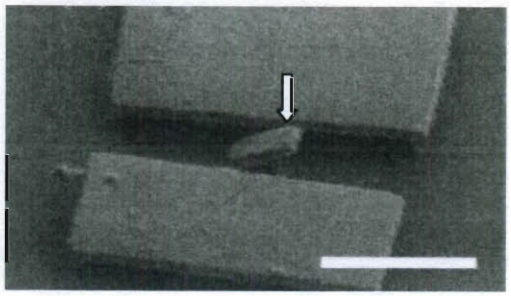

Figure 1-10 Torsion test on a nanotube with a paddle attached at the center (the white arrow indicating the loading direction by an AFM cantilever [94]

1.4. Design and Development of *In Situ* Tensile Test

In addition to their compromised loading configuration, aforementioned quantitative mechanical testing of 1-D nanostructures were primarily carried out either *ex situ* or with low resolution microscopy techniques, such as SEM or AFM. For metallic nanowire testing, these methods generally lack real time monitoring on their crystalline/atomic structure, which did not permit a one-to-one correlation between mechanical data and internal structural evolution. Recently, a few *in situ* mechanical characterizations of individual nanowires with diameters from tens to hundreds of nanometers were realized inside TEM, under various loading geometries, such as bending [95], buckling [96], and compression [97]. However, tensile testing remains the most efficient and easy-to-interpret testing method for measuring intrinsic mechanical properties and investigating fracture behavior of 1-D metallic nanostructures. On the other hand, in situ tensile testing on metallic nanowires poses significant challenges due to difficulties associated with sample clamping, alignment and accurate measurements of load and displacement.

One solution to perform *in situ* tensile tests on 1-D nanostructure is to develop micro electromechanical systems (MEMS)-based testing platforms for such a tensile test while the MEMS device itself could be small enough to fit into a TEM. Researchers had already developed various MEMS devices to perform in situ tensile tests on metallic (e.g. Pd, Cu, Co) nanowires/nanowhiskers and carbon nanotubes (Figure 1-11) [98-101], biological fibrils [102], and gold nano thin film [103]. However, these MEMS platforms relied on quite complicated setups that involved electro- or thermo-mechanical coupling and capacitance-based load measurement; its implementation is thus both expensive and challenging. Recently we designed and developed a simple micro mechanical device (MMD) [104-105], which was based on a pure mechanical "push-pull" actuation mechanism and relied on an independent nanoindenter to measure the load and displacement. Our simple design can significantly help minimize the sources of errors and reduce the cost for the device fabrication. We used this system to characterize gold and nickel nanowires with diameters ranging from tens to hundreds of nanometers, as described in Chapter 3.

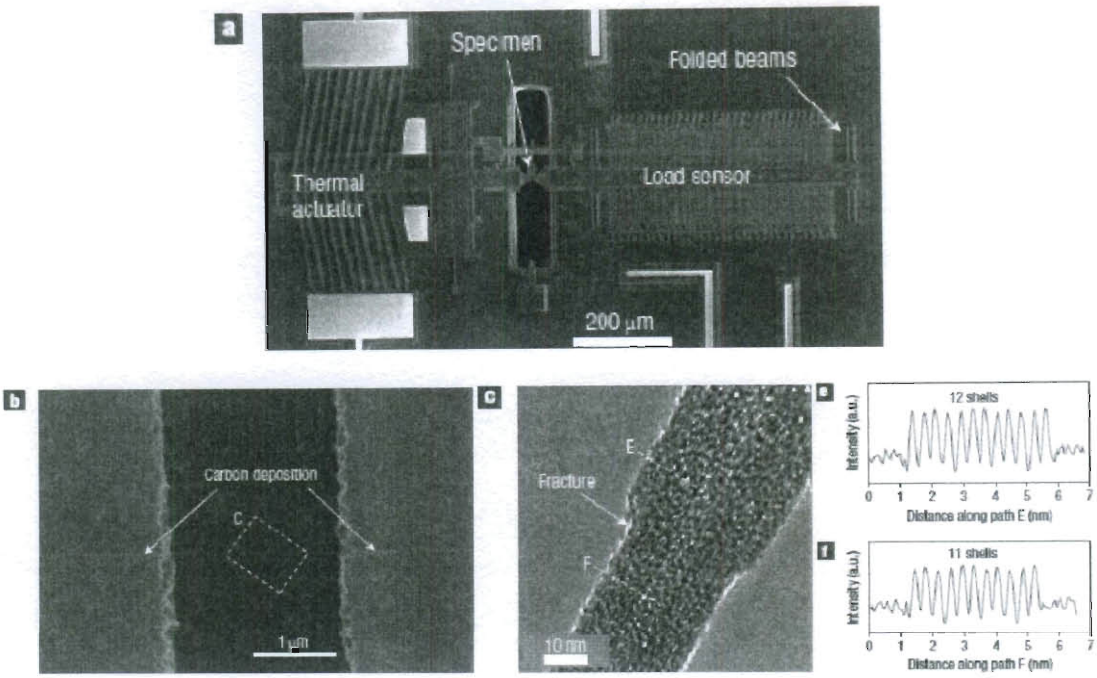

Figure 1-11 MEMS based in situ tensile testing system: (a) SEM image of the MEMS arrangement used to test the mechanical properties of various carbon nanotubes; (b) SEM image of a multiwalled nanotube bridging the gap between the actuator (left) and the load sensor; (c) TEM image of sample 1 after fracture. Paths E and F were used to create intensity profiles (e and f) on either side of the fracture to verify that only a single shell failed. [102]

On the other hand, testing metallic nanostructures with sub-10nm diameter poses even more challenges, due to the difficulties associated with exceedingly small sample size. Due to the difficulty to manipulate and clamp sample inside TEM, early researchers had to prepare samples *in situ* by using either mechanically controllable break junction technique (MCBJT) (Figure 1-12) [106] or nanometer tip-substrate [107] / tip-tip [108] contact-then-withdraw technique to form nano-sized metal junction samples. Unfortunately the crystalline structure and orientation of these quasi-nanowire samples

prepared by these methods were not well-controlled, and sample diameters were non-uniform (ranging from a few Armstrong to a few microns). These drawbacks hindered quantitative characterization and understanding of the deformation and fracture mechanisms for metals at the ultra small scale.

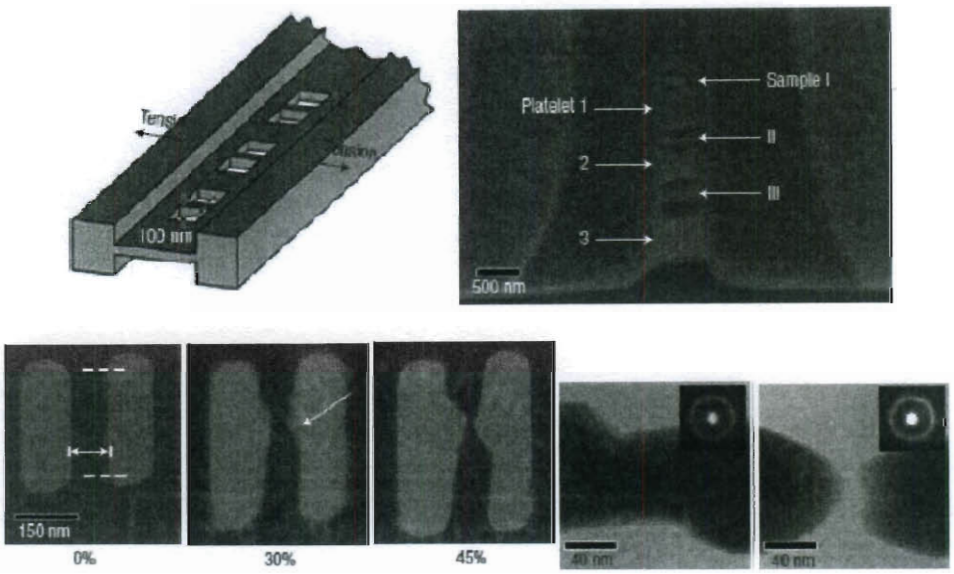

Figure 1-12 Mechanically controllable break junction technique (MCBJT) [106]

In this thesis, we will present the first *in situ* quantitative tensile tests of ultrathin gold nanowires by using the dedicated TEM-AFM sample holder system. Rather than pulling randomly formed nanosized gold nano-junction, we successfully clamped individual pre-fabricated free-standing nanowires with well-controlled crystalline structures and orientations onto the AFM cantilever which acted as the force sensor, and performed quantitative tensile tests directly inside a HRTEM. In addition, unlike typical sample clamping methods involving focus ion beam (FIB) deposition which may introduce significant surface contamination [109] and local heat-induced spot welding which could potentially damage the initial sample structures and morphologies [110-

112], we successfully used recently discovered cold welding phenomenon for ultrathin gold nanowires (Chapter 5), managed to overcome aforementioned difficulties and performed robust individual nanowire picking-up and clamping procedures repeatedly, allowing systematic study on tensile and fracture behaviors of ultrathin gold nanowires (Chapter 4).

1.5. Organization of the Thesis

In summary, with the MMD (micro mechanical device) and TEM-AFM platforms, we are now able to performed *in situ* tensile tests in SEM and TEM for metallic (Au, Ni) nanowires with a wide range of diameters (from a few nanometers to hundreds of nanometers) and well-controlled crystalline structures, which allows the systematic study on size-dependent mechanical behavior of 1-D metallic nanostructures. The organization of the thesis will be:

In Chapter 2, gold and nickel nanowire samples with different diameters and well controlled crystalline structures as well as some novel 1-D nanostructures (e.g. porous gold nanorods), were successfully synthesized via template-assist electrochemical deposition method.

In Chapter 3 and Chapter 4, *in situ* tensile mechanical study of gold and nickel nanowires with different diameters was presented. In particular, we showed the development and usage of the micro mechanical devices for *in situ* tensile testing of gold and nickel nanowires with larger diameters (~100-300nm) in SEM and TEM in Chapter 3. By using the dedicated TEM-AFM platform, *in situ* tensile tests of ultrathin gold nanowires (diameter less than 15nm) were carried out and discussed in Chapter 4.

In Chapter 5, cold welding of ultrathin gold (and silver) nanowires and its application in future integration of 1-D nanostructures was demonstrated. Quantitative *in situ* mechanical and electrical measurements were also carried out to examine the welding quality.

Conclusion and future work were discussed in the Chapter 6.

Chapter 2

Fabrication of 1-D Metallic Nanostructures

2.1. Template-Assist Electrodeposition of Metallic Nanowires with Different Diameters

Metallic nanowires, such as gold and nickel nanowires with different diameters, were fabricated by electro-chemical deposition using nanoporous anodic aluminum oxide (AAO) templates [113-114]. Via careful control of the anodization conditions and processes [115], AAO templates with ordered channels having uniform pore size ranging from tens of nanometers to hundreds nanometers were fabricated. The channel depths (thicknesses of AAO templates) were usually about 40-50um, which will be the upper limit of the nanowire lengths. Room temperature electro-chemical deposition of metallic nanowires, such as nickel nanowires, into the AAO templates was accomplished using a two-electrode system (Figure 2-1) with a graphite counter electrode at room temperature, under a DC power supply (Extech^{TM}, using voltage around 0.8-1.5V, current about 0.01A).

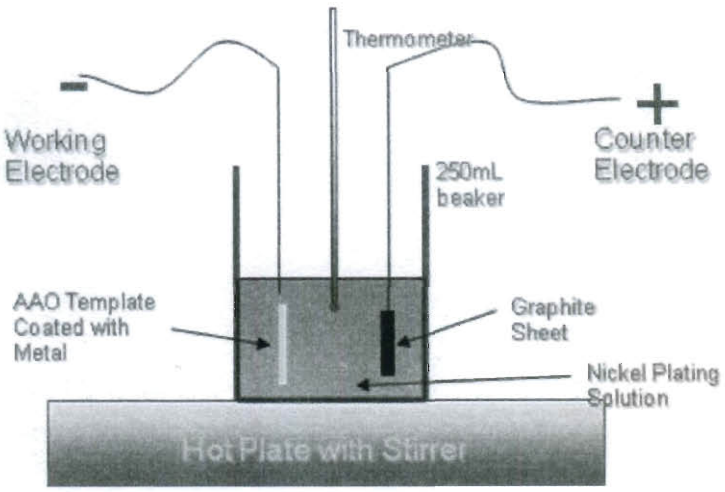

Figure 2-1 Experimental setup for template-assisted electrodeposition of nickel nanowires

Before deposition, a layer of silver (1-2μm) was sputtered on one side of the AAO membrane, which served as the working electrode. The reason to choose silver was because it could be easily etched by nitric acid. The silver target was obtained from ESPI-metals™ Company (4N purity). The AAO membrane was mounted on a copper plate using insulating electrical tape with the conductive metal-coated side facing the copper. The tape covered the remaining copper plate and prevented unwanted deposition. The electrolytes used for gold and nickel were commercially available electroplating solutions (Technic™): For nickel plating solution, the Watts Nickel Pure™ which containing $NiSO_4$ and $NiCl_2.6H_2O$ was used; for gold plating solution, the Orotemp™ plating solution, containing $K[Au(CN)_4]$, was used.

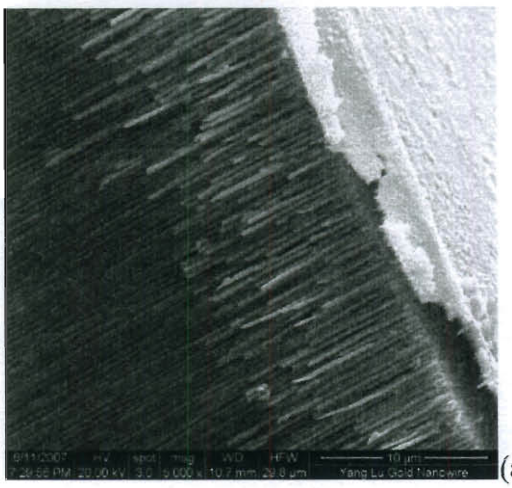
(a)

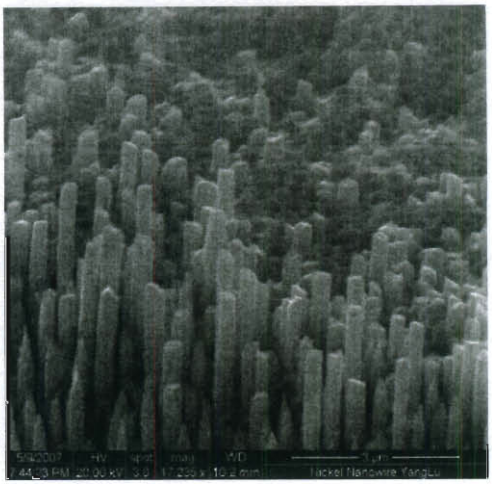
(b)

Figure 2-2 Growth of gold and nickel nanowires inside AAO channels: (a) cross-section view of Au NWs inside AAO channels (the "white" silver back-coating layer acting as the working electrode); (b) top view of Ni NWs grown out from AAO template

Figure 2-2 shows the growth of nanowires inside AAO channels. Once voltage was applied, metal deposited within the channels from the bottom, where silver thin film was coated and served as working electrode. Since the electric current was kept constant, the length and the diameter of the as-made nanowires could be precisely controlled by the electroplating time and the pore size of the AAO template, respectively. For example, in present work, we successfully made nickel nanowires with diameter ranging from ~30-300nm in diameter, with average lengths up to 30-40μm, as shown in Figure 2-3.

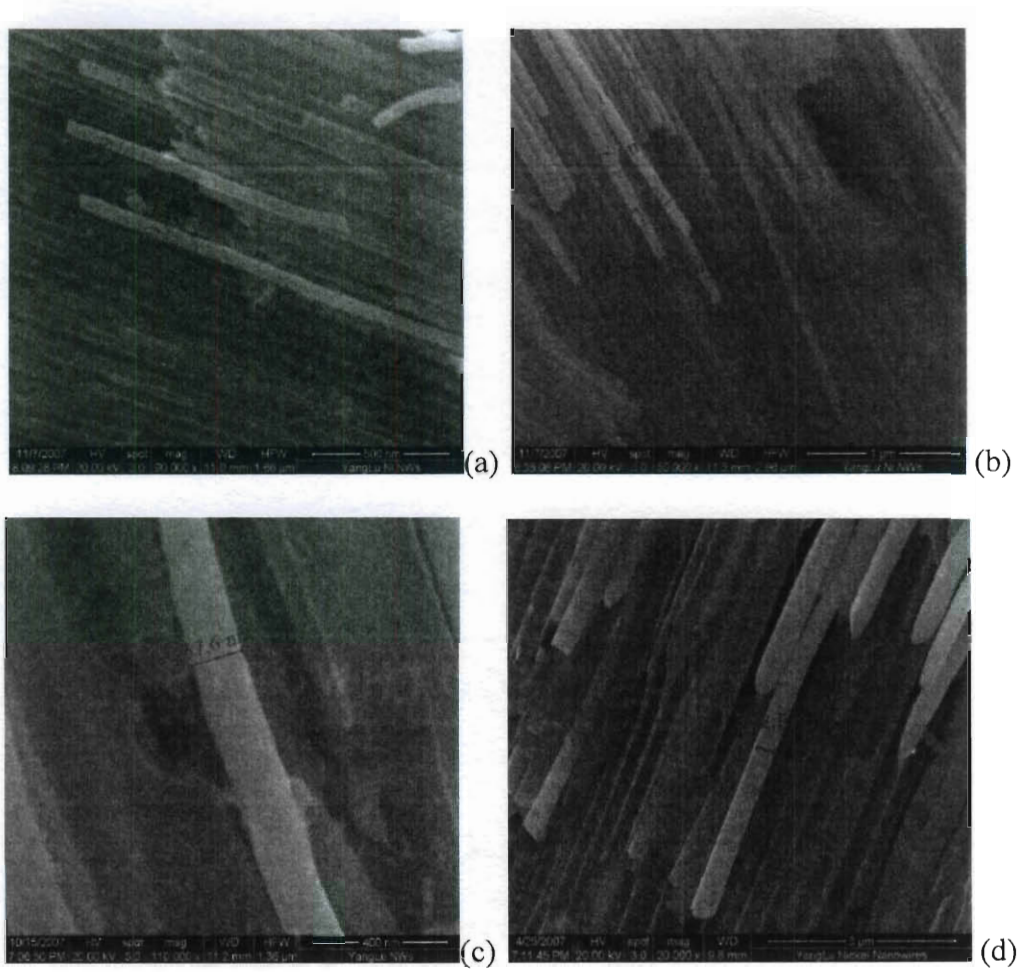

Figure 2-3 Fabrication of Ni NWs with diameter ranging from ~30-300nm

Eventually, freestanding Ni and Au nanowires were obtained by wet etching off the silver back-coating with 4M nitric acid and fully dissolving the AAO template in 6M NaOH solution as shown in Fig. 2-4. Released free-standing nanowires were usually stored in alcohol to prevent possible oxidization, especially for nickel nanowires.

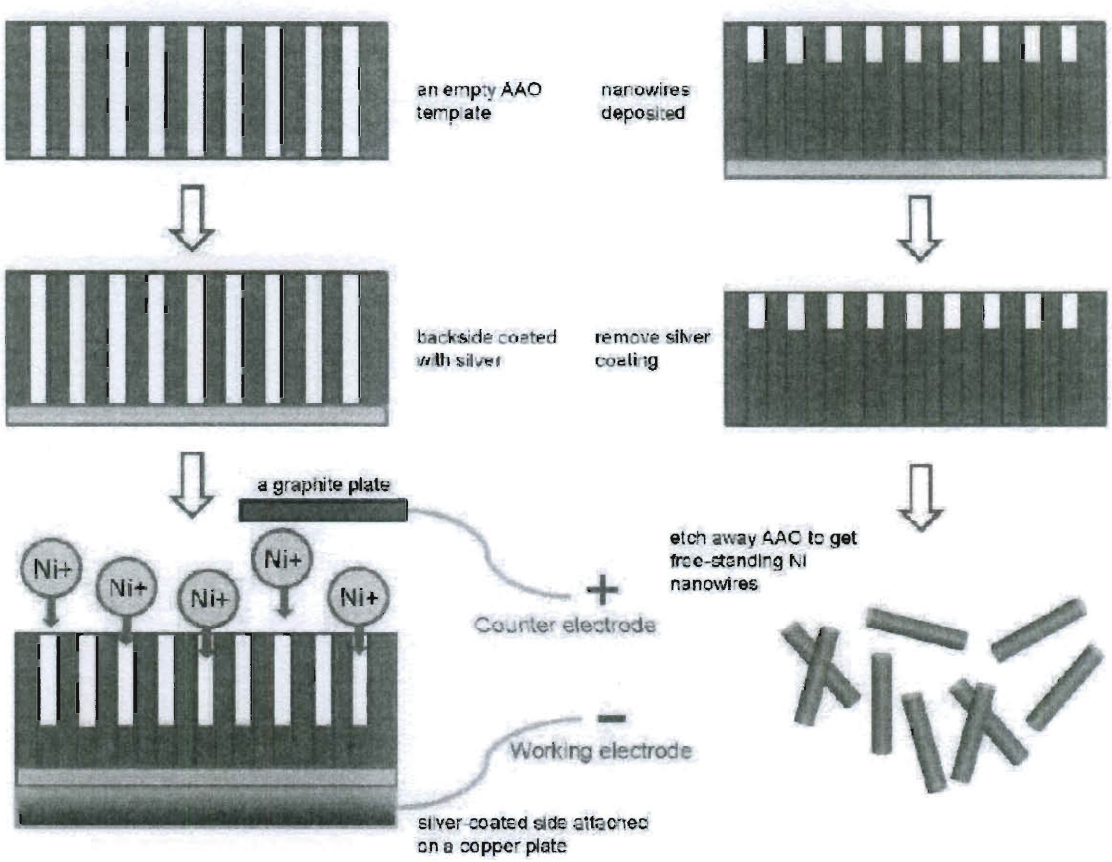

Figure 2-4 The fabrication and releasing flow of free-standing Ni nanowires []

To ensure the chemical composition of the nanowire samples, EDX (Energy-dispersive X-ray spectroscopy) was performed and the results were shown in Figure 2-5 for nickel and gold nanowires, respectively. It must be noted that, the free-standing nanowire were dispersed on silicon wafer substrates, as a result of which Si peaks can be seen in both spectrums.

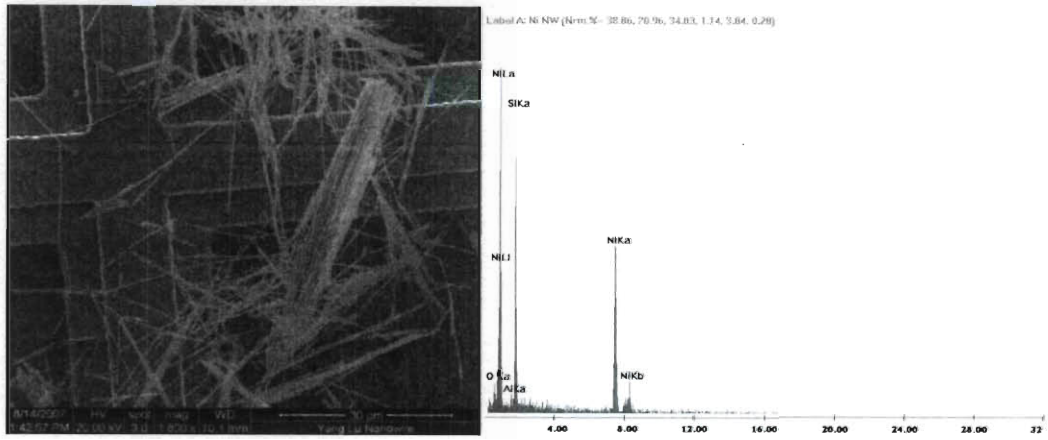

(a)

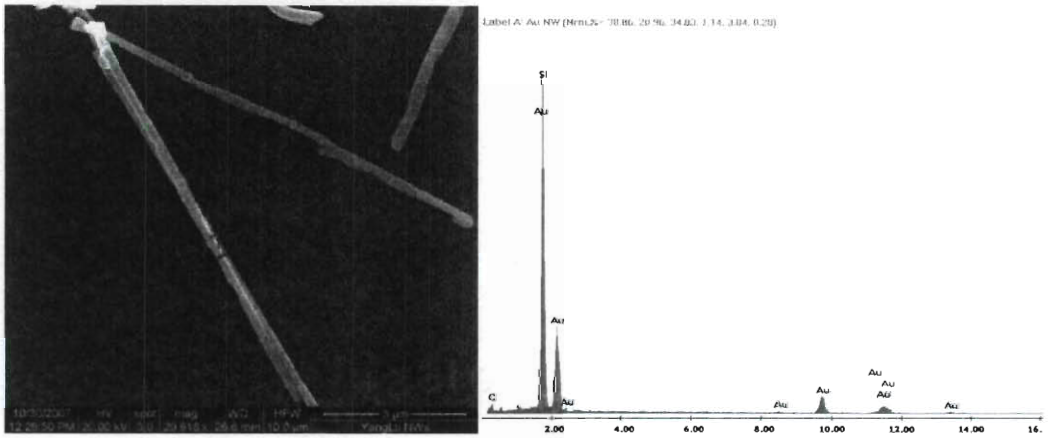

(b)

Figure 2-5 Free-standing nanowires and EDX analysis: (a) free-standing Ni NWs on a lacey-carbon TEM grid and EDX spectrum for free standing Ni NWs on Si substrate; (b) free-standing Au NWs on Si substrate and corresponding EDX spectrum

In addition to gold and nickel, we also fabricated other 1-D metallic nanostructure such as Fe, Co, Ag nanowires and nanorods for various applications, such as catalyst for CNT growth. Furthermore, by alternating the plating solution, we could fabricate multicomponent / multisegmental nanowires, such as Ni/Au/Ni nanowires (as shown in Figure 2-6), for drug/gene delivery applications (as mentioned in Chapter 1).

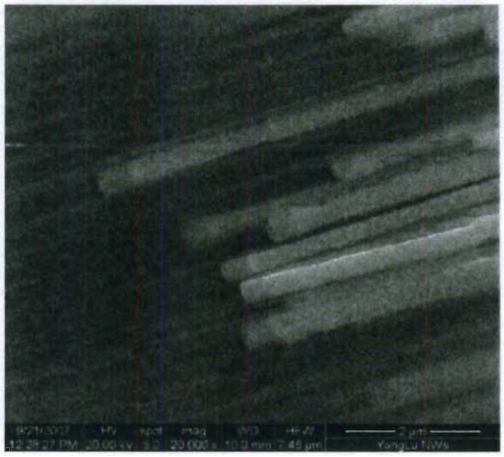

Figure 2-6 Multi-segmental Ni/Au/Ni nanowires with diameter ~200nm

2.2. Macroscopically Controllable Fabrication of Porous Gold Nanorods

Nanoporous metals have been exploited for a wide range of application that take advantage of their extremely high surface-to-volume ratio. Among porous metals, nanoporous gold (np-Au) has attracted special attention from the scientific community due to their catalytic activity [116-117], biosensing [118], surface plasma resonance [119], mechanical properties [120] and biocompatibility [121]. On the other hand, as discussed in Chapter 1, low-aspect-ratio gold nanostructures, such as gold nanorods [58]/ nanodisks [122] /nanocone [123] and nanoshells [124] have drawn considerable attention in recent years owing to their unique and favorable optical properties [58, 125] and strong affinity to biomolecules. For example, Mitamura [126] et al have proved that rod shaped nanoparticles display more valuable optical properties than spherical or cylindrical ones. For instance, while spherical gold particles have only one surface plasmon band (at 510-575nm) depending on size and dielectric environment, nanorods provide two intrinsic

(transverse and longitudinal) bands [58, 127]. In this work, we developed a low-cost high-throughput fabrication process for nanoporous gold nanorods, trying to combine the advantages from both nanoporous structure and low-aspect-ratio "rod" structure.

This three-step fabrication process is shown in Figure 2-7. More importantly, we intentionally over grow the nanowires to form a metal-AAO-metal sandwich structure for real time I-V measurements during the fragmentation stage, in order to monitor and control the fragmentation of nanowires into nanorods.

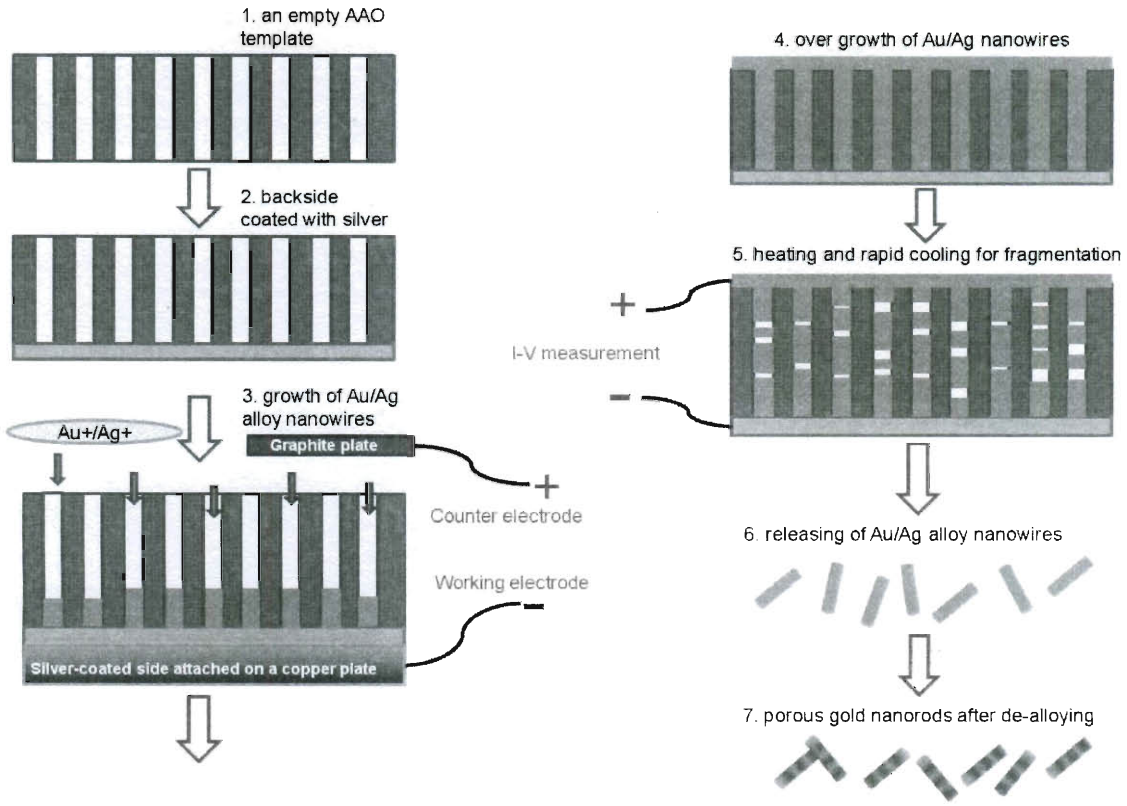

Figure 2-7 Fabrication and fragmentation process for porous gold nanorods

Step1: Electrodeposition of Au-Ag alloy nanowires

Room temperature electrodeposition of Au-Ag alloy nanowires into the nanotemplates was accomplished using a two-electrode system with a graphite counter

electrode at room temperature under a DC power supply (Extech™, ranging from 0-30V, 0.00-1.00A). Here, we use the commercially available AAO templates (Anodisc™ Whatman, Inc) with a pore diameter of 200-300nm. Before electrodeposition, a layer of silver (1-2um) was sputtered on one side of the AAO membrane, which served as the working electrode. The electrolyte was prepared by mixing commercial Au (Technic™ Orotemp®) and Ag (Technic™, major component $K(Ag(CN)_2$) electroplating solutions with a molar ratio of Au+/Ag+ = 1:2 (for a target porosity around 66.67%).

It might be noted that, nanowires were usually intentionally over grown, which resulted in a unique metal-AAO-metal "sandwich" structure. The over-growth Au/Ag layer, along with the silver back-coating layer on the other side of AAO templates, served as electrodes during following I-V measurements in Step 2.

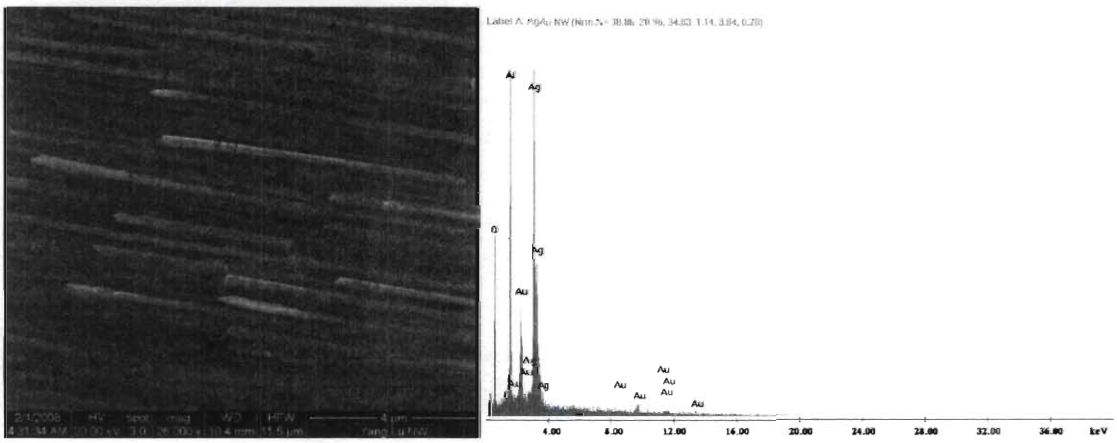

Figure 2-8 SEM image and EDX analysis of Au/Ag alloy nanowires in AAO templates

Step2: Fragmentation with *in situ* I-V measurement

The fragmentation of Au/Ag nanowires into nanorods was accomplished by subjecting the templates containing the Au-Ag-alloy nanowires ("sandwich" structure) to

multiple cycles of annealing and rapid cooling. The fragmentation mechanism is based on Rayleigh instability [128, 129] as well as the geometrical confinement provided by nanosized channels [130], as illustrated in Figure 2-9 (a). As mentioned previously, the nanowires were confined inside AAO channels and covered with metal layers on both ends. Once samples underwent a series of heating-then-cooling cycles between Ta =940°C (the optimum Ta was determined by experiments and should be around/below the melting points for gold (1064°C) and silver (961°C)) and Tc=room temperature, the entire nanowires decayed into a chain of nanorods within the nanochannels of the template, as shown in Figure 2-9 (b) and (c).

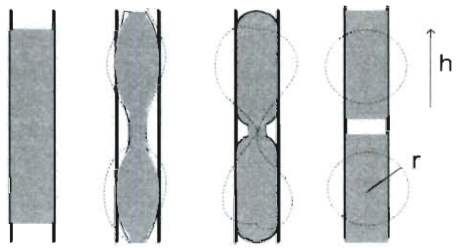

(a)

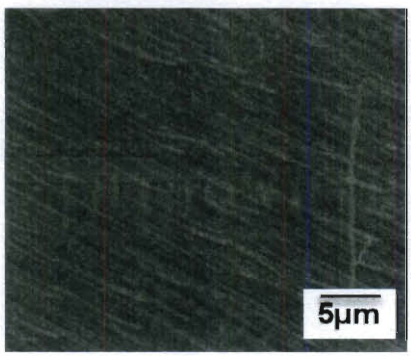

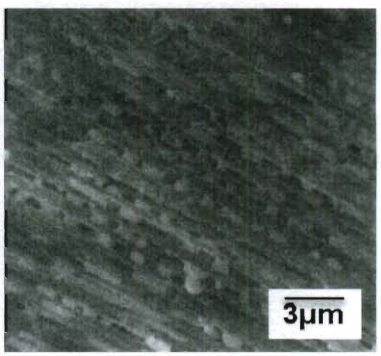

(b) (c)

Figure 2-9 Fragmentation of Au/Ag allow nanowires into Au/Ag nanorods within the geometry confinement of AAO channels: (a) the Rayleigh instability inside AAO

channels; SEM images of Au/Ag nanowires (b) before and (c) after fragmentation process

More importantly, with the unique metal-nanowires in AAO-metal "sandwich" structure, we were able to perform *in situ* I-V measurements for the metal-coated template with nanowire/nanorod inside. The basic idea (as shown in Figure 2-10) is that, for fully grown nanowires, the whole piece of sample would be expected highly conductive, with very low electrical resistance; however, as more and more nanowires broke into discontinuous nanorods, the electrical resistance of the whole piece would increase; eventually, as all nanowires would be broken into discontinuous nanorods, with the conductivity approaching close to zero (since AAO is non-conductive).

Figure 2-10 shows the results of one of the successful experiments containing four I-V curves with decreased slopes (i.e. electrical conductivities) after each heating-and-rapid cooling. The curve with black squares showed the I-V measurement for original "sandwich" sample before fragmentation process and the bottom curve (with blue triangles toward downside) showed the final state with almost zero conductivity (slope was almost zero), a trend which appeared to be in agreement to the theoretical prediction.

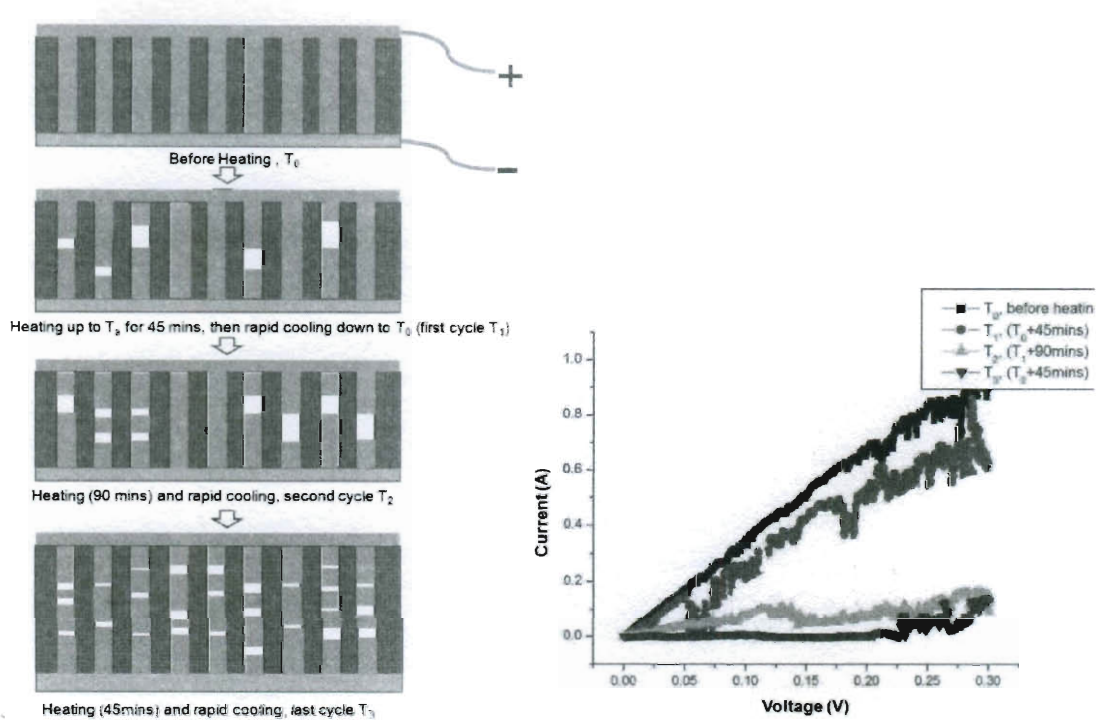

Figure 2-10 *In situ* I-V measurement for macroscopically monitoring the fragmentation process (the right curves were experimental data)

Step3: De-alloying process

Once the Au/Ag alloy nanorods were liberated by dissolution of the AAO templates, using a 6M NaOH solution, the silver component of the nanorods were then etched away using concentrated nitric acid. This is the so called "de-alloying" process [121], with final products containing only gold component in the porous structure. Figure 2-11 shows the resultant porous gold nanorods under SEM and TEM imaging.

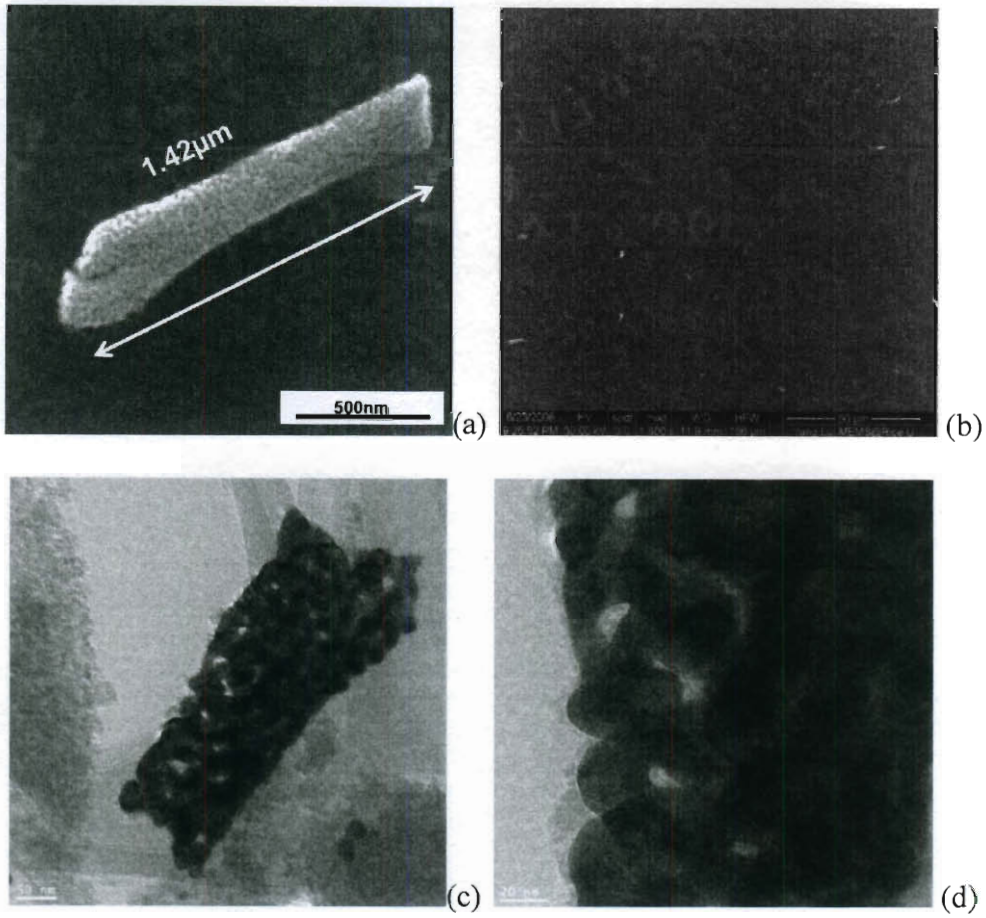

Figure 2-11 Microstructure of porous gold nanorods: (a) SEM image of a porous gold nanorod (~200-300nm in diameter and 1.42μm in length); (b) low magnification SEM image showing the dispersion of free-standing porous gold nanorods on substrate; (c) TEM image of a porous gold nanorod on lacey carbon support film; (d) high magnification TEM image showing the porosity of the nanorod in (c).

In summary, we have developed a macroscopically controllable, high throughput and cost-effective method for the synthesis of porous gold nanorods. This technique can produce large quantity porous gold nanorods with uniform diameters and porosity, which

may be used as a method for low cost industry-scale synthesis of porous gold nanorods for potential biomedical applications, such as cell image contrast agents or drug delivery.

2.3. Crystalline Structure Analysis of Gold and Nickel Nanowires with Different Diameters

In order to study the deformation mechanisms of as-fabricated metallic nanowires, it is necessary to perform microstructure analysis to understand the crystalline structures of these samples. For metallic nanowires, we performed selected area diffraction (SAD) on multiple locations along the individual nanowire sample inside TEM. By analyzing corresponding diffraction patterns, we were able to determine their crystalline structures and growth orientations.

First of all, for all Au nanowire samples (as shown in Figure 2-12), regardless of their diameters, multiple SAD analysis confirmed that they were single crystals with [111] orientation.

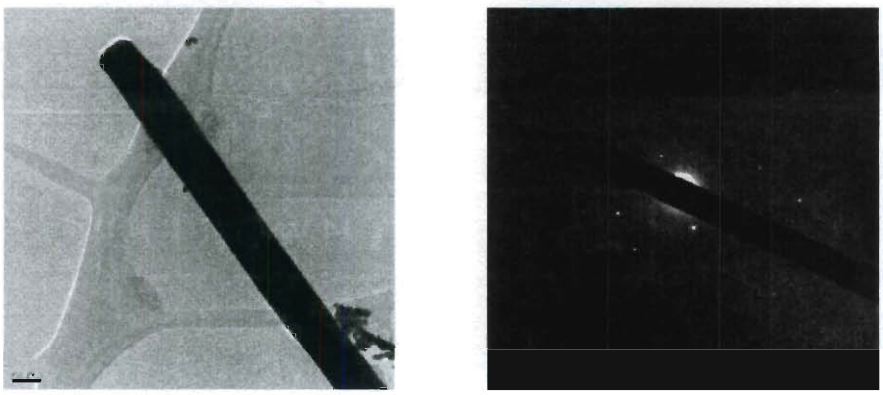

Figure 2-12 TEM image of an Au NW with corresponding selected area diffraction (SAD) pattern. This 200nm-diameter gold nanowire grows with a [111] orientation, while the zone direction being (211).

While for the Ni NWs in present study, samples can be roughly divided into three groups based on their diameters: small diameter (~30-50nm), medium diameter (~80-100 nm) and large diameter (~200-300 nm) ones. The TEM select area diffraction (SAD) analysis (Figure 2-13) of individual NWs indicated that medium diameter (~80-100nm) Ni NWs were single crystals with the [111] growth orientation while the large diameter (~200-300nm) Ni NWs were single crystal with [112] orientation [33].

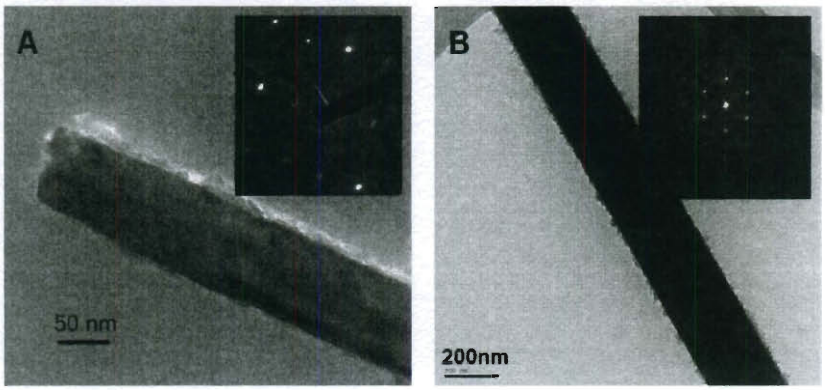

Figure 2-13 TEM image of Ni NWs with corresponding selected area diffraction (SAD) patterns: (a) a single crystal 100nm-diameter Ni nanowire grows along [111] direction; (b) a single crystal 300nm-diameter Ni nanowire with a [112] orientation

More interestingly, for the third group, i.e. small diameter Ni nanowires (D< ~ 50nm), they were no longer in single crystalline structures. Instead, we observed unique twin structures in these samples by HRTEM imaging (Figure 2-14).

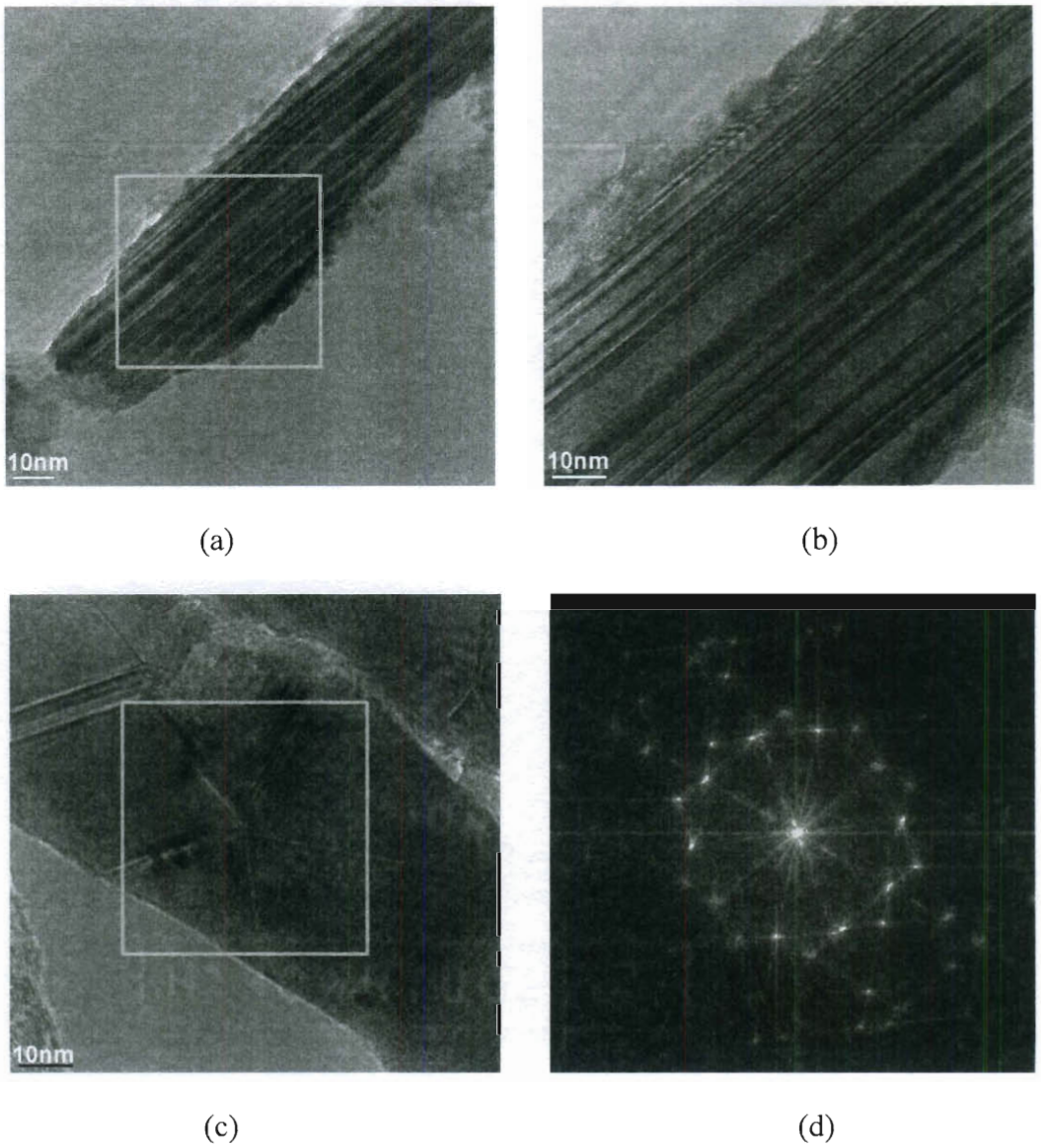

Figure 2-14 Twin structures found in Ni NWs with diameters less than 50nm: (a) HRTEM image of a nanowire with parallel twins along the wire direction; (b) the magnified view of parallel twin structure in the square area in (a); (c) HRTEM image of a nanowire with five-fold twin structure; (d) the corresponding fast Fourier transformation (FFT) image from the square area in (c), indicating the ten-fold symmetry.

The parallel twin structure in nanocrystalline materials has drawn considerable interests in the recent years [131], while five-fold twin was even more rarely reported for metals with high stacking fault energy, such as nickel [132]. While the underlying mechanisms for the formation of twin structures remain elusive, it would be definitely interesting to characterize their mechanical and electrical properties, which will be one of potential future research directions.

Chapter 3

In Situ Tensile Testing of Gold and Nickel Nanowires (Diameters ~100-300nm) using a Novel Micro Mechanical Device

3.1. A Multi-step Method for In Situ Mechanical Characterization of 1-D Nanostructures Using a Novel Micromechanical Device

3.1.1. Introduction

One-dimensional nanostructures, such as metallic nanowires and carbon nanotubes, have stimulated great interest recently as important building blocks for nanoscale electronic and electromechanical devices used in various applications. However, the ability to achieve the full potential of these fascinating technologies is ultimately limited by how these one-dimensional nanomaterials will behave at relevant length scales. Although significant progresses have been made on mechanical testing of 1-D nanostructures using existing techniques such as AFM based bending methods [16, 78, 104, 133], performing direct uni-axial nanomechanical characterization of an individual nanowire or nanotube, still remains a challenge.

Numerous MEMS devices developed to perform mechanical testing on 1-D and 2-D nanostructures have recently emerged due to the following reasons: (1) Knowledge of MEMS technology accumulated in the past decades have enabled the development of a

wide range of device designs for different testing purposes and configurations, with excellent statistical representations; (2) The compact size of a MEMS device makes it ideal to test samples with nanometer dimensions. This property also makes them suitable for in situ testing within various microscope vacuum chambers; (3) The quantitative nature and high displacement/force resolution obtainable through MEMS device based measurements makes them especially attractive for nanomechanical testing. Due to the large amount of literature available in this area, only a brief review of some representative devices specifically designed for nanomechanical testing of samples with nanometer dimensions will be given.

There are two broad categories of design concepts for MEMS based nanomechanical testing platforms in terms of actuation and sensing mechanisms: one relies on external equipment for loading or sensing, and the other has built-in on-chip actuators and/or sensors. The MEMS-based in-situ TEM tensile testing bed developed by Haque and Saif [103] to characterize free-standing nanoscale thin films is an example of a device that falls under the first category. Also falling under the same category are the polysilicon MEMS structures fabricated by Boyce et al. [135] in order to study strength distributions in freestanding polysilicon layers. Another example of this type of devices is a MEMS test bed using external AFM piezoelectric actuation and optical digital image correlation method for displacements measurements [136]. On the other hand, Zhu et al. [100] designed an on-chip nanoscale tensile testing platform for testing 1D nanostructures and thin films that consisted of a thermal/electrostatic actuator for load application and a differential capacitance load sensor for displacement and load measurement. Muhlstein et al. [137] developed a fatigue testing platform that consisted of

an electrostatically actuated comb drive actuator and a capacitive displacement sensor. Kahn et al. [138] designed a comb-drive based MEMS device to test nanoscale biological materials, in which electrostatic actuation was again used to drive the shuttles across which the samples were clamped, while simple cantilever beams were used to monitor the force applied on the specimen. All three of the latter are examples of devices that fall under the second category. Devices falling under either of these two categories of MEMS-based nanomechanical testing platforms have their own set of advantages and disadvantages and they both offer numerous possibilities to test nanoscale samples with considerable accuracy.

Recently we designed and fabricated a micromechanical device, which in conjunction with a quantitative nanoindenter can perform uni-axial tensile testing on 1-D nanoscale samples [139], using established micro-fabrication processes. Using this device, compressive force applied by a quantitative *in situ* SEM/TEM nanoindenter can be converted into pure tension loading at the sample stages in order to mechanically deform a one-dimensional nanoscale sample, such as a nanotube or a nanowire. At the same time, the underlying deformation process could be monitored by high resolution electron microscopy. It is noted that similar push-to-pull idea was explored in the past such as the Theta sample development [140, 141] and a method to measure intrinsic strain in thin films [142]. Our preliminary finite element analysis (FEA) showed that the force vs. displacement curves for the tested samples can be obtained independently from the readings of the nanoindenter using simple conversion factors. For example, for a 5 μm long Ni nanowire sample having a 300nm diameter, the force conversion factor, defined here as the ratio of the force acting on the sample to the force applied by the

indenter on the top shuttle in the negative y direction (see Figure 1), was found to be 0.666 and the displacement conversion factor, defined here as the ratio of the nanoindenter tip displacement to the sample stage displacement (in the presence of a sample *i.e.* the nanowire, sample stage displacement can be interpreted as the elongation of the sample) [139], was found to be ~ 0.987. Both these values were obtained via FEA modeling (the Young's modulus of the Ni nanowires was assumed to be the same as that of bulk Ni *i.e.* 200GPa). Both these conversion factors remain valid, though not extremely accurate, for metal nanowires having dimensions similar to the one described above and having a Young's modulus value greater than ~ 100GPa. However, our in-depth FEA indicated that this simple relationship will no longer hold when testing samples have relatively low Young's modulus. Under these conditions, forces vs. displacement curves derived from the nanoindenter readings using the aforementioned conversion factors will no longer be accurate. In order to address this issue, we present a multi-step method which would enable the use of this device for the characterization of a wide range of samples with considerable accuracy. Briefly, the first step involves making suitable corrections to the parameters of the FEA model of a device, such that its behavior closely resembles that of the actual device (without a mounted sample). This step is to make sure our FEA model is properly calibrated against the real device performance and is ready for subsequent analyses. Subsequently, the second step is taken because the FEA simulated stiffness of the sample loaded device will depend on sample modulus and this relationship needs to be explicitly established in order to accurately test a material with unknown material properties. A series of virtual experiments must be conducted using a device loaded with virtual samples with varying Young's moduli. The

FEA simulated system stiffness obtained (K_s, defined as the force applied by the nanoindenter divided by the nanoindenter displacement in the presence of a mounted sample on the device) must then be plotted as a function of sample Young's modulus. The Young's modulus for a real sample with unknown material properties can thus be determined from above plot, using the K_s value derived from the linear portion of force-displacement curve of an actual nanoindenter driven experiment. In the third and final step, another FEA simulation must be performed using the previously determined "true" sample Young's modulus in order to obtain the actual force and displacement conversion factors for this specific sample. We can then use these conversion factors to independently obtain the complete experimental force vs. displacement curve for the aforementioned sample. Additionally, in this paper, we also aim to discuss the range of sample Young's modulus within which the device can be operated with acceptable accuracy using fixed conversion factors. It is worth noting that, compared to the force conversion factor which relies solely on FEA simulations, the displacement conversion factor is less problematic since the sample elongation could be detected and measured directly inside SEM or TEM from image analysis. It is for this reason that we chose to focus on the force conversion factor determination in this paper.

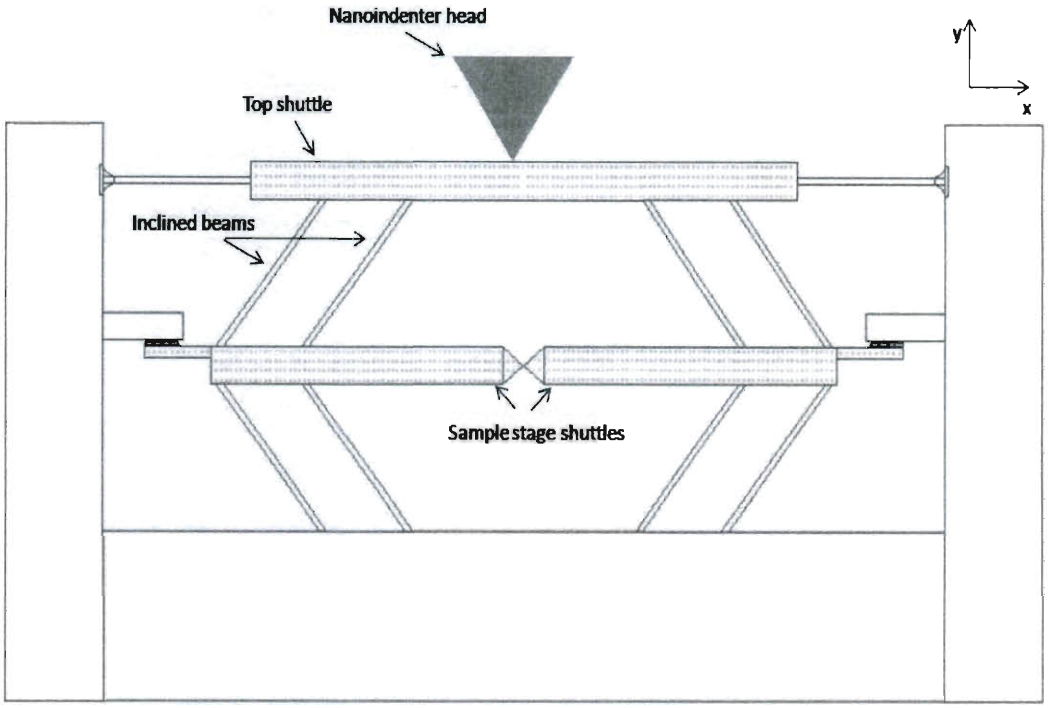

Figure 3-1 Schematic of the micromechanical device

3.1.2. Micromechanical Device Development and Modeling

The devices described in this paper were developed to perform quantitative tensile experiments on 1-D nanostructures to avoid potential buckling instability of samples with high aspect ratio. It is a passive type of a MEMS device where application and measurement of load and displacement can be realized with the aid of a quantitative nanoindenter housed within the vacuum chamber of a SEM or a TEM. The force and displacement resolution of the nanoindenter lies in the order of a few tens of nano-Newtons and a few angstroms respectively. The geometry of the device is shown in Figure 3-1. It basically consists of a pair of movable shuttles (as the sample stage) that

are attached to a top shuttle via 60° inclined freestanding chevron beams. Devices investigated in this work were fabricated on <100> oriented p-doped silicon on insulator (SOI) substrates, with 9.5μm thick device layer. The fabrication scheme adopted involved the use of dicing lines on the masks such that individual devices could be isolated from the wafers on 2 mm × 3 mm pieces, which could in turn be fitted onto a TEM sample holder. A window under the specimen area of the device was micro-fabricated to ensure electron beam transparency for *in situ* TEM experiments and to also facilitate nanoindenter head positioning (Figure 3-2).

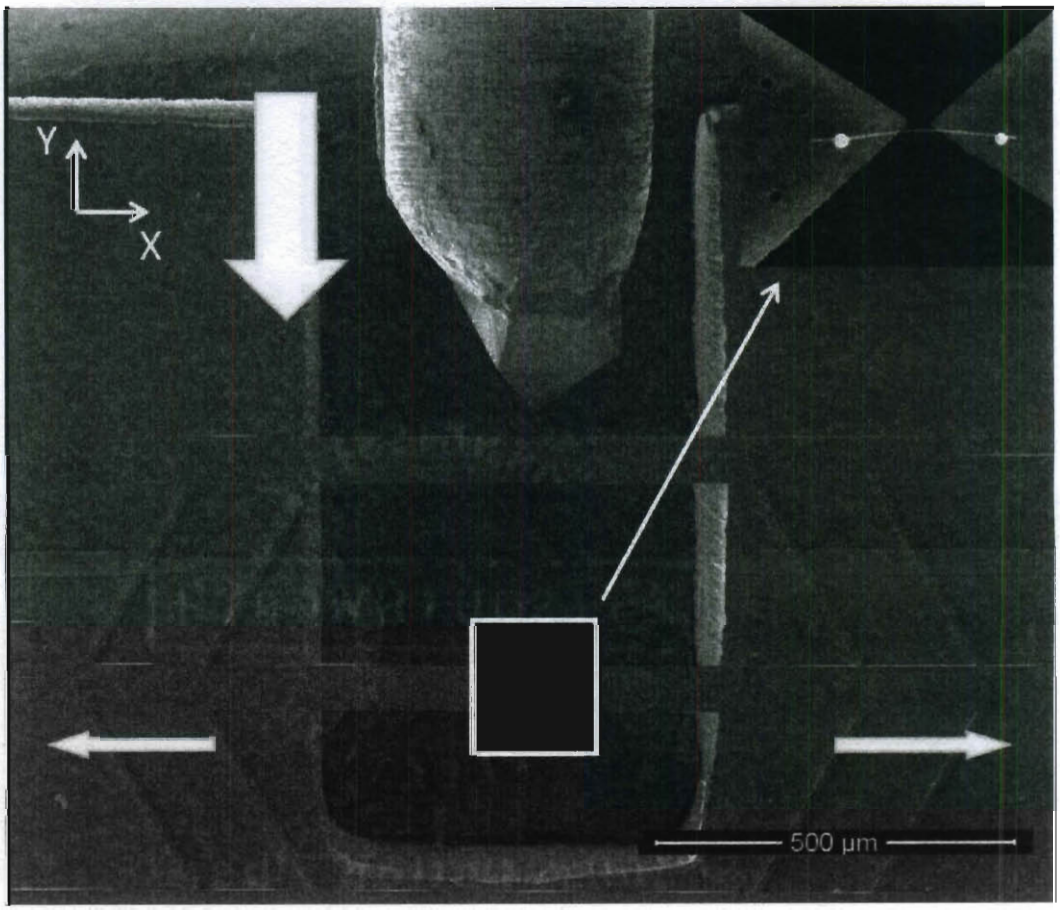

Figure 3-2 SEM image showing the geometry of the fabricated device and the nanoindenter tip. Arrows show the direction of movement of the top shuttle and sample

stage shuttles upon load application. The inset shows a close up image of a mounted Ni nanowire sample

The actuation mechanism for the devices involves the usage of a nanoindenter inside a SEM or a TEM to apply a load on the top shuttle of the device in the vertical (Y) direction. Four sets of symmetrical inclined beams transform the vertical motion of the top shuttle into a horizontal (X) translation of the sample stage shuttles. Proper alignment of the nanoindenter head would result in the sample stage shuttles moving symmetrically in the negative Y direction, thus ensuring that the sample, clamped across the sample stage shuttles, experiences axial tensile loading in X direction (Figure 3-2). The system is purely mechanical as opposed to most of the existing techniques that involve electro-mechanical or thermo-mechanical coupling. The simple design helps minimize the sources of errors, and the use of a quantitative nanoindenter ensures reliable results with a sufficiently high resolution [139].

The device behavior under mechanical loading, both in the presence or the absence of a mounted virtual sample, was modeled using FEA (ANSYS ^{TM}) in order to determine the relationship between the load applied by the nanoindenter and the force acting on the sample stage/sample, and the relationship between nanoindenter tip/top shuttle displacement and sample stage displacement/sample elongation. The modeling was done using the plane stress model employing a device layer thickness of 9.5 μm. The Plane 42 elements meshing were employed in our current study. More complex Plane 82 elements were also employed and it was found that there was no significant difference between these two elements for this device. The devices were assumed to be operating in

the linear elastic regime and the material properties were assumed to be isotropic. For all analyses, the Young's modulus and Poisson's ratio of silicon were assumed to be 160GPa (value obtained via independent nanoindentation experiments conducted on the actual device) and 0.278 [143] respectively. A 5 μm long virtual nanowire with a 300nm diameter was used to model the device behavior in the presence of a mounted sample. Figure 3-3 shows the meshing of the device as well as a clamped virtual nanowire sample.

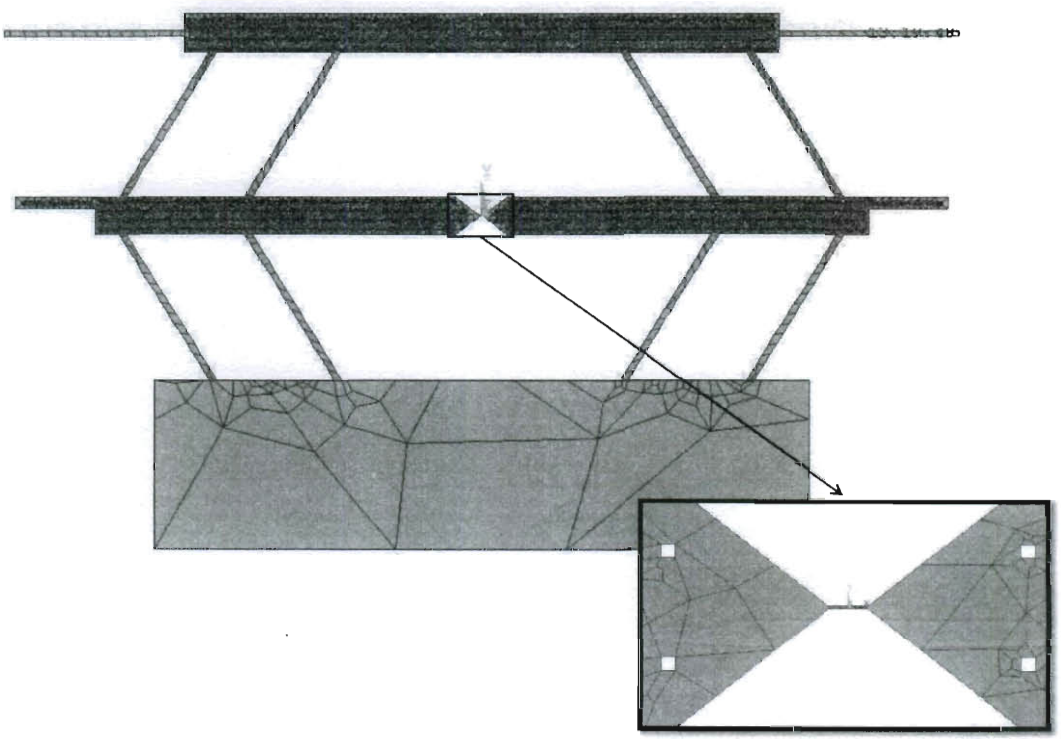

Figure 3-3 Finite element meshing of the micromechanical device clamped with a 5-micron long nanowire (The inset shows a close up image of a mounted nanowire sample between two sample stage shuttles)

3.1.3. Multi-step Methodology Development

Step 1: FEA Model Calibration In order to calibrate our finite element model constructed based on design parameters against the behavior of actual device, calibration experiments were done on devices with no sample mounted. This first step is necessary since the geometrical dimensions of the fabricated device generally differ from the original design due to the anomalies introduced by the fabrication process. By varying the thickness and other geometrical parameters(such as chevron beam width) using measurements obtained from actual device and then compare the simulated and experimental force-displacement curves, we calibrated the FEA model of device and make sure its behavior during virtual experiments closely resembles that of the actual device in the absence of a mounted sample, e.g. the device stiffness (K_d, the force applied by the indenter divided by the resulting displacement of the indenter head for a device without a mounted sample on it) obtained in simulation closely follow K_d from the actual calibration experiment (Figure 3-4).

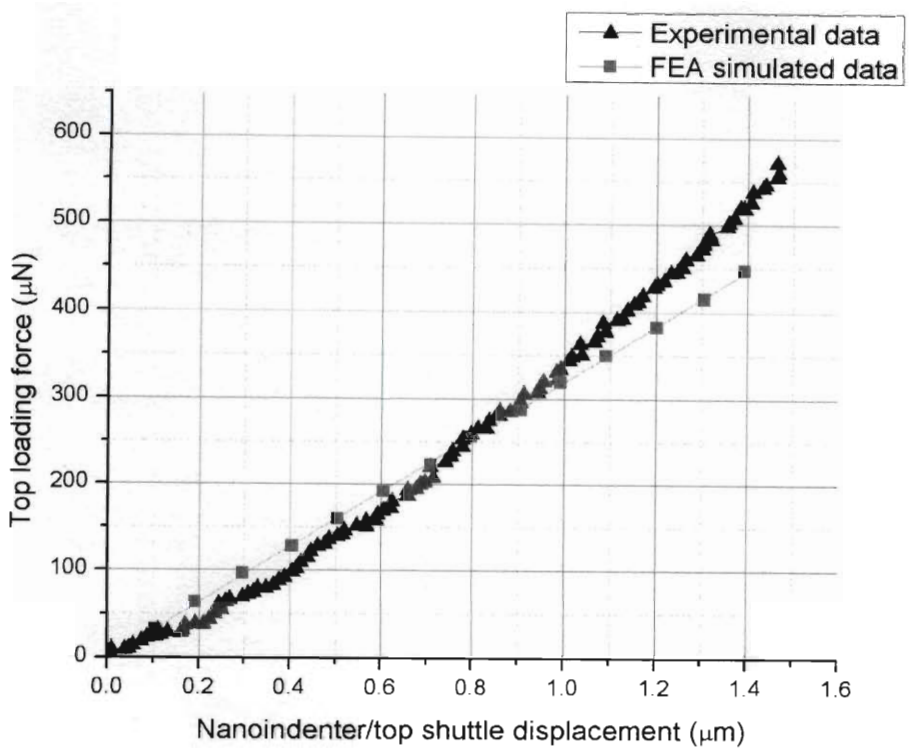

Figure 3-4 Measured and simulated micromechanical device calibration profile (blue triangles show the experimental data from one nanoindentation test on an empty device, and red squares show FEA data of the calibrated model)

Figure 3-5 shows the X and Y nodal displacement contour for a device, without a mounted sample on it, upon load application on the top shuttle. The X direction displacement contour shows that two shuttles move in opposite directions along X axis upon load application. With testing specimen loaded, this value can be naturally considered as the extension of the sample. The Y direction displacement contour was used to calculate the device stiffness K_d. For example, the stiffness K_d of one particular micromechanical device was determined to be ~ 438N/m by averaging the results of

several independent indentation experiments on device without mounted sample on it. After making a few adjustments according to the actual measurement of the as-made devices, such as beam width and thickness, to the dimensions of the FEA model of the device, a similar value for K_d was obtained via simulation.

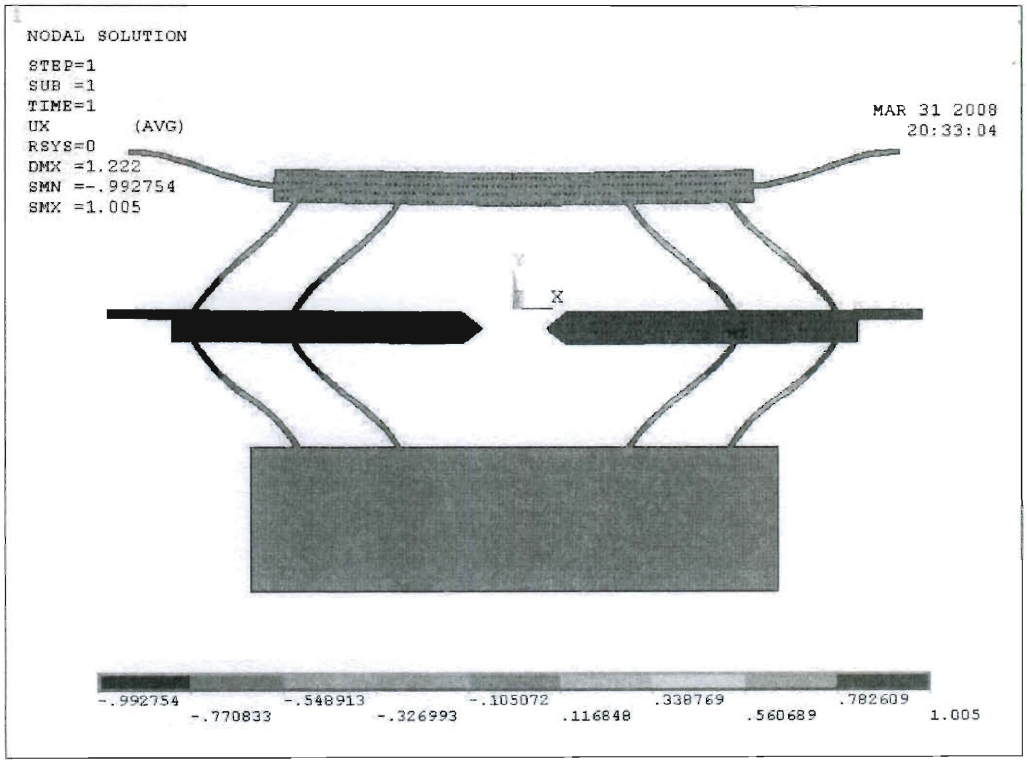

(a)

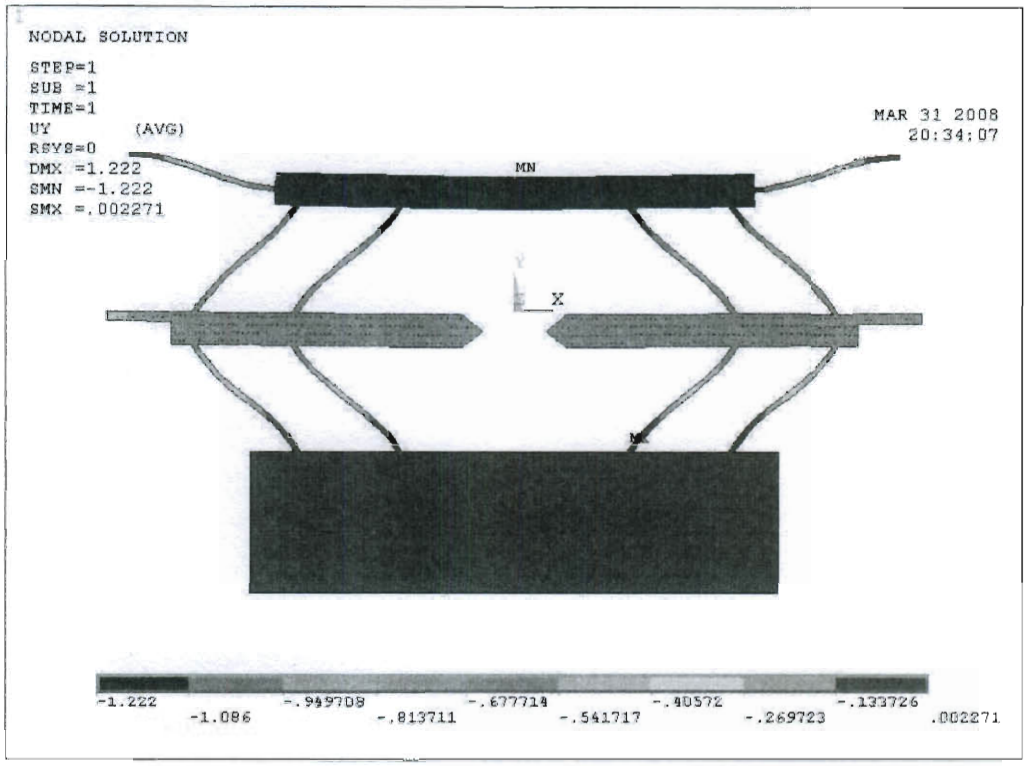

(b)

Figure 3-5 FEA displacement contour of the MMD (a) X axis nodal displacement contour of the micromechanical device and (b) Y axis nodal displacement contour of the micromechanical device, without a mounted sample, upon load application on the top shuttle (unit: μm)

Step 2: Determination of Actual Sample Young's Modulus Once the FEA model of empty device has been appropriately calibrated, we can focus our attention on samples with unknown material properties (here we focus on the Young's modulus). A virtual 1-D sample having a geometry similar to the sample which is to be tested in real time (in our case we used a 5μm long nanowire having a 300nm diameter) was clamped

onto the FEA model of the device (Figure 3-3). A series of FEA simulations under different applied loading levels were performed while varying Young's modulus of the mounted sample. By determining the Y direction nodal displacements of the device's top shuttle at different applied loads, the system stiffness K_s, defined as the force applied by the indenter divided by the resulting displacement of the indenter head for a device with a mounted sample on it, was obtained and plotted as a function of Young's modulus of the virtual sample (Figure 3-6).

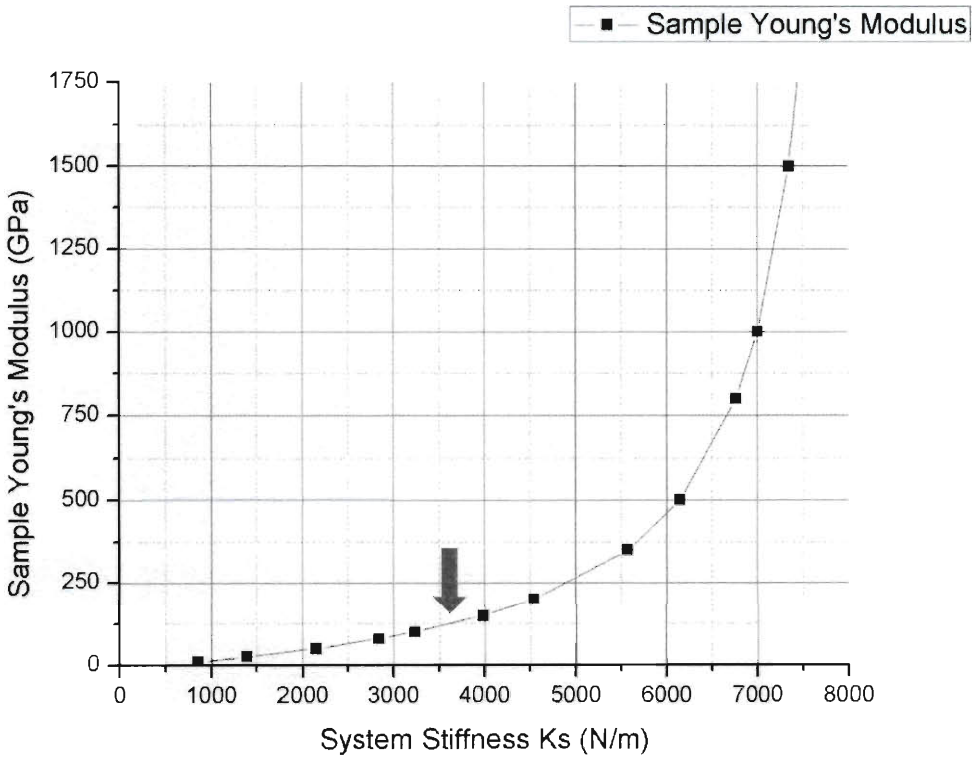

Figure 3-6 Young's modulus of a virtual nanowire sample as a function of system stiffness K_s (the red arrow indicates a K_s value of 3571N/m obtained from a preliminary test for a device mounted with a 300nm-diameter nickel nanowire)

Shown in Figure 3-6 is a plot of system stiffness (K_s) vs. mounted sample's Young's modulus. In order to determine the Young's modulus of the sample to be tested in real time, the K_s value of the device with the mounted sample must first be determined from the linear portion of the force-displacement curve of the nanoindenter driven experiment conducted in real time. This K_s value can in turn be used to ascertain the Young's modulus for the sample using the plot shown in Figure 6. For example, a K_s value of ~ 3571N/m was obtained for a device mounted with a 300nm-diameter nickel nanowire in our preliminary experiments conducted in real time. Using the plot in Figure 3-6 (as indicated by the red arrow), the Young's modulus for this nanowire was ascertained to be 120±12GPa, a value that is lower than the Young's modulus of bulk nickel (200GPa). This value is consistent with an AFM force-deflection method determined Young's modulus value (124±8GPa) of a 300nm-diameter nickel nanowire that was fabricated from the same batch. Additional experiments are planned to further investigate this anomaly in elastic properties of nickel nanowires. It is important to realize that other factors such as indenter tip alignment and specimen attachment and alignment will also affect our measurement results which could contribute to the uncertainties of this method.

Step 3: Determination of Conversion Factor (C_F) In the third and final step, our goal is to obtain the "true" force conversion factor (C_F) for the device mounted with the sample that is to be characterized. This is a critical step to realize the quantitative nature of the micromechanical devices in conjunction with the high resolution *in situ* SEM/TEM nanoindenter.

This step involves the usage of the fixed value of Young's modulus obtained from step 2 in order to perform another FEA simulation following above steps. The procedure is similar to the one described in step 2, but we pay close attention on the X direction displacement under a prescribed top loading, since it provides the strain of the nanowire specimen. Therefore, the actual force loaded on the nanowire sample can be calculated based on its strain and dimensions, as well as Young's modulus obtained above. Thus the actual force conversion ratio of the device system loaded with the specific sample will be obtained. For example, in the case of the same 300nm diameter nickel nanowire, based on the Young's modulus value determined in step 2, a force conversion factor of 0.65 was obtained via simulation using the modified FEA model. We believe that compared to the force conversion factor we previously reported, which was based on the Young's modulus of bulk Ni, the value obtained via this novel method is more accurate. In addition, using the X and Y direction nodal displacements contour, the displacement conversion factor between the nanoindenter/top shuttle and the sample stages was also determined. Note this displacement conversion factor could also be determined via imaging of the SEM or TEM for experiments performed *in situ*.

3.1.4. Discussion

As mentioned earlier, when using the nanoindenter actuated micromechanical device for in-situ experiments, we rely solely on the load signal readings from the nanoindenter in order to determine the applied force on samples. Therefore, determination of force conversion factor is of critical importance as its accuracy greatly affects the computed applied force thus stress on the sample. It has been demonstrated that the newly developed multi-step method can enable us to obtain more accurate force conversion factor than the one based on bulk material Young's Modulus values. This clearly demonstrates the importance of this method especially when testing samples with nanometer dimensions, due to the possible size effects in mechanical properties of materials at small length scales [16, 78, 105, 133].

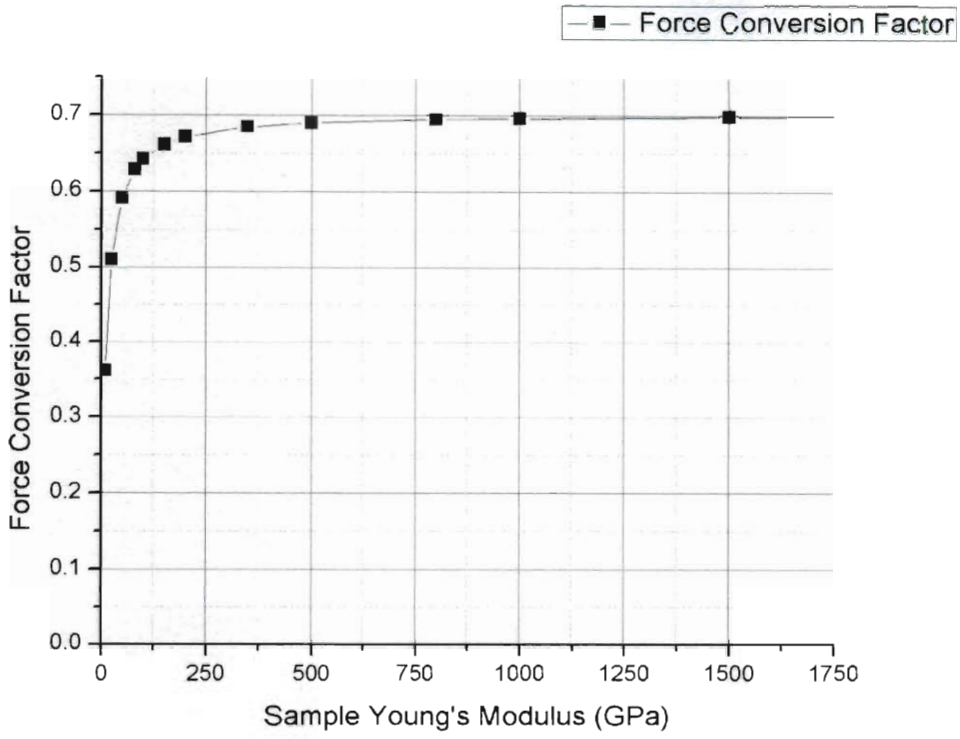

Figure 3-7 Force conversion factor (C_F) as a function of sample Young's modulus

When using the micromechanical devices as a mechanical testing platform for 1D nanomaterials, it is always advantageous to have fixed force and displacement conversion factors with a tolerable error margin. Hence, it is important to find an appropriate sample elastic property range within which simple fixed conversion factors could still be reliably used with reasonable accuracy. For this purpose, we conducted a series of finite element simulations to study the variation of force conversion factors with different sample Young's modulus. Again we apply a prescribed loading on device clamped with a virtual nanowire sample and vary the Young's modulus of the sample, as in step 2. Then we calculated the forces resulted on sample through the X displacements (extensions) of the

nanowire samples, similar to the step 3. So the force conversion factor will be obtained as a function of sample Young's modulus (Figure 3-7) under specific loading. From looking at the plot shown in Figure 3-7, the following observations can be made: (1) force conversion factor increase with increase in the sample Young's modulus; (2) at values close to 500GPa and above, the force conversion factors gradually approach an asymptotic value of ~ 0.7 for a wide range of sample Young's modulus; (3) for samples with relatively small values of Young's modulus (*i.e.* below ~ 100GPa), the force conversion factor increases dramatically with increase in sample Young's modulus. It might be reasonable to say that for samples having a Young's modulus value greater than ~ 100GPa, the force conversion factor could be approximated to 0.666 with relatively good accuracy (less than 5% error). On the other hand, using a curve similar to the one shown in Figure 3-7, force conversion factors can be computed with much greater accuracy. Another important implication of this study is that since the device stiffness can be tailored through the number and dimension of the connecting chevron beams, it is possible to design a device such that the force conversion factor becomes a constant even for small values of sample Young's modulus, and make the device capable of testing such materials with high accuracy. It is also worth mentioning that the factor of machine compliance has been taken into consideration of our nanoindenter setup inside SEM/TEM chamber and calibration experiments were done to get the correct machine compliance value before the actual measurements.

3.1.5. Conclusion

The effect of sample Young's modulus on the force conversion factor of a nanoindenter actuated micromechanical testing platform has been examined extensively using finite element analysis. Our simulation demonstrated that the force applied on a 1-D nanoscale sample mounted on the micromechanical device using a quantitative nanoindenter varies quite dramatically with variation in sample Young's modulus, especially for samples have a value of Young's modulus lower than 120GPa. A multi-step method to overcome this limitation has been proposed. This method involves the usage of both FEA simulations and actual indentation experiments. Force conversion factors computed using this technique are considered to be more accurate than the ones reported earlier [139] since the latter were derived from simulations that were based on the bulk Young's modulus of the sample material. The technique provides a viable solution for obtaining accurate force-displacement or stress-strain curves for 1D nanoscale samples with unknown properties. We emphasize that this multi-step method is particularly useful for nanoscale samples due to the well-known size effects in mechanical properties of materials. Finally, it is worth noting that the geometrical design of our MEMS based micromechanical device can be modified for testing a wide range of nanomaterials with high accuracy.

3.2. In Situ SEM Testing of Gold Nanowires with Different Diameters

In this section, we report on the usage of our micro mechanical devices (MMD) for *in situ* quantitative mechanical characterization of individual gold nanowires within a scanning electron microscope (SEM) equipped with a quantitative nanoindenter. The design of the device makes it possible to convert the compressive nanoindentation force applied to the top shuttle to uniaxial tension on the specimen attached to the sample stages [105]. Finite-element analysis and experimental calibration have been employed to extract the specimen stress versus strain curve from the indentation load versus displacement curve [104]. The stress versus strain curves for five 100–300nm-diameter Au nanowire specimens are presented and analyzed.

3.2.1. Sample Positioning and Clamping

Sample positioning, in this case, refers to the placement of a nanowire at the desired location with micrometer resolution. The fact that the specimens must be freestanding, clamped at both ends, and well aligned in the tensile direction makes sample positioning and clamping quite a challenging task. The novel technique that was adopted in order to mount the Au nanowires is thus described here in brief. A portion of each sample-stage shuttle was coated with a thin layer of epoxy (HARDMAN Water-Clear Epoxy). A droplet from a gold nanowire solution, containing <111>-oriented nanowires grown via electrodeposition (Chapter 2), was first dispersed in isopropanol by ultrasonication for 5–10 min. A drop of this dispersion was deposited on top of a Si wafer coated with a 5-nm-thick layer of titanium. Individual nanowires, ~15 μm long and 100–300 nm in diameter and, hence, visible under an optical microscope, were subsequently

picked up and placed across the shuttles using micromanipulators housed within a probe station (The Micromanipulator Company, Carson City, NV). Tungsten tips (The Micromanipulator Company, Carson City, NV) were used to perform the manipulation of the nanowires, since they were found to attach to the tips via electrostatic interaction. The epoxy layer, upon hardening, acts as a clamp for the tensile specimens.

3.2.2. Experiment

The tensile experiment on the clamped nanowire was performed within a SEM (FEI Quanta 400 high-resolution field emission SEM, FEI Company, Hillsboro, OR) equipped with an InSEM nanoindenter (Agilent Technologies, Oak Ridge, TN) system. A blunt cube corner nanoindenter tip was used to perform the indentation. 9 ± 0.5 μm thick devices with eight 45◦ inclined beams attached to the sample-stage shuttles were used for all the experiments described in this paper.

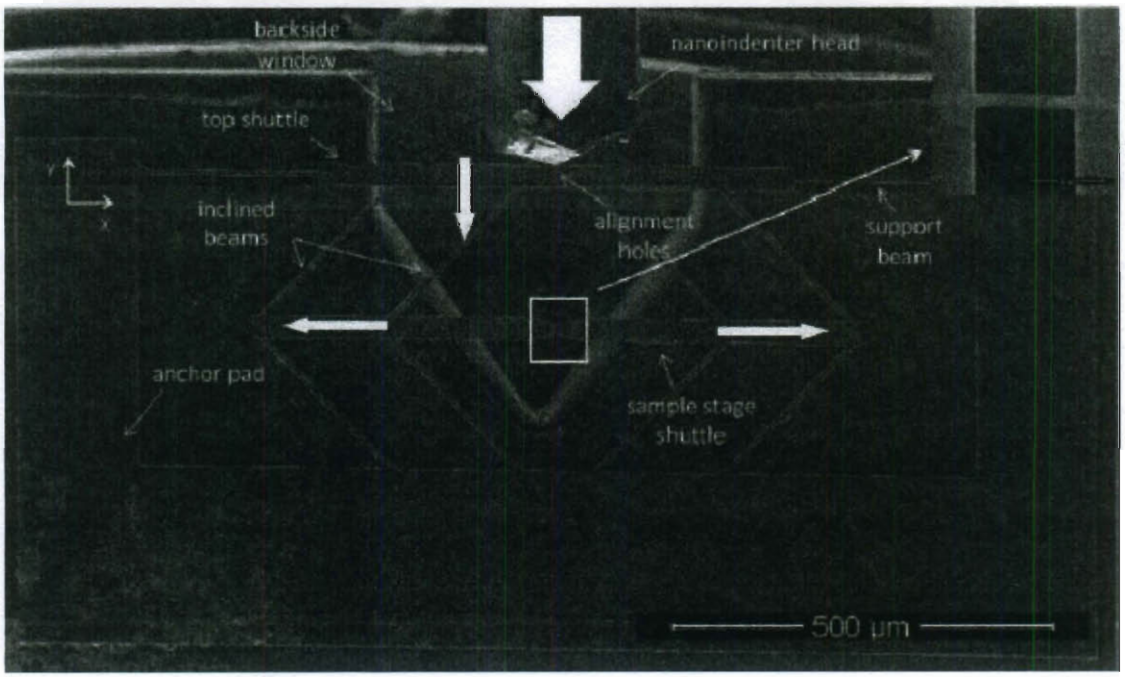

Figure 3-8 SEM image showing the nanoindentation on the micro mechanical device clamped with a gold nanowire. The block arrows show the direction of the movement of the indenter tip and the shuttles during the experiment. (Inset) close-up view of a nanowire sample.

The nanoindenter tip was first aligned with the top shuttle of the device in order to make sure that the sample-stage shuttles moved symmetrically. This was done with the help of alignment holes that had been incorporated in the device design. Once this was done, the electron beam was focused on the nanowire specimen in order to monitor its deformation as a function of load. The indentation was performed in the load-controlled mode, with the loading rate being held at a constant value of ~30 μN/s (corresponds to a strain rate of approximately 0.007/s). The maximum load applied on the device was 2 mN. Once this value was reached, the load was held constant for 0.5 s; this was followed by an unloading step at the aforementioned rate. A thermal drift correction hold step was performed at 10% of the maximum applied load for about 50 s in order to account for small amounts of thermal expansion or contraction in the test material and/or indentation equipment.

3.2.3. Results and Discussions

Figure 3-9 shows the SEM video frames for one of the five successful tests for gold nanowires with diameter ranging from 100nm-300nm. This gold nanowire specimen used for this experiment was about 15 μm long and had a diameter of ~280 nm. The gauge length of the specimen, i.e., the distance between the clamping points, was

ascertained by observation of the side profile of the sample across the sample-stage gap under a SEM and was found to be equal to ~2.85 μm.

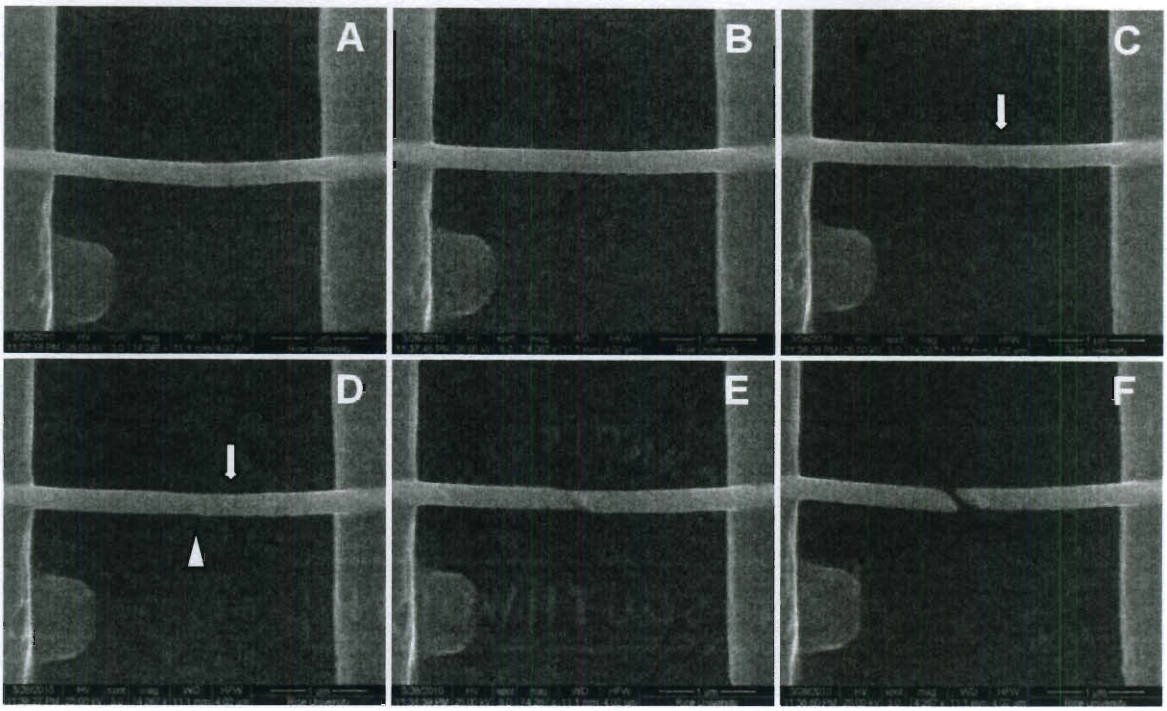

Figure 3-9 SEM video snapshots show a gold nanowire (D~280nm) during the tensile testing experiment: (a) initial relax state; (b) nanowire fully stretched; (c) the first slip band showed up, as indicated by the white arrow; (d) the second slip band showed up, as indicated by the white triangle, where necking occurred; (e) sample under significant plastic deformation; (f) sample finally broke at the second slip band position.

It might be noted that, this sample deformed in typical ductile manner, with significant necking and elongation stage. Nanowire showed slip bands when plastic deformation started and the necking and following slip appeared to follow the direction of the slip band, indicating the possible classical-dislocation-based deformation. However, in order to understanding the underlying deformation mechanisms, in situ TEM

experiment was needed and can be suggested as a future work. The slope of the load versus displacement curve before and after sample failure was used to determine the stiffness of the device in the presence of and after the failure of a mounted specimen [104]. By interpolation, using the value of the slope before sample failure, of the system stiffness (Ks) versus sample stiffness curve, the sample stiffness was determined. The values for force conversion factor C_F and displacement conversion factor C_D were subsequently determined [105], and the stress versus strain curve (see Fig. 3-10) was plotted.

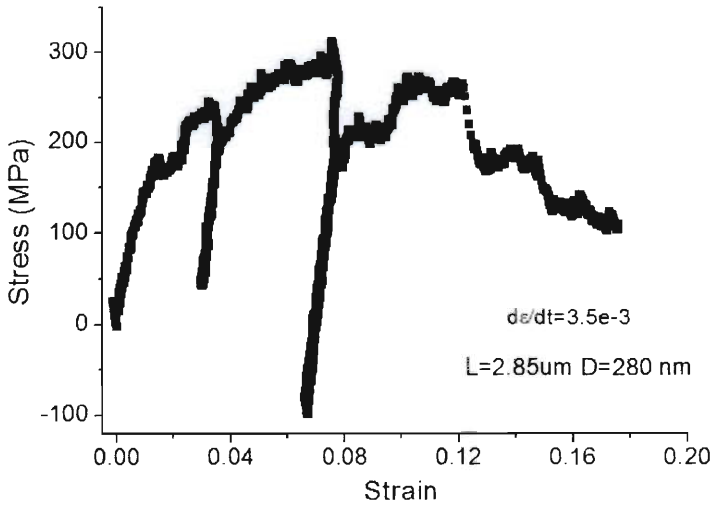

Figure 3-10 Stress versus strain curve for the aforementioned gold nanowire testing. Multiple loading-unloading had been conducted for measuring elastic modulus.

Similarly, we processed another four successful tests' data for gold nanowires with diameter ranging from 100nm to 300nm and summarized all five tests in Table 3-1.

Sample	Diameter (nm)	Eng Strength (GPa)	True Strength (GPa)	Breaking Strain	Strain Rate (/s)
Au NW	280	0.109	0.437	0.176	0.0035
Au NW	154	0.425	1.111	0.127	0.0032
Au NW	326	0.178	0.502	0.217	0.0026
Au NW	210	0.236	1.113	0.233	0.0025
Au NW	241	0.295	1.191	0.205	0.0032
Average	242	0.249	0.871	0.192	0.0030

Table 3-1 Summary of five successful tensile tests on gold nanowires using MMD

From the table, we found that, while the engineering strength of these samples were already much higher than that of bulk (about 80MPa [144]), their corresponding true strengths (considering the final diameter at necking area) were even higher. Considering the nanowire were grown in <111> orientation and tensile loading was along the wire axis, based on the measurement of the slip band angle (about 20-35degree with respect to wire axis), the slip plane could be (11-1) and slip along <112> direction. Therefore the Schmid factor will be 0.314 and the calculated CRSS values of these samples were ranging from 75-90MPa. In addition, all these samples underwent significant plastic elongation, with 12.7%-23.3% total strain, indicating that the nanowire broke in a typical ductile fracture mode. This quantitative data appear to be well correlated with in situ SEM video observation.

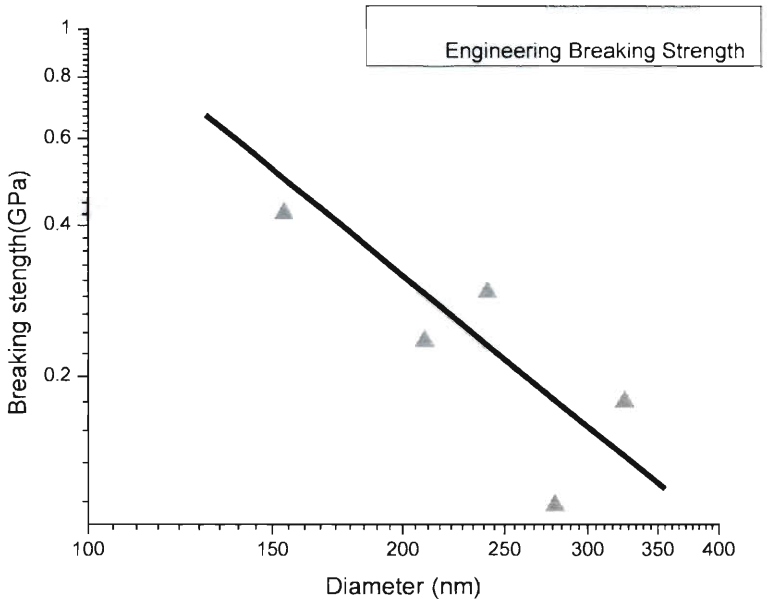

Figure 3-11 Size dependent mechanical behavior: Breaking strength (GPa) versus Nanowire diameter (nm) (both in log scale)

Finally, we plot engineering breaking strength versus sample diameter in Figure 3-11, and the curve clearly show the size effect, in short, smaller is stronger. In addition, by plotting the data point in log-log scale, we discovered similar relationship as the well-known Hall-Petch relation $\sigma_y \propto D^{-\alpha}$ [145] which illustrates the power law between material strength and sample sizes with a fitting parameter α. For pillar studies [3, 15, 17, 65, 67, 68, 86], linear curve fitting for compression strengths and 1-D sample diameters plotted in log scale can help to find out the scaling parameter α. Similarly, by fitting breaking strength and nanowire diameter in our case, as shown in the Figure 3-11, we've got a fitting parameter is 0.598, which is very close to the value of 0.61 for Au single

crystal [145], indicating the deformation for nanowires at this length scale might be still similar to that of micro and submicron pillar samples.

3.3. In Situ TEM Tensile Testing of Nickel Nanowires by Using the Micro Mechanical Devices

3.3.1. Introduction

Deformation mechanisms of metallic nanostructures, such as nanowires and nanopillars, have drawn considerable interests in the past decade due to their importance in building reliable nano-electronic devices and predicting the performance of nano-electromechanical-systems (NEMS) [36-38]. Recently, *in situ* TEM mechanical testing has emerged as a powerful tool to interrogate low dimensional metallic nanostructures, since it could provide detailed structural information at very high resolution during mechanical testing of such samples. This unique capability of monitoring sample's internal structural evolution in real time is considered to be very valuable in establishing better correlated structure-property relationship. Various *in situ* TEM mechanical testing methods have been developed in the past decade, such as nanoindentation tests of metal thin films [103], nano-compression tests of metal pillars [97] and bending/buckling tests [95-96] or resonances/vibration based tests of nanowires [88]. However, reliable and easy-to-interpret tensile tests remain to be rather challenging, owing to the difficulties associated with sample clamping, precise manipulation and alignment, as well as accurate measurement of load and displacement. Earlier efforts that had been made on developing *in situ* TEM tensile testing of low dimensional nanomaterials, such as AFM-cantilever or nano-manipulator assisted methods [98, 107, 108], oftentimes encounter inevitable drawbacks such as uncontrollable sample geometry and limited material selectivity, and problematic sample alignment and clamping. In order to develop a robust universal testing platform for samples of different materials and sizes/geometries, micro-electronic-

mechanical system (MEMS) has been considered as an ideal solution to perform nanoscale mechanical testing for various types of samples. Carbon nanotubes [101], bio-fibrils [102], thin films [103] and nanowires [98-99] have already been successfully tested by different MEMS devices. Also due to their small footprints, MEMS-based testing devices can naturally fit into SEM/TEM chambers for *in situ* mechanical testing [146]. We have recently designed and fabricated a silicon-based micro mechanical device (MMD) to perform quantitative *in situ* tensile tests on 1-D nanomaterials within a scanning electron microscope equipped with a quantitative nanoindenter [104-105]. This device was actuated mechanically with direct and independent measurement of load and displacement at high precision, allowing real-time observation of the deforming samples. Various samples, such as MWCNTs, Ni, Cu and Au NWs had been tested using the MMD platforms assisted by a quantitative nanoindenter inside a SEM [104-105, 147]. This platform has demonstrated its strength in providing continuous high resolution force displacement data, and versatile and precise load/displacement control, due to the simplified device structure and independent actuation and sensing mechanisms.

In the current work, we have successfully extended the usage of the novel micro mechanical device to perform quantitative *in situ* TEM tensile test on an individual nickel nanowire. Aided by a high resolution Nanofactory^{TM} TEM-Nanoindenter holder (Fig. 3-12a), individual nickel nanowires with diameter around 300nm were tested *in situ* and sample stress versus strain data were simultaneously obtained. The real time TEM images and diffraction analysis provided very useful insights into the origin of high strength and corresponding fracture mechanism.

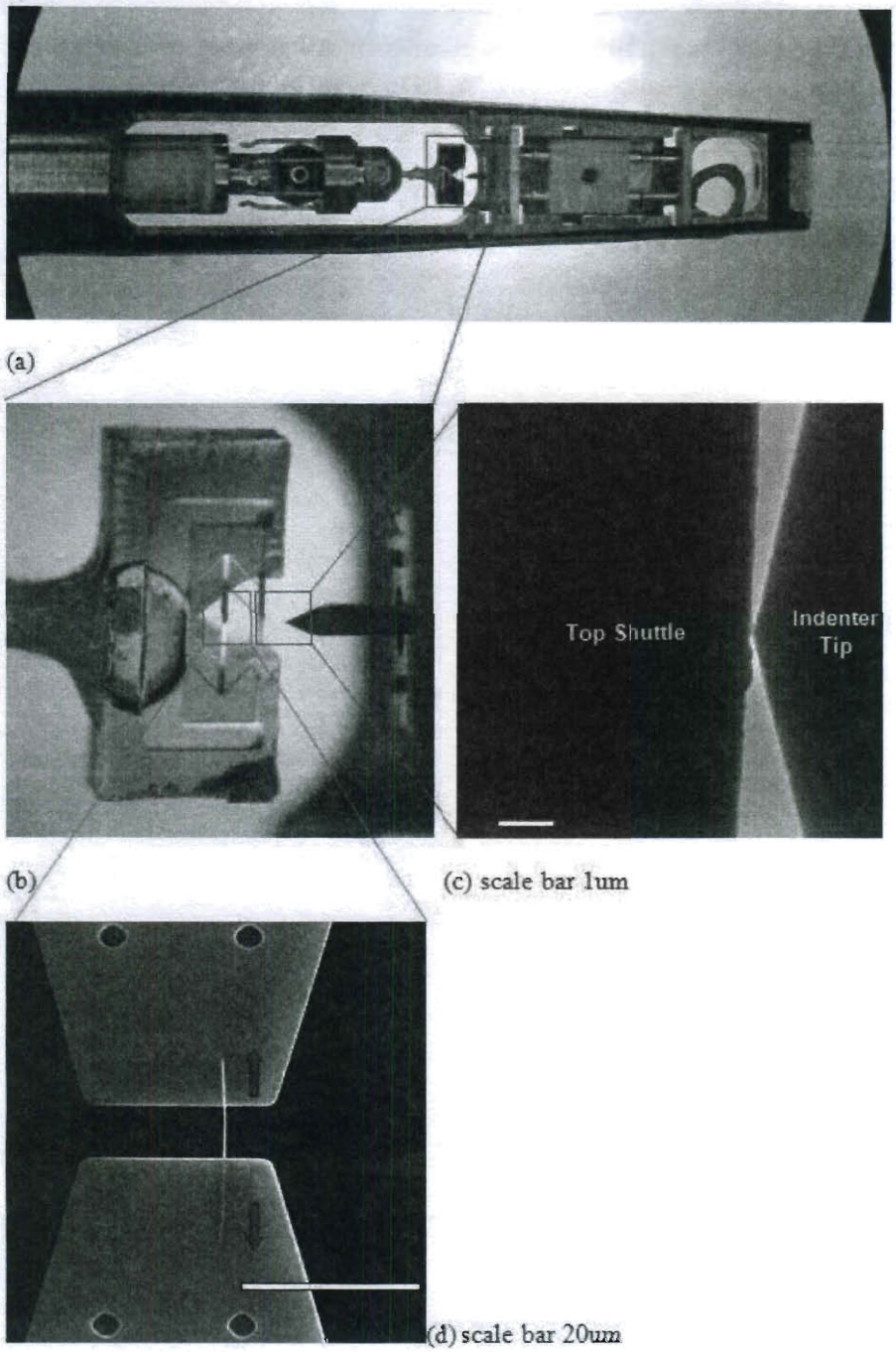

Figure 3-12 *In situ* TEM tensile testing using the MMD: (a) a micro mechanical device loaded in the Nanofactory^{TM} TEM-nanoindenter sample holder; (b) close-up view of the nanoindenter head toward the micro mechanical device (MMD); (c) a TEM image showing the alignment of the nanointender head with the center position of the top shuttle

beam of the MMD (scale bar 1μm); (d) a SEM image showing a ~300nm Ni nanowire clamped between two sample shuttles (scale bar 20μm)

3.3.2. Device and Sample

The design and fabrication of the micro mechanical device (MMD) had been described in detail elsewhere [104, 105] and will only be briefly discussed here. The MMD (Fig. 3-12b) was fabricated on SOI (Silicon on insulator) wafers using standard photolithography techniques. The device can convert the compression applied by a quantitative nanoindenter into uni-axial tension on samples clamped between the suspended sample stages through a simple "Push-Pull" mechanism (Figs. 3-12b to d). The force *vs.* displacement thus stress *vs.* strain curves (in conjunction with real time sample dimension measurements) of the sample could be derived from the force and displacement reading of the nanoindenter, with the help of Finite Element Analysis (FEA) [104] or a simple response subtraction method [105].

It should be noted that while the MMD was originally designed with the consideration of its usage in a transmission electron microscope (TEM) in mind [105], we still needed to modify the design layout considerably in order for it to work properly with the Nanofactory™ *in situ* TEM-Nanoindenter sample holder. The new design (as shown in Figs. 3-12 a and b) modifications include further decreasing the device size (device footprint decreased from 3mm x 2mm to 2.5mm x 1.2 mm) for better fitting into the highly restricted sample space in the holder (Fig. 3-12 a); decreasing the device weight by reducing the thickness of the suspended Si device layer (reduced from the original 9.5±0.5 μm to the current 6±0.5μm thickness) to improve the stability of the device when

it is being coarsely aligned by using the piezo-driven positioning stage in the holder or being set in motion during the actual testing; and finally revising the back-side window design to facilitate inTEM nanoindenter tip positioning while maintaining proper electron beam alignment. Fig. 3-12a shows an optical image of a Nanofactory^{TM} TEM-Nanoindenter sample holder loaded with a newly designed MMD.

Nickel nanowire samples tested in this study were fabricated by a simple aluminum anodic oxide (AAO) template assisted electrochemical deposition process [60]. Careful TEM diffraction analysis at multiple locations along the nanowire axial direction was performed, confirming these Ni nanowires possess single crystalline face centered cubic (f.c.c.) structure with [112] orientation along the wire axis [60]. Once the nanowires were released from the AAO template, a micromanipulator under an optical microscope or a nanomanipulator inside a SEM was used, depending on sample dimensions [105], to pick up an individual nanowire and place it between the sample stages. Sample clamping was realized by using either a conductive epoxy or a FIB deposited metal layer [105]. As shown in Fig. 3-12d, a ~300nm Ni nanowire was placed and clamped between two sample stages using conductive epoxy.

Once loaded with a nanowire sample, the MMD was then attached to a gold or tungsten rod with conductive silver glue to create an electrical conductive path in order to minimize charging issues. The rod with the MMD was then fixed on a copper cap which was subsequently attached to the ball head driven by a piezo-tube (left part in Fig. 3-12a). This set-up makes it possible for device motion in three dimensional spaces with respect to the nanoindenter head on the right side in Fig. 3-12a. The quantitative nanoindenter is equipped with a blunted diamond tip connected to a simple cantilever beam based force

sensor [148], which requires careful on-site calibration before actual experiment takes place. All experiments were performed inside a FEI^{TM} Tecnai G^2 F30 high resolution TEM, operated at 300 kV working voltage.

3.3.3. Results

Figure 3-13 demonstrated a successful *in situ* TEM testing of a ~360nm nickel nanowire. The sample gage length defined by the distance between two clamping point of the nanowire sample was determined to be ~ 15μm, using high resolution SEM images before transporting the sample loaded device into the TEM.

Displacement control was used in the actual test. The automatic quantitative nanoindentation test executed by the automatic function in the control software has a relatively small displacement range of ±770nm. However, for this specific ~360nm-diameter Ni NW, preliminary automatic test indicated that the sample remained in elastic region after reaching the full ±770nm indentation displacement limit. In order to perform a complete tensile test up to fracture, we have to first perform a manual indentation by using the coarse movement function, which has tens to hundreds of microns in displacement range and was typically utilized for sample/device manipulation and alignment. During this coarse movement, applied force can still be recorded by the nanoindenter force sensor, while the sample displacement can be monitored through the real time TEM videos. By carefully performing manual indentation until sample under larger elastic deformation, an automatic indentation experiments was then engaged and continuously stretched the nanowire sample until sample coming into plastic deformation and final fracture. Fig. 3-13b showed the sample right before fracture, which was under

significant plastic deformation (as indicated by the red double-arrows). Finally the sample suddenly broke without observable necking process (Fig. 3-13c).

Post-data analysis was executed to convert the original nanoindenter force versus displacement reading from the testing into sample stress versus strain curve. This conversion relationship was obtained by fitting and comparing the slopes of empty device and initial linear region of the actual test, and the details can be found in [105]. By converting the indenter force-displacement data into sample force and displacement data, together with the geometry (diameter, elongation of the nanowire) information from the video, the stress versus strain curve can be obtained (Fig. 3-13d). It might be noted that, due to the limited range (±770nm) of automatic indentation,manual loading was used prior to automatic testing in order to break the sample. The insert of Fig. 3-13d shows the stress versus strain data during automatic testing stage.

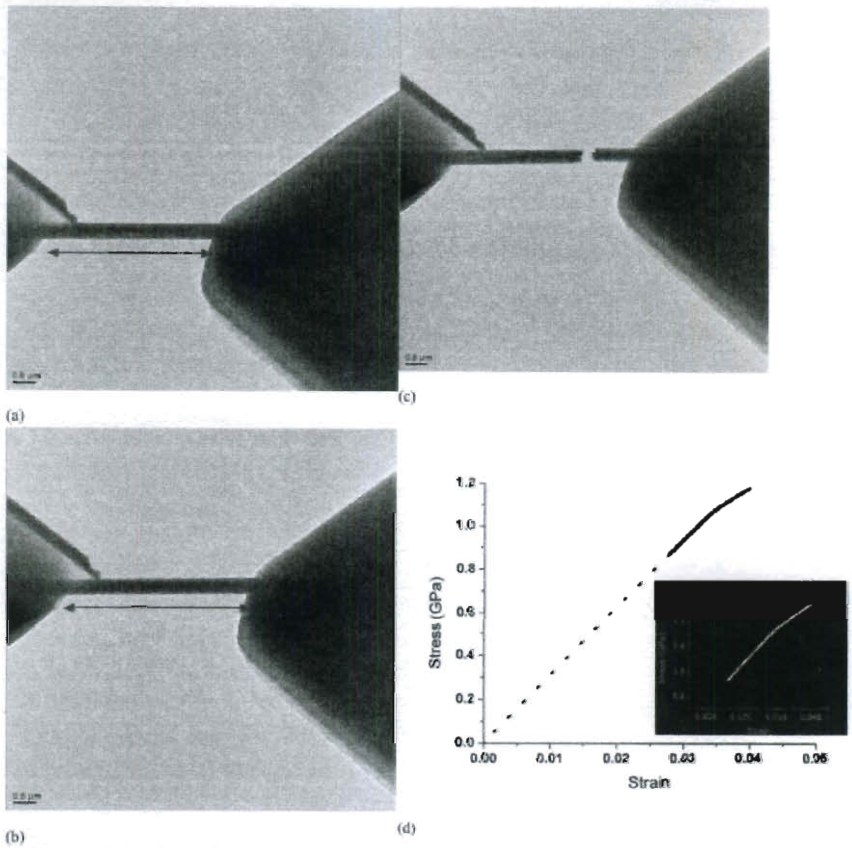

Figure 3-13 TEM image frames showing a quantitative tensile test for a ~360nm-diameter nickel nanowire: (a) before loading; (b) right before breaking; (c) after breaking; (d) the corresponding sample stress versus strain curves (insert shows magnified view of the curve during automatic testing stage)

In Fig. 3-13d, the specific nanowire sample experienced a total ~ 4% strains before final fracture. Typical plastic flow behavior was not observed from the stress-strain curve, but sample did show a slope change (slightly lower) at about 1.1GPa, which may indicate the onset of the local plastic deformation activities. However, the incipient plasticity in this sample might occur at a much lower strain level that is possibly below the detection limit of the current technique. The sample breaking strength is about

1.2GPa, which is much higher than bulk Ni (140-195 Mpa [144]). According to the earlier work done on similar Ni NW samples [105], the measurement using this setup appears quite consistent with the results from earlier *in situ* SEM measurements.

3.3.4. Discussions

Finally, by watching the movie corresponding to the test in Figure 3-13, dramatic contrast changes within the strained nanowire sample imaged under bright-field TEM imaging conditions were clearly observed (Fig. 3-13 a-c), until the sample eventually broke at position within the sample region that underwent the significant contrast changes. Similar phenomena had been reported, such as the *in situ* testing of ZnO nanowires by Espinosa et al. [149] in which several fringes was evident in the bright-field TEM image and sample did break along one of such fringes. It was believed that the local changes observed in the contrast of the TEM images might be related to atomic distortions resulting from stress concentrations [149]. In order to verify this assumption, and reveal the underlying deformation mechanism, high magnification TEM imaging can be performed during the test. For example, with appropriate orientation, dislocation networks and their interactions with excellent contrast maybe observed in real time bright-field TEM image (Figure 3-14a). For the Ni NW tested in Fig. 3-13, higher magnification image showed very clear fracture morphology (Figure 3-14b), which convincingly verified the earlier suggestion of brittle fracture based only on stress-strain curve and low magnification video of the deformation and fracture process. This also agreed well to the results of earlier SEM experiments [105]. Additionally, select area diffraction (SAD) analysis, a unique and important capability of TEM, could also offer

very useful insights into crystalline structure evolution such as possible phase transformation [19, 150] during the mechanical testing. In Fig. 3-14c, we performed SAD for the broken Ni NW sample (as shown in insert, corresponding to the right part in Fig. 3b), and it showed that the residual nanowire remained as f.c.c structure in [112] orientation (R_2/R_1=~1.3, =~78°, Zone axis (345)). Interestingly, additional diffraction spots were also observed, which may indicate that the fracture zone might undergo some local re-orientations in the crystalline structure.

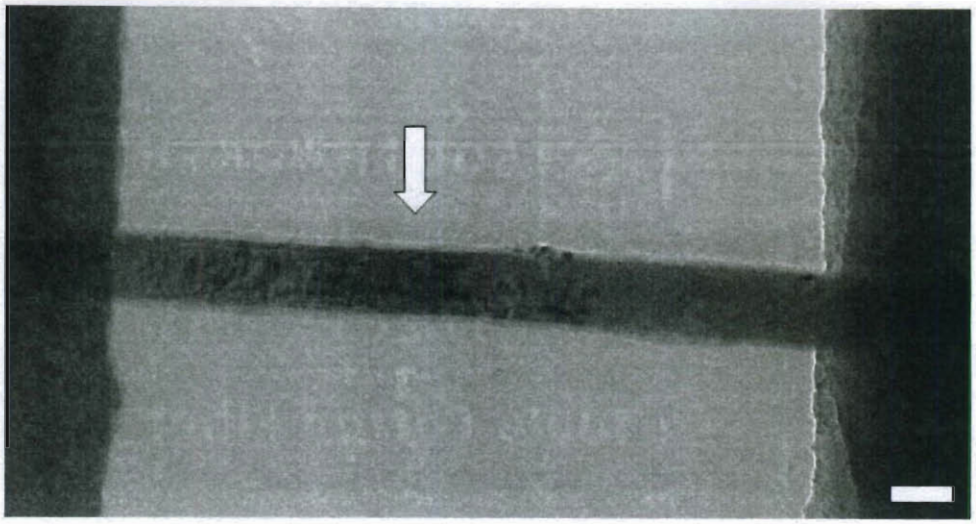

(a)

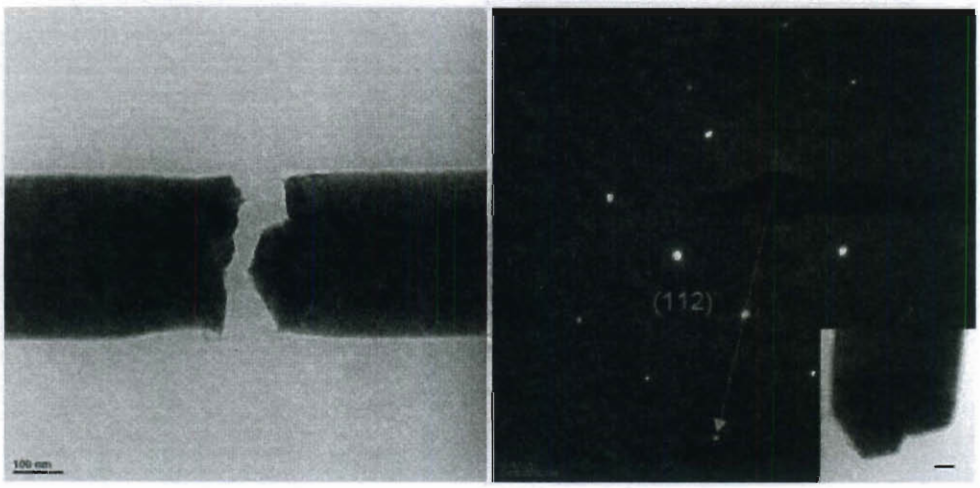

(b) (c)

Figure 3-14 High magnification TEM imaging and diffraction analysis: (a) a ~300nm nickel nanowire under tension, the contrast at the stress concentration area (indicated by the white arrow) might show the dislocation network (scale bar 200nm); (b) close-up view of the fracture morphology of sample broken in the test of Fig. 2 (scale bar 100nm); (c) real time TEM select area diffraction (SAD) analysis showing the crystalline structure of the broken nanowire sample (as shown in the insert, scale bar 50nm). The arrow indicates the wire growth direction

3.3.5. Summary

Here, we have demonstrated that the recently developed micro mechanical device could be utilized to perform intriguing quantitative mechanical testing of nanoscale samples inside a TEM assisted by a high precision TEM-nanoindenter holder. With careful consideration and improvement in the design and experimental setup, metallic nanowires were successfully tested and such *in situ* TEM experiment showed its strength and potential of not only ensuring accurate and valid measurement via real time video monitoring but also revealing the internal structural evolution while providing precise force displacement measurement. Therefore, the reported *in situ* TEM setup could effectively facilitate the construction of the much desired structure-(mechanical) property relationship with quantitative understanding at the nanoscale, with the potential of testing a wide variety of different low dimensional nanoscale materials.

Chapter 4

In Situ Tensile Testing of Ultrathin Gold Nanowires (Diameters ~5-15nm)

4.1. Surface Dislocation Nucleation Mediated Deformation and Ultrahigh Strength in Sub-10nm Gold Nanowires

When a crystal's dimension reduces to nanometer length scale, the strength of the sample is expected to approach the ideal strength of a defect free crystal. The deformation and the ultrahigh strength attained were predicted to be controlled by surface dislocation nucleation rather than by dislocation multiplication/interaction as in bulk crystals. Here, we show that by performing in situ quantitative tensile tests on individual <111> single crystalline ultrathin gold nanowires (diameter ~7-10 nanometers), significant load drops were observed in corresponding stress-strain curves suggesting the occurrence of dislocation nucleation. Subsequent high resolution TEM (HRTEM) imaging demonstrated that plastic deformation was indeed initiated and dominated by free surface dislocation nucleation, mediating ultrahigh yield and fracture strength in gold nanowires.

4.1.1. Introduction

Size dependent plasticity and fracture behaviors of one-dimensional metallic nanowires offer exciting potentials for revealing fundamental mechanisms of deformation and failure, as the length scale of metals approaching atomic spacing. Uni-axial

compression of focus ion beam machined single crystalline metallic pillars with tens of micrometers to hundreds of nanometers in diameters showed strong size effects with much higher yield stress for smaller pillars without the presence of strain gradients [67, 68]. A conceptual framework of "dislocation starvation" [18] was thought to be responsible for this apparent size dependent behavior. The "mechanical annealing" phenomena [97] observed in compression of Ni pillars inside TEM suggested that gliding dislocation could leave crystal more rapidly than they multiply which leads to a dislocation-starved state, requiring very high stress to nucleate new mobile dislocations in such a small crystal volume. When crystal size further reduces to tens of nanometers and below, surface dislocation nucleation is predicted to play a more critical role in controlling plastic deformation and subsequent fracture behaviors [3, 19]. Unfortunately, direct experimental evidence of such surface dislocation nucleation aspects of small scale plasticity remains elusive and requires careful quantitative *in situ* investigations.

Early studies on quantitative mechanical testing of 1-D nanostructures were primarily carried out *ex situ*, using techniques such as nanoindentation [15], resonant oscillation [88], and AFM deflection [16] tests. They generally lack real time structural monitoring, which did not permit a one-to-one correlation between mechanical data and internal structural evolution. Recently, *in situ* mechanical characterizations of individual nanowires with diameters from tens to hundreds of nanometers inside transmission electron microscopes (TEM) were realized under various loading geometries, such as bending [95], buckling [96], and compression [97]. However, the most efficient and easy-to-interpret tensile testing method for measuring intrinsic mechanical properties of exceedingly small nanowire samples inside TEM, poses significant challenges due to

difficulties associated with sample clamping, alignment and accurate measurements of load and displacement. Researchers had developed various MEMS devices to perform *in situ* tensile tests on metallic (e.g. Au, Pd, Ni) nanowires and carbon nanotubes [100-101], biological fibrils [102], and gold nano thin film [103]. However, the diameters of tested nanowires using MEMS stages were usually in the range of tens or hundreds of nanometers. In order to test metallic nanostructures with sub-10nm diameter, one had to prepare samples *in situ* by using either mechanically controllable break junction technique (MCBJT) [106] or nanometer tip-substrate [107] / tip-tip [108] contact-then-withdraw technique to form nano-sized metal junction samples. Unfortunately the crystalline structure and orientation of sample prepared by these methods were not well-controlled, and sample diameters were non-uniform (ranging from a few Armstrong to a few microns). These drawbacks hindered quantitative characterization and understanding of the deformation and fracture mechanisms for metals at the sub-10nm scale.

In this part of work, we show for the first time *in situ* quantitative tensile tests of gold nanowires with diameter less than 10nm. Rather than pulling randomly formed nanosized gold nano-junction, we successfully clamped individual pre-fabricated free-standing nanowires with well-controlled crystalline structures and orientations onto the AFM cantilever which acted as the force sensor, and performed quantitative tensile tests directly inside a HRTEM (Fig. 4-1).

4.1.2. Sample and Experimental Setup

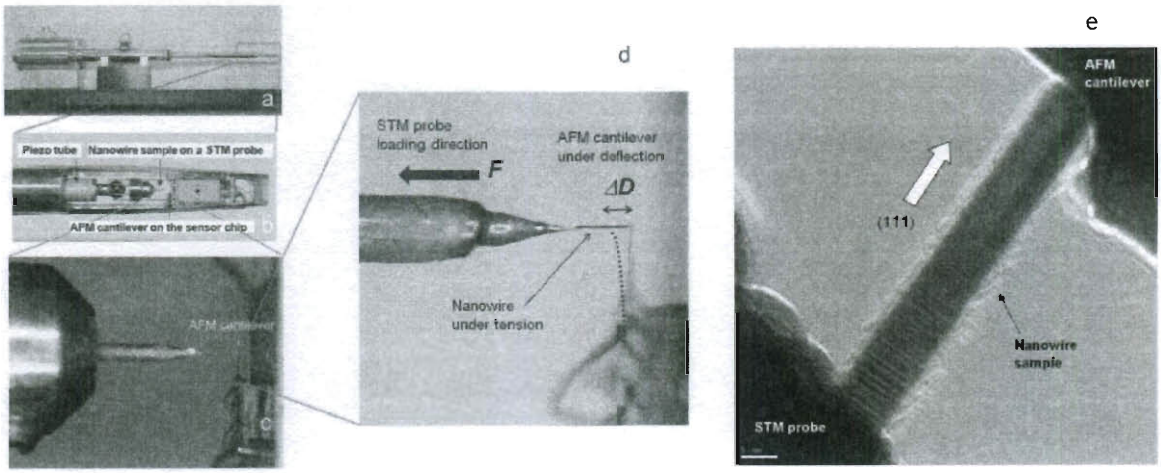

Figure 4-1 Experimental set-up and materials preparation: (a) The NanofactoryTM TEM-AFM holder; (b) and (c) zoom-in image showing the holder configuration; (d) illustration of the quantitative testing configuration with the AFM cantilever as the force sensor; (e) HRTEM image of a 7 nm nanowire shows the lattice fringes, indicating the nanowire grows along <111> direction (scale bar 5nm)

Ultrathin gold nanowires with uniform diameter ranging from 7 to 10nm were used (Fig. 4-1 e) in this study and they were chemically synthesized by the reduction of $HAuCl_4$ in oleic acid (OA) and oleylamine (OAm) [41]. These high-aspect-ratio nanowires had lengths ranging from tens nanometers up to a few microns. They were also verified to be single crystal in <111> growth direction, with measured average lattice fringe spacing ~0.23nm (corresponding to the {111} lattice spacing of gold) from their high-resolution TEM images (Fig. 4-1 e).

Quantitative tensile tests were conducted by using a Nanofactory^{TM} TEM-AFM sample holder (Fig. 4-1 a) and the TEM samples were prepared by adhering ultrathin

gold nanowires onto a gold or tungsten STM probe using conductive silver glue. Then the STM probe with Au nanowires was loaded into the Nanofactory^{TM} TEM-AFM sample holder (Fig. 4-1a) and manipulated by a piezo-driven head (Figs. 4-1 b-c). The sample clamping was facilitated by coating the tip of the silicon AFM cantilever with a thin (tens of nanometers) adhesive layer, such as silicon oxide. During tensile tests, an AFM cantilever beam with known spring constant k = 4.8 N/m was deflected by an individual nanowire sample pulled by the piezo tube under displacement control mode (Fig. 4-1 d). Sample elongation and the change in diameter were monitored directly via real time TEM imaging and the force was calculated by the recorded deflection of the AFM cantilever. A linear relationship was assumed between the deflection and force ($F= k*\Delta D$), considering small deflection. In all experiments, the stationary e-beam-blocking bar was inserted as a reference marker for all displacement measurements. All experiments were performed inside a FEI^{TM} Tecnai G^2 F30 high resolution TEM, operated at 300 kV working voltage. It is also worth noting that no current was passed through samples and very low dose electron beam (~1 A/cm^2) were used in order to reduce the electron irradiation induced heating in all of our experiments.

4.1.3. In situ quantitative tensile measurement inside TEM

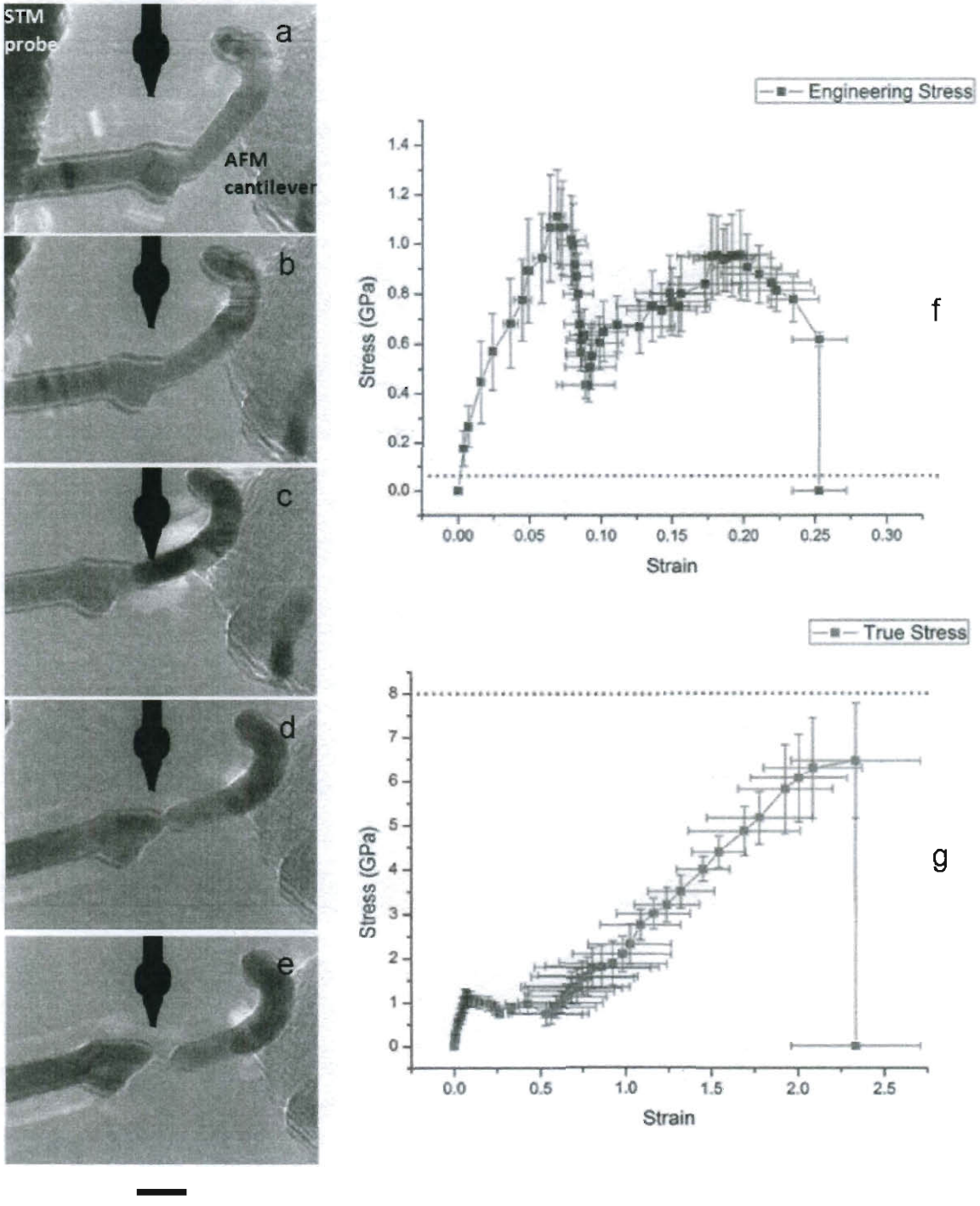

Figure 4-2 Quantitative tensile test of an ultrathin nanowire (diameter ~10nm). TEM image frames (a-e) showing the testing process (scale bar 10nm); corresponding (f)

engineering and (g) true stress versus strain curves for the test shown in (a-e); error bars were obtained by multiple measurements from nanowire lengths and AFM cantilever deflections, as well as the imaging area movement corrections. Blue line in (f) indicates the fracture strength (~100MPa, [144]) of bulk gold, and the red line in (g) indicates the theoretical strength of gold (~8GPa, [1]).

In Figs. 4-2 a-e, an ultrathin Au nanowire (diameter ~10nm and length ~70nm) was deformed and fractured under tensile loading. Figure 4-2 f demonstrated the corresponding engineering stress and strain data obtained by measuring cantilever deflections and sample elongations. The nanowire experienced an impressive ~26% total engineering strain before final failure. During plastic deformation, the nanowire kept necking down to a point and formed atom chains at the final stage right before fracture. Since actual instantaneous diameter of the deforming nanowires could be measured using high resolution TEM imaging during tensile tests, the true stress versus strain curve (Fig. 4-2 g) was also obtained. Clear size effect in fracture strength was observed for ultrathin Au nanowires with engineering strength of ~620MPa, much higher than fracture strength of bulk gold (~100MPa [144]). Taking into consideration of the dramatic cross-section area reduction due to necking, the corresponding true fracture strength was estimated to be ~7 GPa! This value is very close to the ideal strength of gold crystal (~8GPa [1]), and higher than most of the reported experimental strength data (ranging from 0.8-6GPa) for Au nanowires with larger diameters [16]. This true fracture strength value is also comparable to experimentally measured strength of single Au atomic chain (~13GPa)

[151], owing to the extensive necking process experienced by the Au nanowire before fracture.

More interestingly, very significant load drop in the stress-strain curve (Fig. 4-2 f) was observed after the initial elastic deformation, where the engineering stress of the Au nanowire dropped from ~1.1 GPa down to ~460MPa. The measured yield stress of ~1.1 GPa is extremely high for Au, comparable to theoretical prediction of ideal shear strength from density functional theory (DFT) calculations, i.e., 850 MPa–1.4 GPa, depending on the loading mode [152]. The ultrahigh yield strength of the ultrathin gold nanowire is attributed to lacking of pre-existing mobile dislocations in the ultra small nanowire (Figs. 4-2 a and 4-3 b) [145].

Furthermore, the stress drop was quite abrupt and did not seem to be a random event, as similar load drop was also observed in another quantitative tensile test of similar Au nanowire, as shown in Fig. 4-3. By monitoring the displacement of the AFM cantilever with respect to the red-color reference bar (also acting as the scale bar) in the video, we observed clearly that the sample experienced a similar load drop to that shown in Fig. 4-2. Corresponding engineering stress versus strain curve for this test was plotted in Fig. 4-3 a. It should be noted that true stress versus strain curve was not plotted here due to the low magnification/resolution (diameter measurement will not be very accurate in this case). Additionally, when load drop occurred, corresponding image of the sample again showed rapid change of image contrast near the necking region (see Fig. 4-3 b), indicating possible surface dislocation nucleation events.

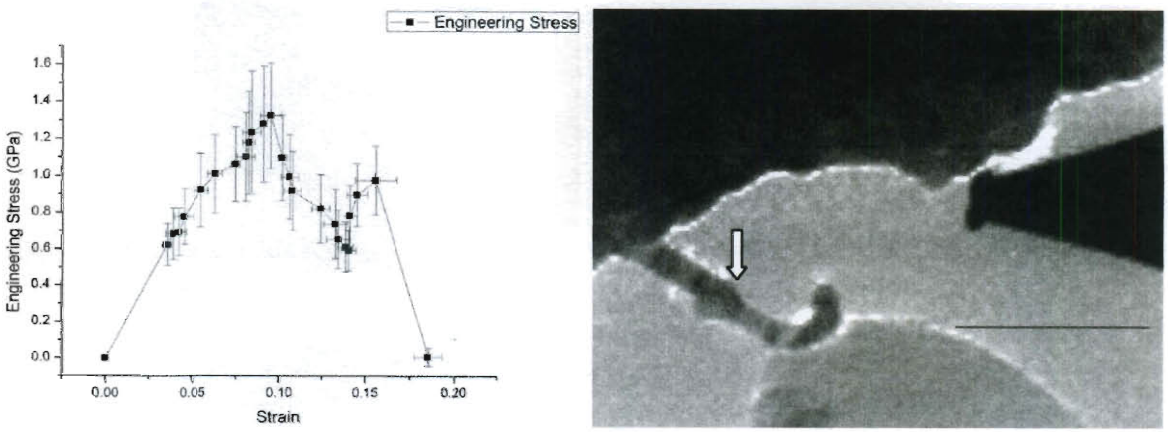

(a) (b)

Figure 4-3 Low-magnification tensile test of an ultrathin gold nanowire clearly showing the load drop (a) low-magnification tensile test with corresponding engineering stress versus strain curve; (b) the image showed the sudden contrast change near the necking region (under the white-color arrow) when load drop occurred (scale bar 100nm)

It is believed that the large load drop was associated with the onset and rapid succession of multiple dislocation activities, including nucleation and subsequent slip propagation across the nanowire. This dislocation nucleation induced load drop was recently predicted in molecular dynamic simulations of tensile tests of gold nanowires, and it was further suggested that slip nucleation in these f.c.c. nanowires is essentially a surface phenomenon and the Shockley partials are the major contributors in this process [3, 4]. The significant load-drops in uni-axial stress-strain curves could only be experimentally observed if the initial sample is dislocation free achieved either by fabrication or "mechanical annealing" processes. Thus our experiments provide the first direct evidence for the predicted load drop in nanowire tensile tests.

4.1.4. HRTEM analysis of an ultrathin gold nanowire under tensile loading

To fully reveal the underlying deformation mechanisms associated with the observed significant load drop phenomenon, specifically the exact location of the dislocation nucleation event, qualitative tensile tests in high resolution transmission electron microscopy (HRTEM) mode were performed using a shorter nanowire in order to ensure high quality imaging of the deforming region. Figs. 4-4 a-h showed the deformation process of a single crystalline gold nanowire (~30nm in initial length) with the same <111> growth orientation. The loading rate was slightly slower for better image quality (at ~0.2nm/sec and strain rate ~0.001/sec). The sample was pulled in the same uni-axial loading direction along <111> nanowire axis. The nanowire first experienced a prolonged elastic deformation region with no apparent lattice structural change (Figs 4-4 a-b), which correlates well with the earlier quantitatively measured elastic strain of a few percent (Fig. 4-2 f). The onset of the plastic deformation was indicated by the sudden appearance of a dislocation slip trace apparently emitted from the nanowire surface as marked in Fig. 4-4 c. Due to the extremely small sample volume available, the nucleated dislocations were thought to slip across the nanowire swiftly. By measuring the angle between the slip trace and the wire axis (~19.5 degree as in Fig. 4-4 c), it was confirmed that the dislocation slip occurred on another {111} plane. This observation along with earlier observed load drop in the stress-strain curve of similar Au nanowire clearly demonstrated the onset of plasticity in these ultra-thin nanowires with very few pre-existing dislocations was indeed dominated by surface dislocation nucleation. With further deformation, more similar dislocations were emitted from both sides of the nanowire surfaces and then slipped quickly across the nanowire with no apparent

interactions along intersecting {111} planes to gradually form a necked region in the middle section of the nanowire (Figs. 4-4 d-g). The neck kept reducing its thickness with nucleated surface dislocations continuously exiting the nanowire along the corresponding slip planes, giving rise to extensive plastic deformation and significant cross-section area reduction leading to the final fracture of the nanowire.

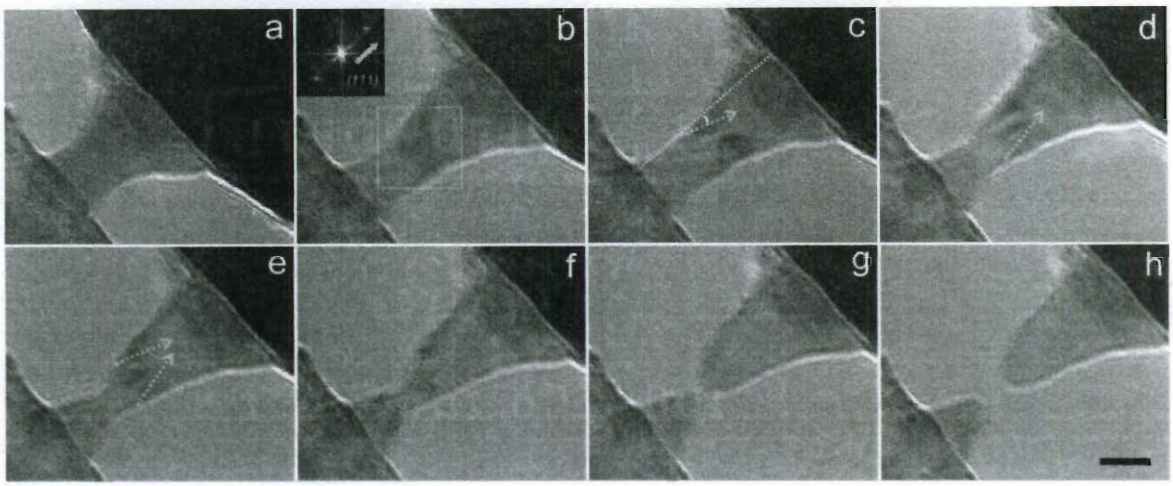

Figure 4-4 HRTEM images of a short gold nanowire under tensile loading: After the elastic deformation region (a-b), initial surface dislocation nucleation was indicated by the arrow in (c) with the approximate edge profile of nanowire marked by the dotted line. Arrows in (d, e, f) indicates more similar surface dislocations emitted from both sides of the nanowire surfaces, and a neck (e-g) was formed in the middle section of the nanowire until final fracture in (h). Insert in (b) shows a FFT image calculated from the image inside the white square, showing the wire orientation.

Although the exact slip directions of these surface dislocations moving on corresponding {111} slip planes could not be directly determined from our experiments, it is well known that the {111}<110> perfect slip occurs through two {111}<112> partial

slips on the same {111} planes in f.c.c. crystals. For <111> oriented Au nanowires under tensile deformation along its wire axis, the Schmid factor for a leading Shockley partial (0.31) is higher than that for the trailing one (0.16) [3, 4]. This basically implies that it is difficult for the trailing partials to follow its leading counterparts and the observed surface dislocations are most likely to be partial dislocations moving along <112> directions.

4.1.5. Conclusion

In summary, ultrahigh yield and fracture strength close to theoretical predictions were measured in <111> oriented single crystalline Au nanowires with sub-10 nm diameters. Quantitative *in situ* tensile experiments inside a HRTEM unambiguously revealed the underlying processes of the necking formation and subsequent fracture mediated by surface dislocation (Shockley partials) nucleation in ultrathin gold nanowires. The direct observation of this unique mechanism confirmed the long expected but never experimentally verified critical roles played by surface dislocation nucleation in plasticity and fracture of metal nanowires.

4.2. Brittle and Ductile Fracture of Ultrathin Gold Nanowires

Fracture of metals at the nanoscale and corresponding failure mechanisms have recently attracted considerable interests. However, quantitative in situ fracture experiments of nanoscale metals were rarely reported. Here we show that, under uni-axial tensile loading, single crystalline ultrathin gold nanowires may fracture in either "brittle" or "ductile" modes, displaying distinctively different fracture morphologies and ductility. In situ high resolution transmission electron microscopy (HRTEM) study suggested that the unexpected brittle fracture was closely related to the observed twin structures, which is very different from partial dislocation nucleation/slip mediated mechanism in ductile fracture mode. Molecular dynamics (MD) simulations further revealed the processes of shear-induced twin formation due to sample misalignment and damage initiation at the twin boundary/free surface interface, confirming the experimentally observed differences in fracture morphology and ductility. Finally, a fracture criterion based on competition between twin formation and partial dislocation nucleation/propagation as a function of misalignment angle was discussed.

4.2.1. Introduction

As modern electronic devices continue shrinking critical feature sizes, extensive research has been focused on the development and implementation of next-generation interconnects to incorporate increasingly small feature sizes with high performance and reliability in a cost-effective manner. While current lithography may encounter a barrier when the critical dimension was approaching sub-20nm [39], ultrathin metallic nanowires [40] have been recently fabricated via bottom up methods and may potentially satisfy the

stringent nano-electronic device requirements. Ultrathin gold nanowire is particularly promising candidate for future interconnects and as active components in nanoscale electric and mechanical devices [38, 41] owing to its excellent electrical and mechanical properties and desired chemical inertness. However, full realization of ultrathin gold nanowires' potential in nanoscale electrical and mechanical devices requires a comprehensive reliability study of their fracture behaviours and corresponding mechanisms, which is yet to be explored.

In the past decades, significant progresses have been made in quantitatively measuring mechanical properties of metallic nanostructures (see Chapter 1). However, quantitative understanding of sub-20nm metallic nanowire fracture behaviours, which requires direct correlations between mechanical measurements and corresponding substructure evolutions, remains elusive. The preferred uni-axial tensile fracture experiments for high aspect ratio ultrathin nanowire samples remains quite challenging for these exceedingly small samples due to sample handling and clamping issues. Typical clamping methods involving focus ion beam (FIB) deposition may introduce significant surface contamination [109] and local heat-induced spot welding could potentially damage the initial sample structures and morphologies [110-112]. Using recently developed cold welding techniques for ultrathin gold nanowires [41], we manage to overcome these difficulties and are now able to perform robust individual nanowire picking-up and clamping procedures repeatedly, allowing systematic study of tensile fracture behaviours for ultrathin gold nanowires.

4.2.2. Experiment

Cold-welding assisted sample picking-up and clamping

The individual nanowire was picked up and clamped onto a TEM-AFM holder (NanoFactory™ Instruments, Sweden), assisted by recently discovered "cold welding" technique [51]. The gold STM tip on one side was first etched further to produce many sharp tips on top of it, and the AFM tip on the other side was also coated with a very thin gold film on which many gold asperities were formed. These nanoscale features served as the clamping spot for cold welding process that securely clamped the ultrathin gold nanowire samples for subsequent tensile testing (Figure 4-5).

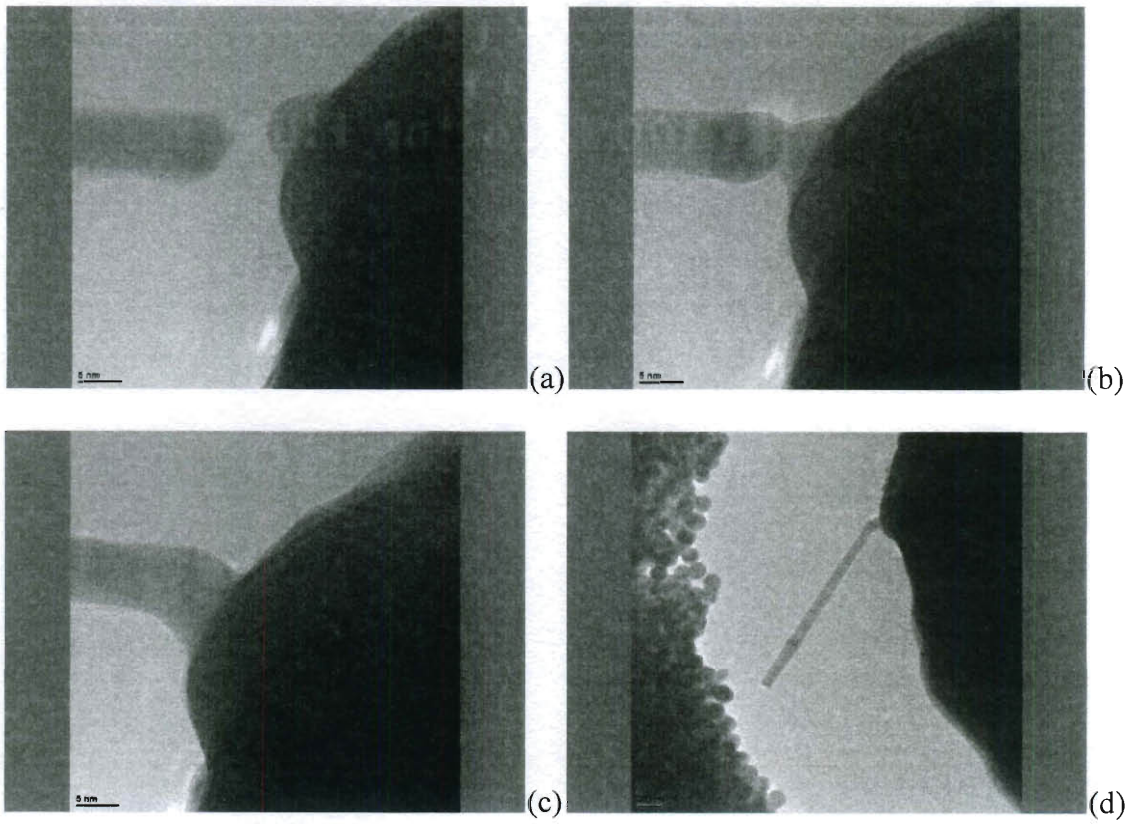

Figure 4-5 Cold-welding clamping of an ultrathin gold nanowire

Quantitative *in situ* TEM tensile measurement

Total 22 sub-15 nm <111> gold nanowires were successfully tested using a Nanofactory^{TM} *in situ* TEM-AFM sample holder (see Figure 4-1), in which a silicon AFM cantilever with known spring constant acts as the force sensor and a gold STM probe driven by a piezo stage acts as the actuator. The nanowire samples were clamped between the gold STM probe and the silicon AFM cantilever through the in situ nanomanipulation and cold-welding assisted sample clamping. The basic testing geometry and principle has been illustrated in [51]. However, in earlier work the force and displacement data were extracted based on the direct measurements from the video frames. Here we have been able to obtain force and displacement data with high precision and sampling rate by taking advantage of an integrated MEMS-based sensor [148] after careful calibrations.

Stress and strain calculation

Instead of relying on direct measurements of image frames in video, we could generate stress-strain curves using the force and displacement output from the TEM-AFM holder equipped with a highly sensitive MEMS-AFM sensor [148] with very high data acquisition rate. The engineering stress was derived from force (F) over the measured initial cross-section area. The engineering strain was obtained using the elongation of the nanowire sample between clamping point over the initial gauge length (L_0), $\varepsilon=\Delta D/L_0$. Since the direct displacement reading was the STM withdrawing distance (D_S), the actually elongation of nanowire ΔD should equal the STM withdrawing displacement minus the AFM cantilever deflection distance (D_A, could be obtained by F/k, where k is the spring constant of the cantilever and F could be obtained directly),

$\Delta D=D_S-D_A$. It should be noted that, both D_S and D_A were carefully calibrated based on the actual video frames of individual tensile experiment.

4.2.3. Results

Figure 4-6 shows a typical tensile test of a <111> ultrathin gold nanowire sample (~7.5nm in diameter and ~114nm in length) prepared by nanomanipulation and cold welding processes. The nanowire was stretched toward the right side by the STM probe at the constant loading rate about 0.3nm/s. This particular sample experienced extensive plastic deformation (Figs. 4-6 c-e) and formed a neck (Fig. 4-6 e, as indicated by the white arrow) in the middle section before final fracture. In Fig. 4-6 f, it was found that the fracture surface of the left part of the nanowire formed a sharp tip when imaged at higher resolution.

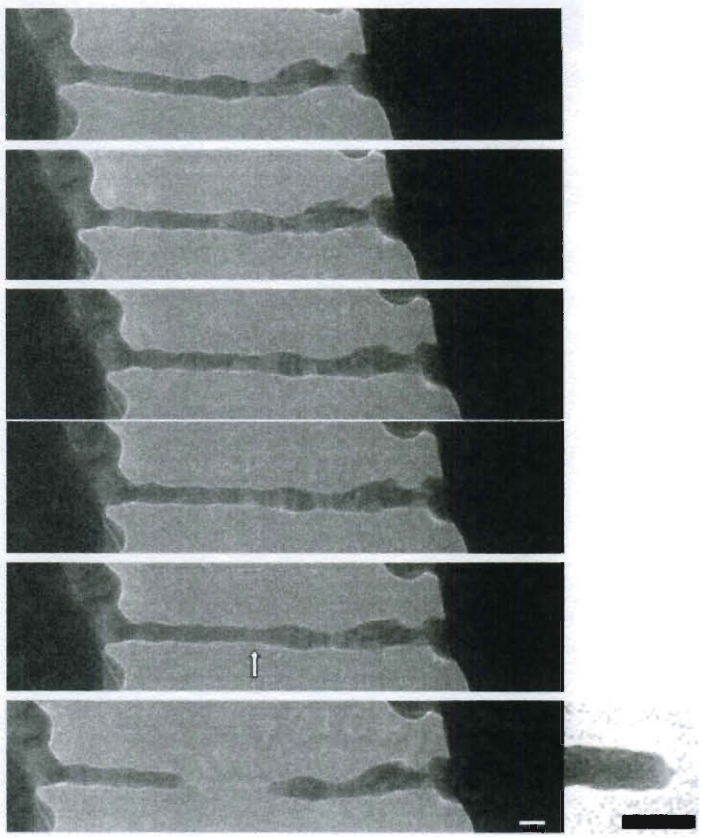

(a-f)

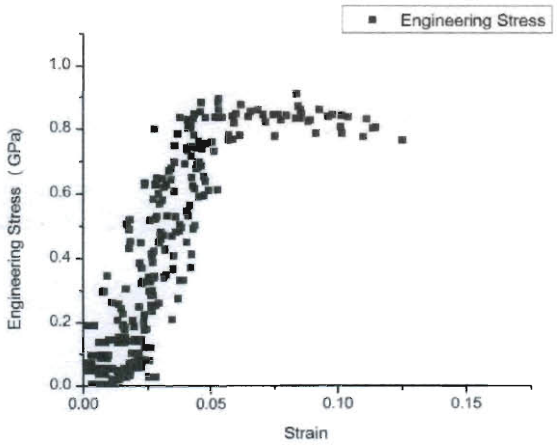

(g)

Figure 4-6 A typical in situ tensile test of a long ultrathin gold nanowire fractured in ductile mode: (a) nanowire at the initial relaxed state; (b) nanowire under initial loading; (c-e) nanowire underwent plastic deformation, thinning and necking process; (f) final

fracture stage, left side of the sample (as shown in the right insert image, scale bar 10nm) returned to no-force state, with a residual sharp tip, along with the AFM cantilever (scale bar 10nm); (g) the corresponding engineering stress-strain curve.

The corresponding stress versus strain curve was plotted in Fig. 4-6 g. A distinct yielding point at engineering stress of ~900MPa and strain of ~5% was observed, and this sample experienced a total 12.4% strain before final fracture. The engineering fracture strength was subsequently determined to be ~774MPa. Due to the relatively low magnification (needed for video calibration) and low video recording speed (0.5 frame per second) used in this in situ experiments, we were not able to capture the instantaneous diameter just before the final facture. Nonetheless, by measuring the diameter at the necking section (i.e., ~3.5nm) using the last frame prior to fracture, we obtained a nominal true breaking stress of ~3.55GPa (considering the actual instantaneous diameter should be less than 3.5nm, the actual true fracture strength may even be higher).

Interestingly, this "typical" elastoplastic ductile facture was not always observed in our systematic investigations. In Figure 4-7, another tensile test with distinctively different fracture behavior, i.e., brittle-like fracture was observed. The sample experienced comparatively much shorter elongation and suddenly fractured, leaving a relatively flat fracture surface (Fig. 2b).For this particular sample, the diameter was also ~7.5nm and the initial length was ~60.5nm. At the beginning stage of the tensile test, the load was applied along the nanowire axis with a misalignment angle of ~25 degrees, due to the changes in sample position and orientation during clamping process. Corresponding stress-strain curves in Fig. 2c showed that engineering stress of the

sample continuously increased up to ~1GPa before final fracture at ~5% strain. No apparent yielding and plastic deformation/necking was observed.

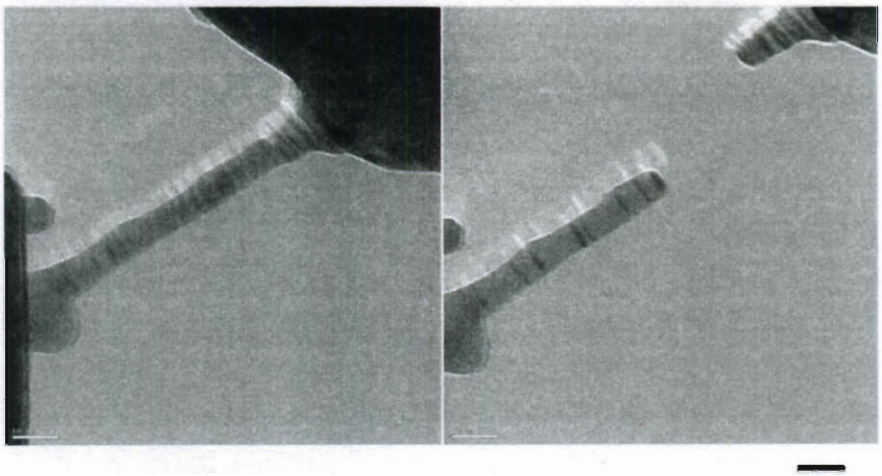

(a) (b)

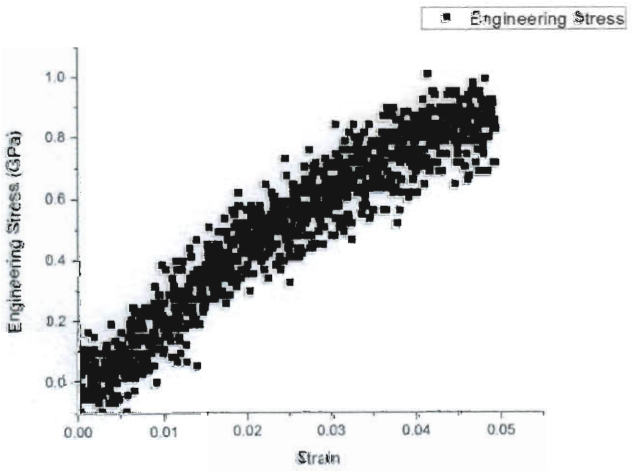

(c)

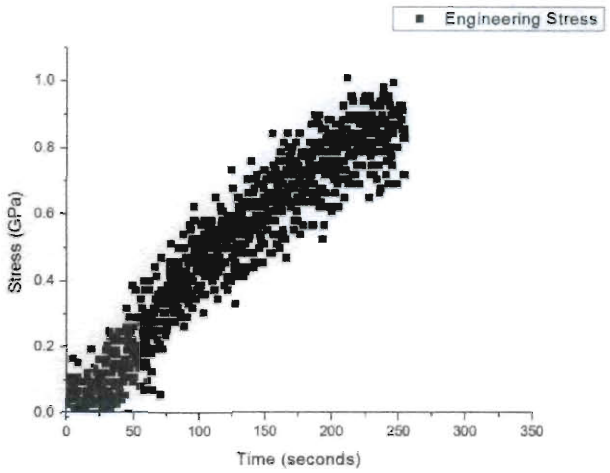

(d)

Figure 4-7 A typical brittle fracture of a long nanowire under tension with a low loading rate (~0.1nm/s): (a) initial state; (b) after breaking (scale bar 10nm); (c) corresponding engineering stress-strain curve; (d) engineering stress as a function of loading time.

By carefully examining the fracture morphologies, stress-strain curves and deformation processes from the videos of all 22 in situ quantitative tensile experiments performed on sub-20 nm Au nanowires, we were able to distinguish the "ductile" versus "brittle" fracture modes using the three criteria defined in Table 4-2 and divide all the tests into two categories as summarized in Table 4-1.

Table 4-1 Summary of the 22 successful tensile tests on ultrathin gold nanowires

Sample	Diameter (nm)	Engineering Strength (GPa)	True Strength (GPa)	Fracture Strain
Ductile				
1	8.5	0.598	6.913	0.145
2	7.5	0.774	3.554	0.124
3	9.9	0.822	5.497	0.161
4	7.4	0.889	5.409	0.110
5	9.7	0.654	9.819	0.196
6	5.5	0.813	9.607	0.142
7	10.5	0.960	4.150	0.111
8	10.0	0.620	6.055	0.264
Average	8.6	0.766	6.375	0.156
Brittle				
1	14.0	0.641	1.038	0.033
2	10.0	0.892	1.586	0.059
3	7.2	1.008	2.534	0.068
4	9.3	1.860	2.644	0.037
5	7.1	0.875	1.437	0.033
6	9.1	0.625	0.885	0.065
7	10.0	0.827	1.768	0.063
8	10.0	0.552	1.190	0.057
9	7.5	1.550	2.181	0.084
10	8.5	0.601	0.890	0.071
11	6.4	0.939	1.087	0.061
12	10.1	1.034	1.274	0.073
13	7.5	1.000	1.563	0.050
14	10.0	0.600	1.667	0.074
Average	9.0	0.929	1.553	0.059

It might be noted that, while in general the ductility (breaking strain) was used as the primary criterion, fracture surface morphology and deformation process observed from the videos were oftentimes more straightforward in determining the fracture modes

without the need of labor-intensive data processing and extraction. However, due to re-arrangements of surface atoms, the fracture morphology may change as a function of time, resulting in hard-to-distinguish features under lower TEM imaging magnifications (typical magnifications for most of in situ experiments performed). This could make the last two criteria less reliable. Finally from Table 4-1, the brittle fracture samples had slightly higher engineering fracture strength than the ductile fracture samples on average, while samples failed in ductile mode had much higher true fracture strength than the ones failed in brittle mode, due to the significant cross-section area reductions during the necking process.

Table 4-2 Criteria for defining "brittle" and "ductile" fracture

Fracture Modes	**Brittle**	**Ductile**
Ductility (breaking strain)	**<8.5% (AVG 5.9%)**	**>11.0% (AVG 15.6%)**
Fracture surface morphology	"Cleavage" (flat fracture surface perpendicular to the nanowire axis)	"necking down to a point" (extreme case: atom chain)
Deformation process	limited plastic deformation, sudden fracture	stable necking developments, sustained elongation until final fracture

Gold was considered as one of most ductile metals and very rarely has brittle fracture for gold samples at room temperature been reported, even at the nanoscale. One may suggest that higher loading rate could potentially cause this brittle fracture for the ultrathin gold nanowire. However, in all 22 successful tensile tests with nanowire diameters ranging from 5-15nm, 14 of them were fractured in "brittle" mode (see Table

4-1) and they occurred under various loading rates ranging from 0.1-0.5nm/s. Loading rates of the same range were applied in the ductile fracture cases. In particular, the specific test shown in Fig. 4-7 was performed at an extremely slow rate of 0.1nm/s, with the total duration of the experiment reached 250 seconds (Fig. 4-7 d), which is slower than most of the ductile fracture cases. Therefore, the loading rate appears not to be the dominating factor in determining the fracture modes.

Compared to the recently established surface partial dislocation mediated plastic deformation induced ductile fracture [3, 4, as well as Chapter 4.1] of nanoscale metals, the unusual brittle fracture behavior observed is particularly intriguing as these dimensionally similar nanowire samples were originally all single crystals with the same orientation, and were tested under similar loading rates at room temperature. In order to reveal the underlying mechanism behind this "brittle" fracture, HRTEM analysis was performed for a sample failed in brittle mode, with the highly magnified image focusing on the broken section. Interestingly, we discovered that there were multiple twin boundaries near the fracture zone (Fig. 4-8). The twin boundaries were perpendicular to the nanowire axis, and the fracture of nanowire samples appeared to always occur along or near one of the twin boundaries (Fig. 4-8 a-f). Fast Fourier Transformation (FFT) calculation of the sample after fracture (Fig. 4-8 g) also confirmed the existence of twin structures in the fractured nanowire. The same link between the observed twin structures on {111} planes of the nanowire samples and the brittle fracture mode was confirmed for all 14 samples (Table 4-1) via high resolution imaging. Moreover, no such twin structures were observed for any of the nanowire samples fractured in ductile mode. This strongly

suggested that the twin structure might play a critical role in brittle facture of the nanowire.

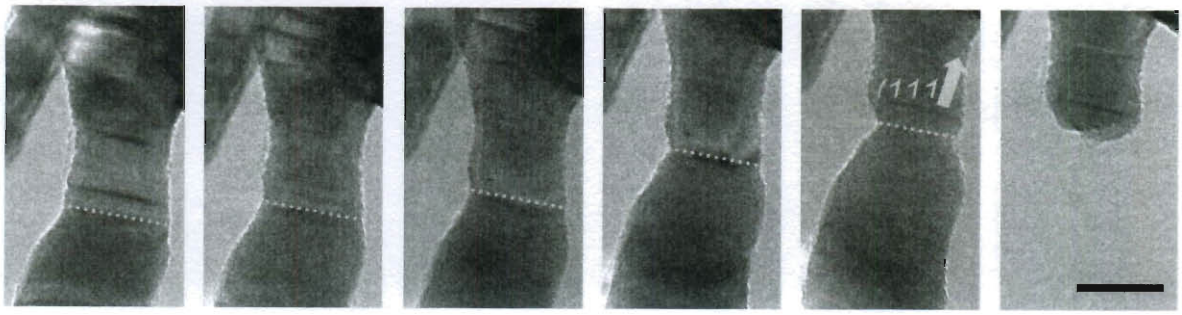

(a-f)

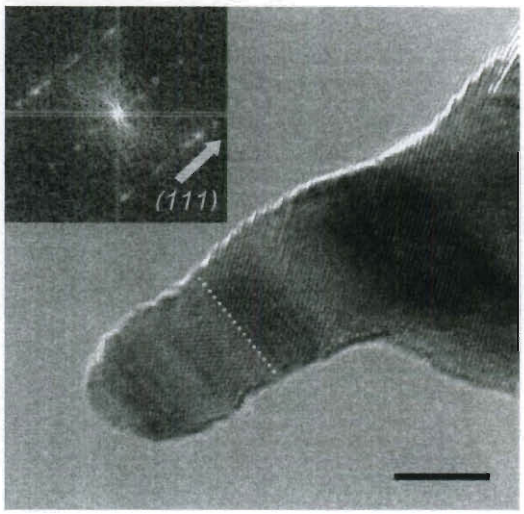

(g)

Figure 4-8 HRTEM tensile test of a short nanowire with twins: (a) initial state with three twin boundaries; (b) surface non-uniformity near the bottom twin (marked by white dotted line) under tension; (c-d) further loading cause stress concentration at the intersection between bottom twin boundary and free surface; (e) right before fracture, a groove was formed near the marked twin boundary; (f) after fracture along the bottom twin boundary, the top two twin boundaries remained inside the nanowire; (g) a nanowire

fractured in brittle mode, corresponding FFT insert clearly shows the remaining twin structures (all scale bar 5nm).

Molecular dynamics (MD) simulations were performed to further assess the role of twinning on subsequent fracture modes. Two different cylindrical Au virtual nanowire samples, one with perfect face centered cubic (f.c.c.) structure and another with a sharp interface bounded by f.c.c and hexagonal close packed (h.c.p.) structures at the center simulating the observed twin boundaries, were examined under uni-axial tension between two substrates. The atomistic cross-sectional views of the initial nanowire geometry and final fracture morphology of both samples were shown in Fig. 4-9.

Nanowire samples are initially of the same crystalline orientation (except for the twinned region shown in Fig. 4-9 c), as well as of the same vertical and radial dimensions (i.e., L = 4.2 nm and D = 3.5 nm) in cylindrical shape with each being separately sandwiched between two substrates. A circular notch was created initially in the nanowire either at the middle position or at the twin boundary (Fig. 4-9 a and c), to resemble the surface non-uniformity observed in experiments (Fig.4-8). This notch also served as the position for initial deformation to occur. In Fig. 4-9 c atoms in twinned region were coloured in red with other atoms coloured in orange, while in Fig. 4-10 e-f atoms were coloured via the local order parameter proposed by Steinhardt et al. [153].

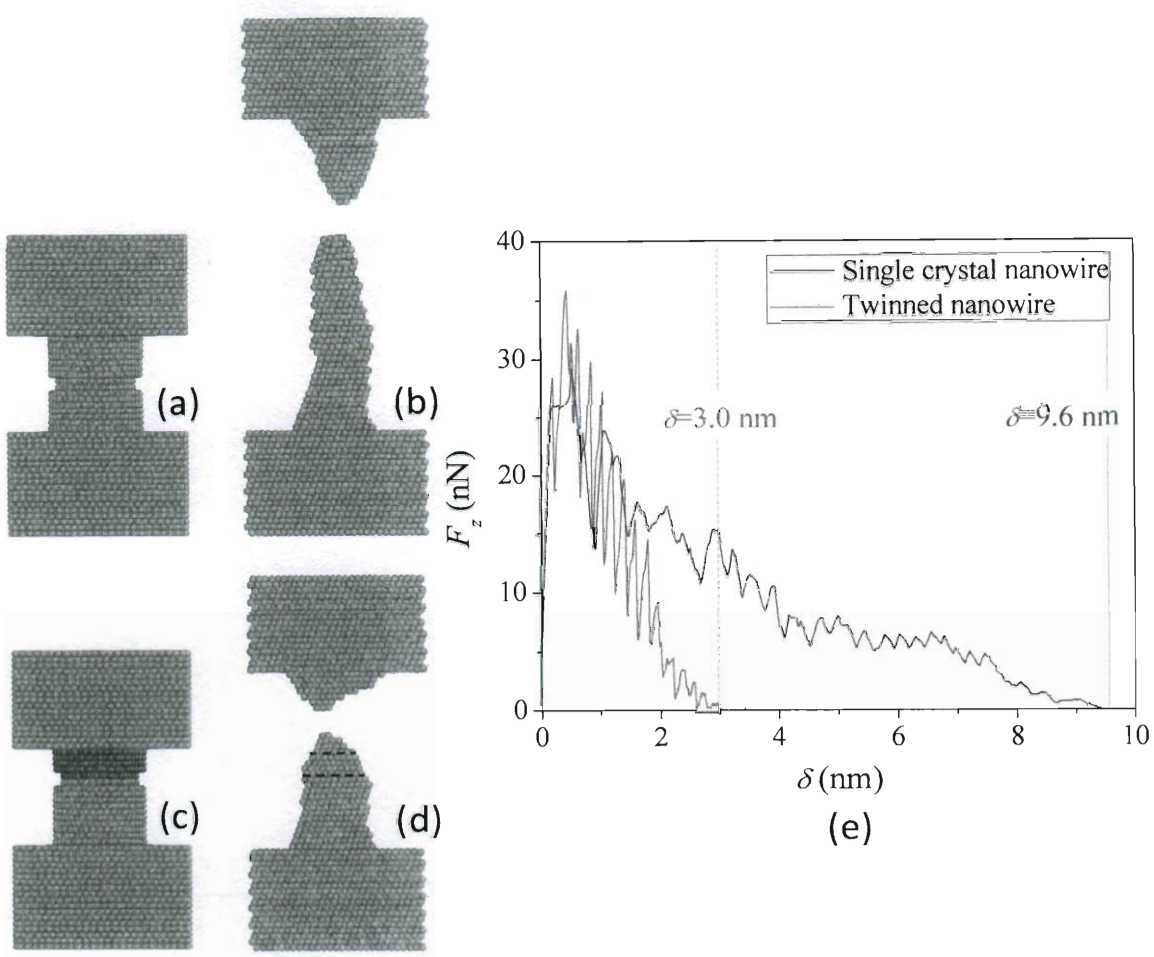

Figure 4-9 MD simulation of nanowires of comparable dimensions with and without twins in the middle: projection view of a pristine single crystal nanowire without twin before loading (a) and after fracture (b); projection view of a nanowire with a twin boundary in the middle (with atoms in the initial twinned region coloured in red), before loading (c) and after fracture (d); the atomic configurations in (b) and (d) were rotated in order to clearly reveal the remaining twin structures as indicated by black dash lines; (e) force versus displacement / elongation curves for both tests.

The simulations were performed in a NVT ensemble with the temperature maintained at 300 K using a Nosé–Hoover thermostat [154]. During the simulations, the top and bottom substrates were brought apart at a constant speed of v_z = 0.2m/s, stretching the nanowire clamped in between until final fracture. The inter-atomic potential employed in the present study to describe the interactions between atoms is the embedded-atom method (EAM) [155-156] potential for Au developed by Cai and Ye [157].

In Figure 4-9 a & b, the single crystalline f.c.c. nanowire deformed and fractured in a ductile manner with significant elongation and thinning, and sustained large strain. On the other hand, the nanowire with a twin boundary at the center would break near the twin boundary, at a much smaller strain with almost no thinning process (Fig. 4-9 c & d). Careful examination of the structural changes during tension and final fracture morphologies of these two samples revealed that the single crystalline nanowire formed two sharp long tips following the substantial necking development, with no twin boundaries could be observed during tension and after failure. On the other hand, the initially twinned nanowire formed a relatively flat fracture surface, with a couple more twin boundaries appeared in the fractured sample (Fig. 4-9 d) similar to what has been experimentally observed in Fig. 4-8 g. The facture seemed to have initiated from the intersection of the initial twin boundary with the nanowire surface, where surface atom arrangements had been disturbed by the intersection of twin boundary (Fig. 4-8 and 4-10 b) In Fig. 4-9 e, applied force along nanowire axis direction (F_z) versus elongation (δ) of the nanowires before fracture were plotted, clearly demonstrating the nanowire with initial twin structure had much less ductility than that of single crystalline nanowire

(about 3-4 times differences, correlating well the experimental results summarized in Table 4-1). Therefore, the effects of twining on determination of Au nanowire ductility and fracture modes had been verified.

4.2.4. Discussions

Considering the fact that all samples initially have the same single crystalline <111> structure, it is certainly of interest to examine how these twin structures formed in pristine nanowires. It should be noted that twins can easily form in gold nanowires under various loading conditions as gold has relatively low stacking fault energy [158]. It is possible that those twins may occasionally form during manipulation and sample clamping process. More importantly, we experimentally confirmed that twins could form during tensile loading from the initial single crystalline structure, as shown in Fig. 4-10 a-b. Similar type of twin formation in gold nanorod during tensile loading had been also observed experimentally [159] and in computational simulation [160-162]. It is shown that the formation of twins is associated with the stack fault (SF) generation [149], as well as the collective motion of Shockley partial <112>/6 along {111} slip planes that can transform the structure from FCC to HCP [160, 162].

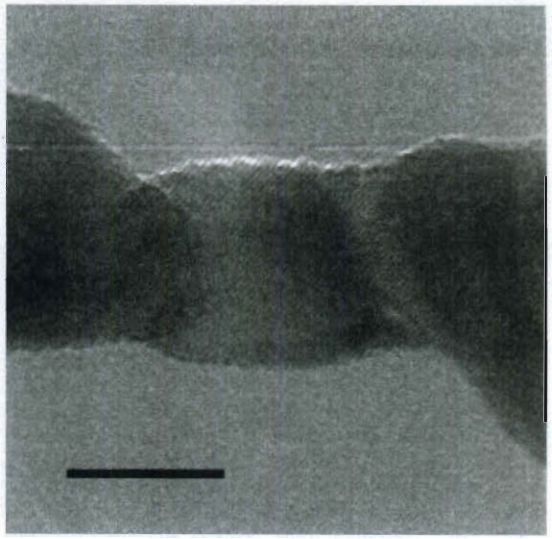

(a)

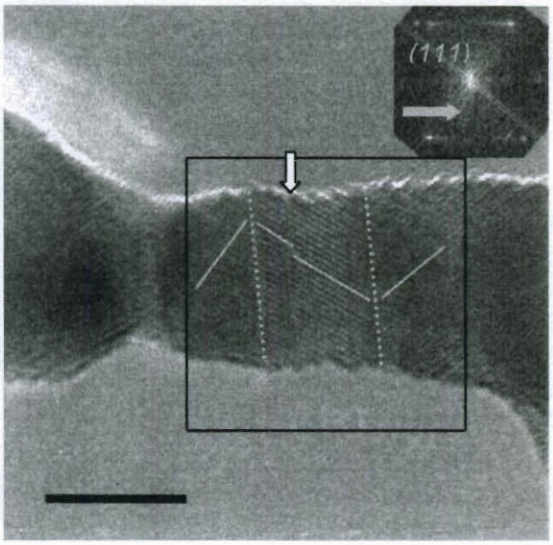

(b)

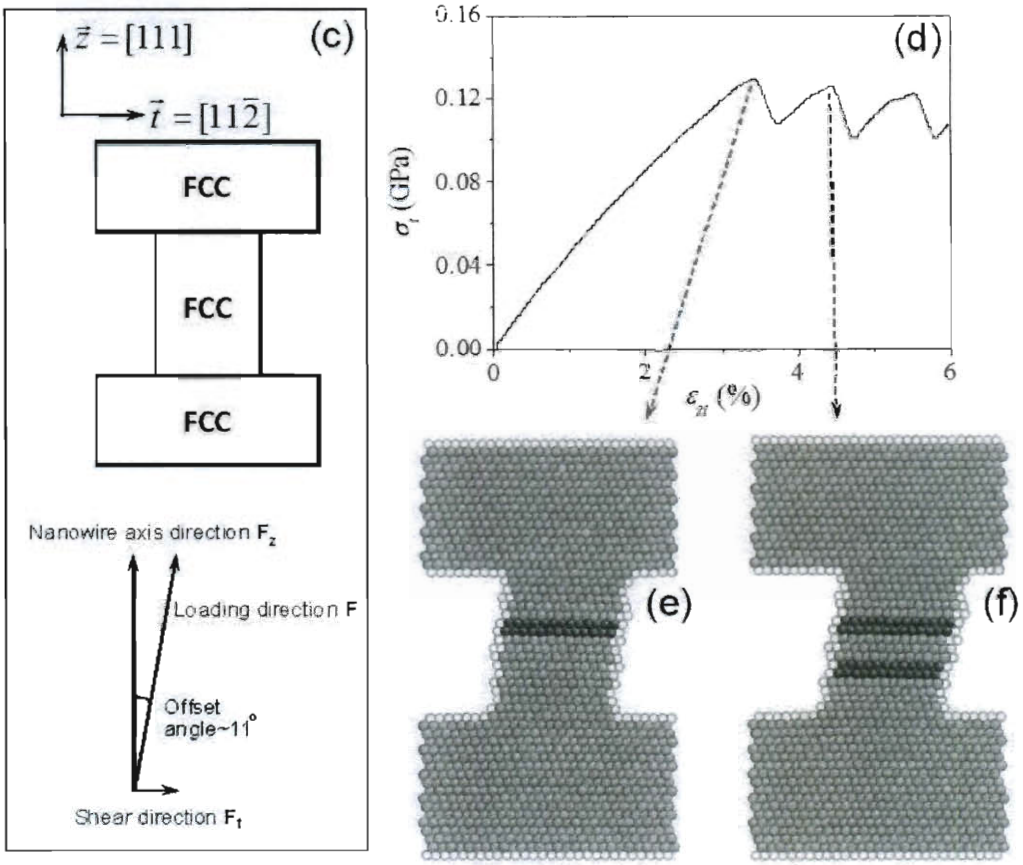

Figure 4-10 Experimental and computational confirmation of twin formation during tensile loading: a short single crystal nanowire under in situ HRTEM tensile loading, before loading (a) and after a certain amount deformation with twin formed (b); In (b), two twin boundaries and a stacking fault (SF) were clearly observed, the inserted FFT confirmed the observed twins were along (111) planes (scale bar 5nm); (c) the configuration of shear induced twin formation in MD simulation; (d) shear stress σ_t versus strain ε_{zt} plot with corresponding twin formation events (e and f). In e and f, atoms were coloured in yellow representing normal FCC arrangements, coloured in blue representing HCP arrangements and coloured in white representing surface atoms.

In Fig. 4-10 as well as in Fig. 4-8, twin boundaries were observed to be perpendicular to the nanowire and loading axis. It is thus a quite logical next step to evaluate the possibility of having a driving force perpendicular to the intended loading direction (along nanowire axial direction) that could result in the formation of the observed twin structures. In all cases where twin formation (e.g., see Figs. 4-7, 4-8, 4-10 and Ref. [159]) had occurred, some initial misalignments between nanowire axis and loading directions were always observed. As such misalignment inevitably induced shearing along the transverse planes, it might provide the necessary driving force to promote the nucleation of SF and subsequently the formation of twins.

To validate this possible origin of twin formation due to misalignment induced shearing, we again performed MD simulations. An originally pristine single crystal nanowire oriented along <111> direction was placed under a tensile loading force $\vec{F}$. The loading direction is ~11 degree off the wire axis (Fig. 4-10 c), introducing a shear component F_t. The corresponding shear stress-strain ($\sigma_t - \varepsilon_t$) curve was shown in Fig. 4-10 d. We observed that once σ_t exceeded a critical value ~0.13 GPa (well comparable to experiment data taking into consideration of misalignment angle), twinning partial dislocations were nucleated (see Fig. 4-10 e-f) and corresponding load drops were observed (see Fig. 4-10d). It is worth noting that the shear loading component F_t is fairly small compared to the primary tensile loading force, in accordance with small misalignment angles in reality. It is for this reason that no significant load drops were observed in the tensile stress-strain curves of nanowires fractured in brittle modes.

Additionally, considering the fact that misalignments may be unavoidable during the initial stage of tensile tests due to the difficulties associated with sample manipulation

and clamping, it is very important to evaluate the magnitude of misalignment that could lead to the observed twin formation and subsequent brittle fracture rather than the more classical partial dislocation nucleation and propagation mediated ductile fracture. In fact, the initial stage of both conditions was activated by one partial/stacking fault, so we only need to consider those slip systems that result in intrinsic stacking faults. From the Thompson Tetrahedrons [163], we can identify the possible operating slip systems during tensile deformation of the nanowire as following:

1. Twinning partial: $(111)[\bar{1}\,\bar{1}2]$

2. Non-twinning partials: $(11\bar{1})[\bar{1}\,\bar{1}2]$, $(\bar{1}11)[\bar{2}\,\bar{1}\,\bar{1}]$ and $(1\,\bar{1}1)[\bar{1}2\,\bar{1}]$

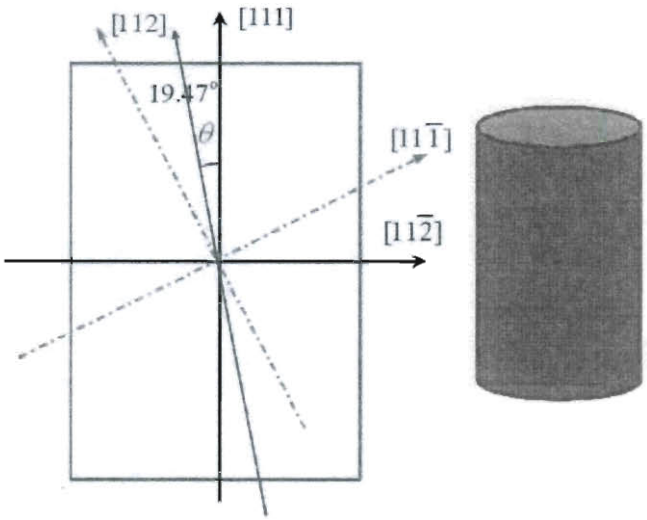

Figure 4-11 Schematic illustration of loading misalignment with corresponding multiple slip systems for twining partial and normal partial dislocation initiation: the bold black (red) line with single-head arrow stands for the loading direction with a misalignment angle theta; and the dotted grey (blue) lines with single-head arrow indicate two possible partial dislocation slip systems.

Note in Fig. 4-11, only slip systems $(111)[\bar{1}\,\bar{1}2]$ and $(11\bar{1})[\bar{1}\,\bar{1}2]$ were shown as they are most relevant if a shear component is induced along $[11\bar{2}]$ direction due to misalignment. By assuming actual loading stress σ and misalignment angle θ, we can calculate the corresponding resolved shear stress on slip systems $(111)[\bar{1}\,\bar{1}2]$ and $(11\bar{1})[\bar{1}\,\bar{1}2]$, denoted as τ_T and τ_p, respectively.

$\tau_T=\sigma\sin\theta\cos\theta$

$\tau_p=\sigma\sin(19.47-\theta)\cos(19.47-\theta)$ —— 19.47 is the angle between [111] and [112] directions

So the criteria of the (111) twin formation prior to the $(11\bar{1})[\bar{1}\,\bar{1}2]$ partial dislocation slip will be:

$\tau_T > \tau_p \rightarrow \sigma\sin\theta\cos\theta > \sigma\sin(19.47-\theta)\cos(19.47-\theta) \rightarrow 4\theta > 38.94 \rightarrow \theta > 9.74$ degree

From this calculation, it is clear that when initial misalignment angle θ is small (less than 9.74 degree), the shear component τ_T for twinning partial is small while the shear component for $(11\bar{1})[\bar{1}\,\bar{1}2]$ non-twinning partial is much larger, resulting in the non-twinning partial dislocation nucleation/propagation mediated ductile fracture. However, if the θ is larger than 9.74 degree, the shear component τ_T for twinning partial will be larger than the shear component for non-twinning partial, resulting in the twin formation and subsequent brittle fracture. Therefore, this simple criterion based on competition between twin formation and partial dislocation nucleation/propagation as a

function of misalignment angle could be used to explain experimentally observed brittle and ductile fracture in sub-20 nm gold nanowires.

Finally, it is worth noting that due to the high aspect ratio of the nanowire samples tested (thus quite compliant in the transverse direction) and the nature of the TEM loading stage configuration, tensile loading generally tends to become self-aligned in later stage of the tests. Thus even after the initial formation of twins, partial dislocations might still be generated later. Systematically understanding of how twins interact with later formed partial dislocations and how such interactions affect subsequent fracture mode would definitely be an interesting future work to be explored. In one of the preliminary study shown in Fig.4-12, we observed that partial dislocations had been activated in later stage of tensile testing. It indeed could be blocked by the twin boundaries, which prevents the dislocation propagation as well as the subsequent necking process, resulted in the similar brittle fracture. These may also explain the slightly higher engineering tensile strength for nanowires failed in brittle mode, which possibly confirmed twin strengthening effect in nanowires [158] experimentally.

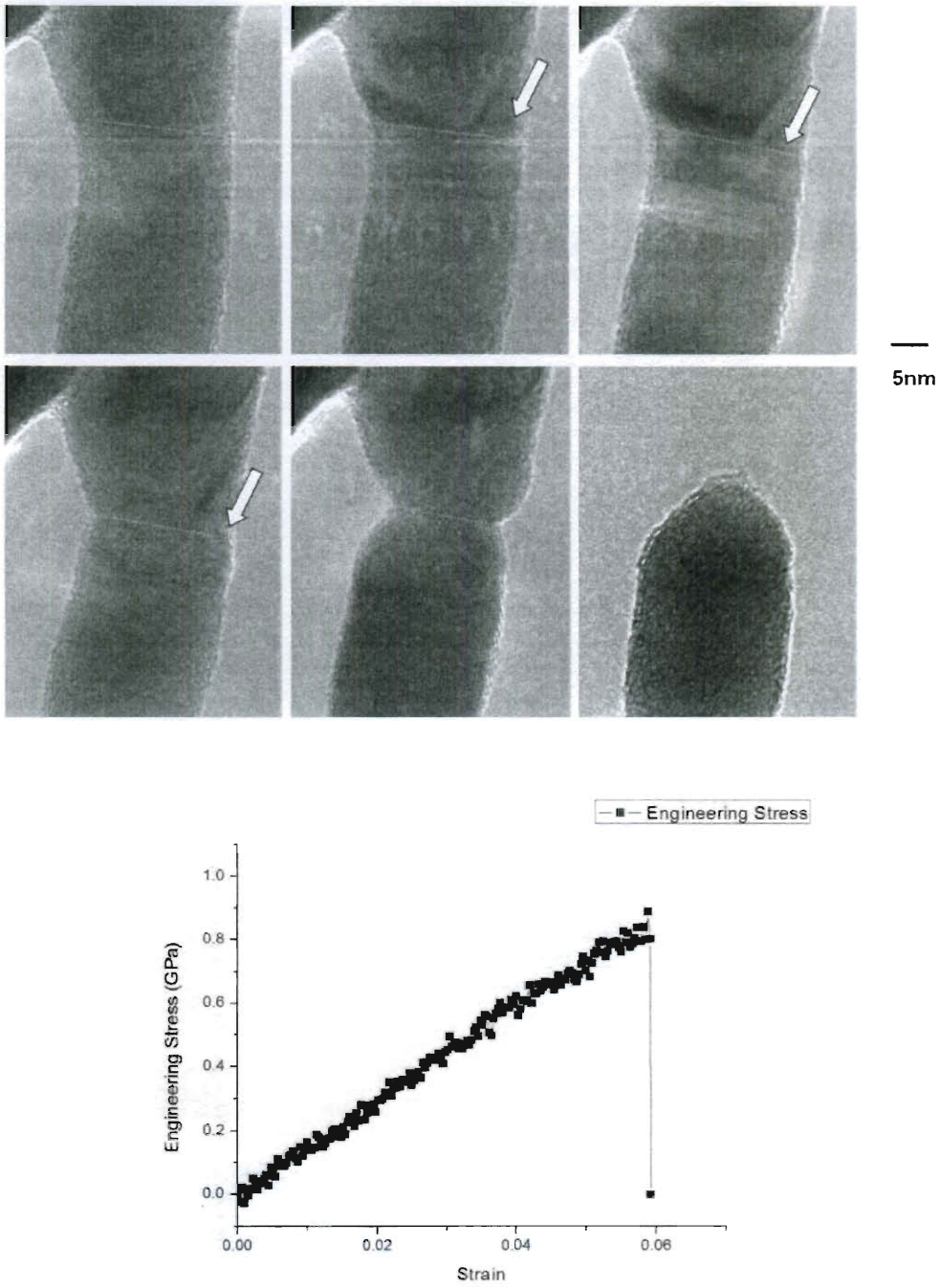

Figure 4-12 Dislocation blocked by the twin boundary, resulted in the typical brittle fracture near the twin boundary

4.2.5. Conclusions

In summary, we have systematically studied the mechanical behavior of sub-20 nm gold nanowires under tension loading. For nanowires of virtually the same pristine single crystal structure and dimensions, distinct fracture behaviors were observed including both the expected ductile fracture and the unusual brittle fracture with low ductility. In the samples that experienced brittle fracture, (111) twin structures were found to form during initial loading stage due to small misalignment and the final failure usually occurs along one of the twin boundaries. This study provided a comprehensive picture of deformation and fracture mechanisms of ultrathin metallic nanowires. Our results can potentially offer significant insights towards the reliability of future nanoelectronic and nanoelectromechanical devices consists of these fascinating nanoscale building blocks.

Chapter 5

Cold Welding of Ultrathin Gold Nanowires

5.1. Introduction

Welding, with its historic development tracing back to the Bronze Age, serves modern industry in broad areas where metals are used [164]. While back to 1940s people started to recognize "cold-welding" as a general phenomenon, it had already been practiced for more than 700 years [165, 166]. Unlike normal welding where liquids or molten phases need to be present, cold-welding is a solid-state welding process in which joining takes place without fusion (the process of causing a material to melt with intense heat) at the interface. However, in order to realize the cold-welding for bulk metals, either high applied normal/frictional load or atomically clean flat ductile surface in ultrahigh vacuum environment is generally required. About two decades ago, G.M. Whitesides and his colleagues discovered that metallic thin film, such as gold, supported on compliant elastomers can weld together at remarkably low loads under ambient laboratory conditions [166]. While its underlying mechanism has not been fully understood, this finding extended cold-welding process into a broad range of modern organic microelectronic/optoelectronic devices fabrication, such as organic light emitting devices (OLED) and photovoltaic cells [167]. Now as extensive researches going on for nano-electronic devices and NEMS, whether or not cold-welding could also be practiced at the nanoscale becomes an interesting topic. In recent years, scientists successfully

realized the joining of individual low-dimensional nanostructures, such as carbon nanotubes [110, 168-170] and metal/semiconductor-filled carbon nanotubes [171-174], metal/semiconductor/ceramic nanowires and nanoparticles [175-183], by either applying voltage/current or heating the sample stage or focusing high intensity electron or laser beams on the joining section. While these methods certainly have their own advantages, however, aforementioned nanoscale welding techniques have always involved some sorts of local heating processes which could be difficult to control precisely at relevant length scales and may change the underlying substructures and related properties of the original building blocks. Due to these limitations, the idea of cold-welding, which joins nanostructures without heating, becomes an attractive solution for bottom-up assembly at the nanoscale.

5.2. Nanoscale cold-welding

In this work, cold-welding of individual gold nanowires was performed and monitored inside a high resolution transmission electron microscope (HRTEM) equipped with Nanofactory^{TM} TEM-scanning tunneling microscopy (STM) and TEM-atomic force microscopy (AFM) sample holders. Ultrathin gold nanowires (diameter less than 10nm) were chosen because they are widely considered as an ideal candidate to achieve extremely dense logic and memory circuits as future molecular-scale interconnects [38, 41]. The good resistance to oxidization for gold is another reason. Samples were selected from two sources. The first type is the ultrathin gold nanowires with relatively small aspect ratio, i.e. with ~5-10nm in diameter and 10-50nm in length, referred as "nanorods" in this paper. They were originally ligaments that were cut off *in situ* from home-made

porous gold nanostructures (Fig. 5-1 a). The porous gold nanostructures were obtained via dealloying process of gold-silver alloy [119, 121]. The second type of sample is recently developed micron-long ultrathin gold nanowires [41] with 3-9nm in diameters (Fig. 5-1 b). HRTEM imaging and selected area diffraction (SAD) showed that both samples had single crystalline face-centered cubic (FCC) structure. The average inter-fringe distances for both types of sample were measured to be around 0.23-0.24nm, corresponding to (111) lattice spacing (0.23 nm) of the FCC gold crystal.

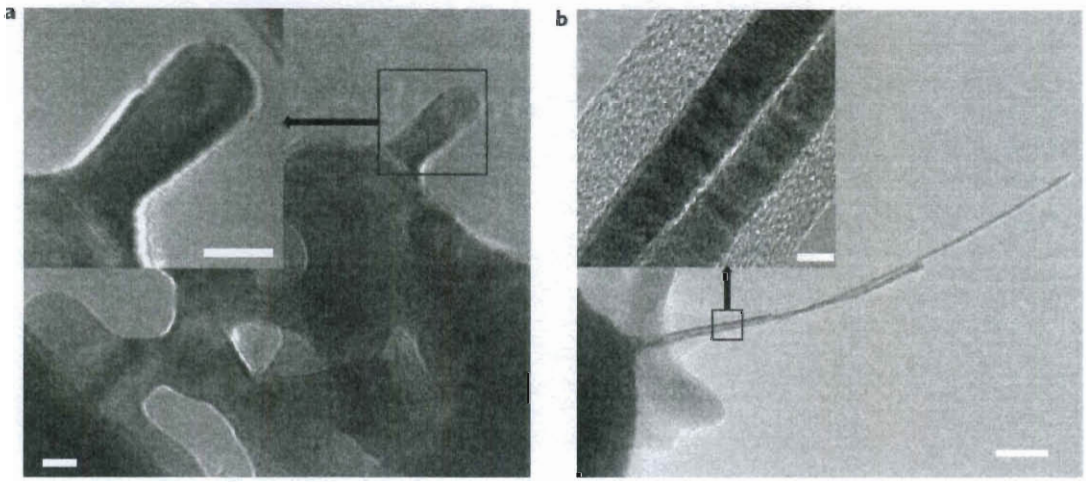

Figure 5-1 Two types of ultrathin gold nanowire samples. TEM images of (a) an ultrathin gold nanorod (scale bar 5nm) on porous gold nanostructures and (b) micron-long ultrathin gold nanowires (scale bar 100nm), with corresponding HRTEM image inserts showing the crystalline structures (chemically-fabricated micron-long nanowires were usually covered with a layer of surfactant (oleylamine), and mechanical rubbing between two nanowires can effectively remove the residual surfactant on their surfaces before welding experiments) (scale bar 5nm in both inserts)

The *in situ* TEM samples were prepared by adhering nanowires or nanorods onto tungsten or gold STM probes and then loaded to the TEM-STM or TEM-AFM holders (NanoFactory^{TM} Instruments, Sweden). Three-dimensional movement of STM probes was driven by a piezo-electric head of the holders. In addition to normal manipulation and joining of nanowires, the TEM-STM holder can also apply a specific bias and measure the current response of the nanowire sample bridged across two gold STM probes. All welding experiments were carried out using an FEI^{TM} Tecnai G^2 F30 TEM, mostly operating at 300KV working voltage (lower working voltages were also used in order to rule out the electron beam heating effect). During all welding experiments, no current was passed through the sample and a low intensity electron beam was always used for imaging and video capturing.

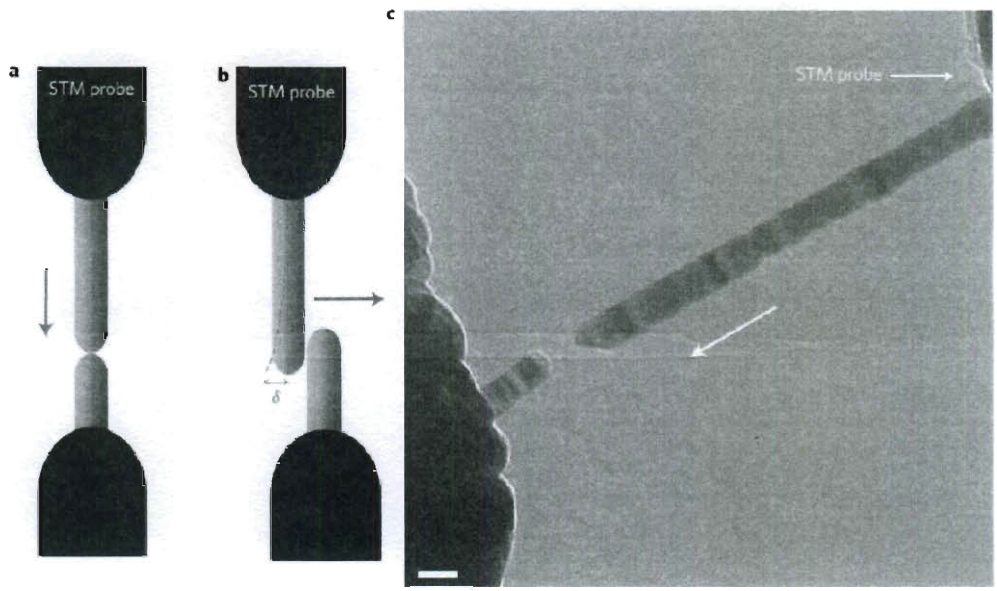

Figure 5-2 Nanowire manipulation and welding geometries. Schematic images of two welding geometries for ultrathin gold nanowires: (a) Head-to-head; (b) Side-to-side mode (δ represents virtual bending deflection of the top nanowire when contacting to the

bottom nanowire); (c) A TEM image showing the manipulating movement of a longer nanowire toward a short nanowire (Scale bar 10nm)

Both "head-to-head" and "side-to-side" joining were performed in our experiments for both types of samples using the TEM-STM holder, as illustrated in Fig. 5-2 a-b, respectively. Other welding geometries can be also realized, such as a case of "head-to-side" joining shown in Supplementary Information. Individual nanowire was manipulated through a tungsten or gold STM probe (Fig. 5-2c), driven by a movable piezo-electric head of the holder. Joining of two gold nanorods was attempted first in the head-to-head way, as shown in Fig. 5-3. We manipulated one nanorod toward another by continuously adjusting the position alignment until the two samples approaching each other head to head (Fig. 5-3 a-b). When the front surfaces of the two nanorods contacted, they welded together instantly (about 1.5 second, Fig. 5-3 c-d). After the welding, the image contrast of the welded nanorod became more and more uniform (Fig. 5-3 d-f), indicating continuous substructure evolutions (Fig. 5-3 d-e) to smooth the surface. Once this process completed, the STM probe was then pulled back (Fig. 5-3 f-h) along the direction indicated by the arrow, until fully separated from the sample. It was shown that the as-welded nanorod still maintained its morphology and structure in the free-standing state (Fig. 5-3 i). Similar joining was also successfully made for micron-long ultrathin gold nanowires; however, head-to-head welding for gold nanorods was much easier to be performed since they had no buckling issue as in the case of manipulating longer nanowires.

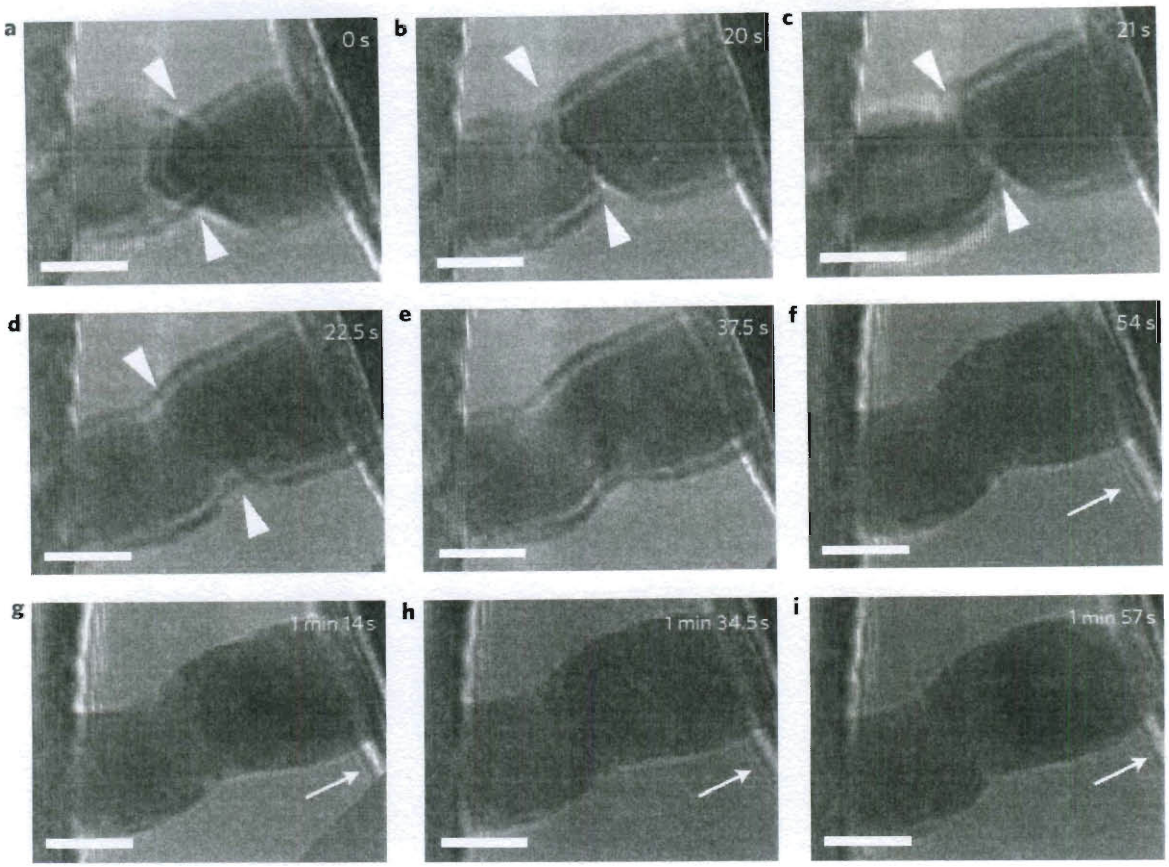

Figure 5-3 Head-to-head welding of two gold nanorods. One nanorod (right) was driven to approach another (left) until their front surfaces contacted (a-c); Welding process was then completed within ~1.5 seconds (c-d) followed with structure relaxation (d-e); After withdrawing the STM probe (f-i), the as-welded nanowire was in the free-standing state in the last image (i). Triangles indicate the front edges of two nanorods; Arrows indicates the withdrawing direction of the STM probe (Scale bar 5nm)

For the side-to-side welding, precise alignment is not required and successful joining of both types of samples was easily repeated for many times. Simply manipulating the nanowires until they partially overlapped to each other, a side-by-side contact could then be made and cold-welding would always occur promptly (Fig. 5-4 a-

b). The particular welding process finished within 34 seconds (Fig. 5-4 b-c), and HRTEM imaging in Fig. 5-4 d shows the structure of the as-welded structure after relaxation process. In order to check the welding quality, *in situ* pulling of the as-welded nanowire (Fig. 5-4 e-j) was performed right after the first joining. Surprisingly, the welded nanowire formed a neck and broke at another location rather than at the joining section from the first welding. Comparison of the lengths of the nanowire which remained stationary at the bottom during the pulling process (original ~21.5nm in Fig. 5-4 a and after-breaking ~25.7nm in Fig. 5-4 j) clearly demonstrated that the as-welded nanowire broke at a different location which was about 4.2nm above the original welding spot. The qualitative pulling result implies that the as-welded structure is as strong as the original nanowire.

With the same sample shown in Fig. 5-4 a-j, we also performed a second welding via a head-to-head mode, and then pulled the as-welded nanowire again until breaking. During this pulling process, the sample formed a neck near the second welding zone (Fig. 5-4 k). Fast Fourier Transformations (FFT) from images taken from both the welded segment and the remaining segment of the nanowire (which also contained the first welding zone) confirmed that the second welding zone and the rest part of the nanowire (Fig. 5-4 l) were both single crystalline in the same <111> orientation.

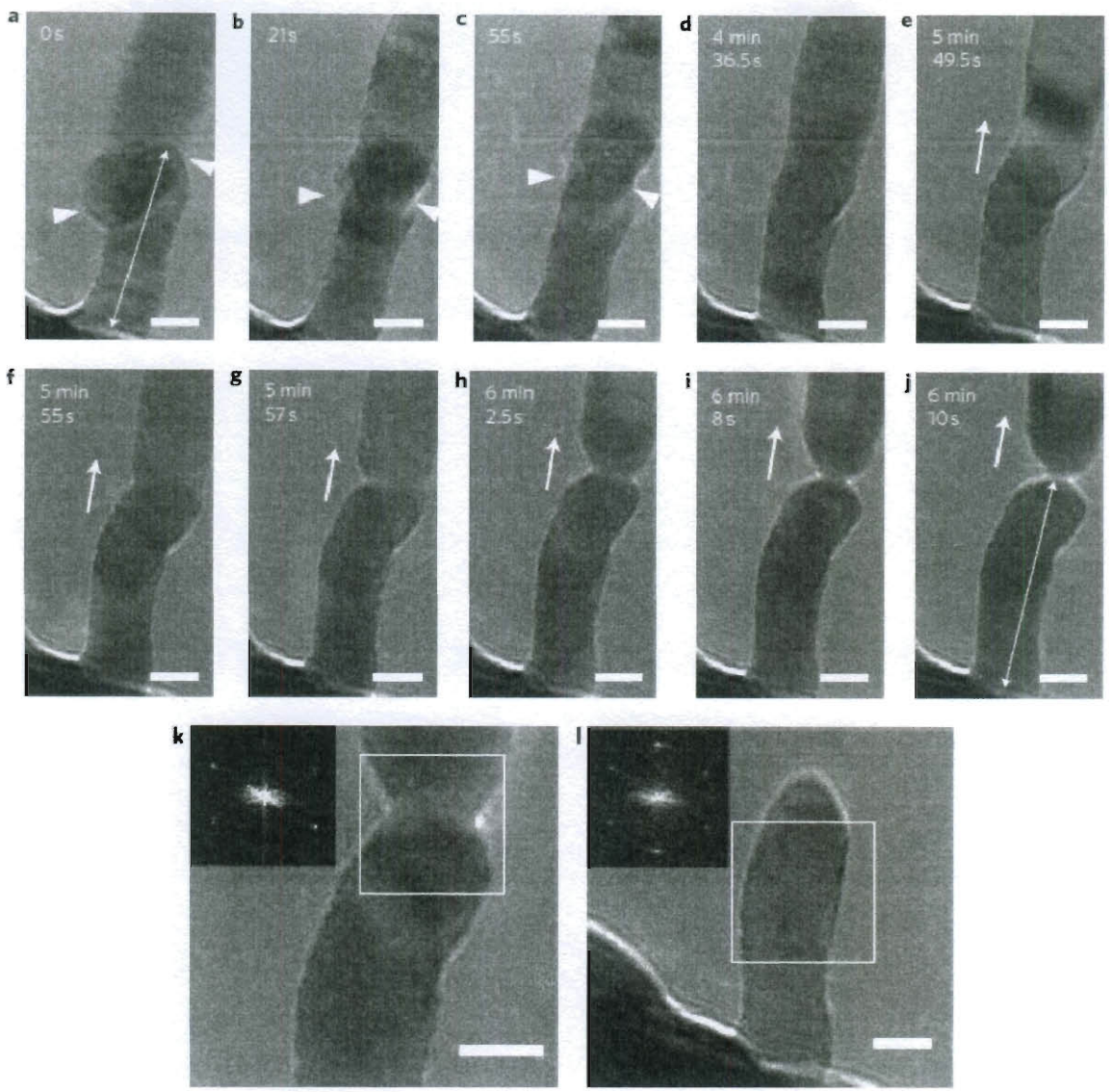

Figure 5-4 Side-to-side welding of two gold nanowires. Welding of two ultrathin gold nanowires was completed within ~34 seconds by making side-to-side contacts (a-c), followed with structure relaxation (c-d) and *in situ* pulling of the as-welded nanowire (e-j); The thin double-headed arrows in (a) and (j) indicate the bottom nanowire length before and after the first welding and pulling; Then the two broken nanowires in (j) was welded again by making a second contact, followed with a second pulling and breaking. Images k and l show HRTEM images of the necking area during the second pulling and

the remaining nanowire at the bottom after second breaking, respectively; Inserts show calculated diffraction patterns from the square regions of both images by Fast Fourier Transformation (FFT); Again, triangles show two edges of two nanowires before welding while the thicker single-headed arrows indicate the STM probe pulling direction. (Scale bar 5nm)

In addition to aforementioned "head-to-head" and "side-to-side" joining geometries, cold-welding can also be realized in other geometries depending on (a) the relative positions of two nanowires; (b) the degree-of-freedom of nano-manipulation; (c) the matching orientation of two nanowires. For example, a "head-to-side" welding was successfully performed and form a "T" shape nanowire junction (Fig. 5-5 a-c). Combining multiple welding geometries, more complex configuration of nanowires can be bottom-up assembled, such as illustrated in Fig. 5-5 d.

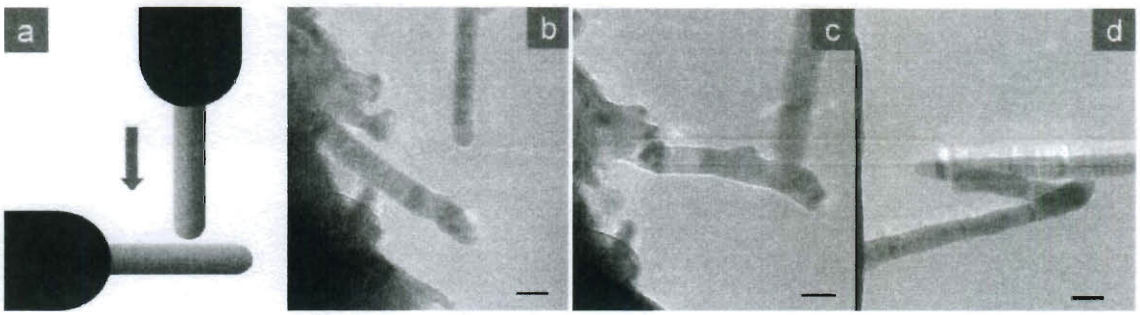

Figure 5-5 Head-to-side welding for two ultrathin gold nanowires (a) An illustration of welding geometry; (b) Before welding and (c) After cold-welding; (d) The joining of multiple (three) nanowires by cold-welding (Scale bar 10nm in all three images)

5.3. *In situ* mechanical and electrical measurements

In order to quantitatively determine the strength of the as-welded structures, an *in situ* TEM-AFM holder was used to perform tensile tests on as-welded nanowires, as illustrated in Fig. 5-6 a.

The TEM-AFM holder was used primarily for quantitative measurement of nanowire strength, on which a silicon AFM cantilever beam with known spring constant (4.8N/m) was deflected by the clamped nanowire sample under tensile loading. The sample attachment to the AFM cantilever was made by pushing nanowire against the AFM tip surface, which was coated with an adhesive layer, until strong bonding was formed. Since the deflection of the cantilever is much smaller than its length, a linear relationship between ΔD (displacement of the AFM tip, same as the cantilever deflection) and F (force applied on the nanowire sample) was assumed. During the experiment, a selected area diffraction (SAD) center-spot blocking bar which is free of movement throughout the process of taking TEM images and videos was inserted as the reference for displacement measurements. The tensile strength was calculated as engineering stress. The stress calculation was reasonably accurate (less than ±10% error) with magnified views of cantilever deflections in TEM images.

It should be noted that the two nanowire samples to be welded were first obtained by breaking one original gold nanowire, with measured tensile strength ~ 600±50MPa (engineering stress). A side-to-side cold-welding experiment was performed following the breaking of the original nanowire. Once the joining and relaxation process were completed (Fig. 5-6 b-c), we pulled the as-welded nanowire away from the AFM tip. Again the breaking point was not in the welding zone. By measuring the deflection of the

AFM cantilever (ΔD), a tensile strength about 580±40MPa (engineering stress) was obtained. This compares very well with the strength of the original nanowire. In contrast, the tensile strength for bulk gold is normally about 100MPa [144]. The drastically increased mechanical strength for gold nanowires was experimentally and computationally demonstrated before [16, 19] (It has been well recognized that there exists a strong size effect in mechanical behaviours for metals and more generally, "smaller is stronger" ([16] and the included references). At nanometer length scale, the structure of materials such as nanowires is normally free of defects, and the deformation mechanism is quite different from that of bulk materials. As such, the strength of nanowires can even approach the ideal strength of materials. The observed high mechanical strength for gold nanowires in this study correlates well with earlier results obtained both experimentally and computationally [16, 19].). These measurements clearly confirmed that as-welded nanowires had maintained the superior mechanical properties as the original single crystalline nanowires.

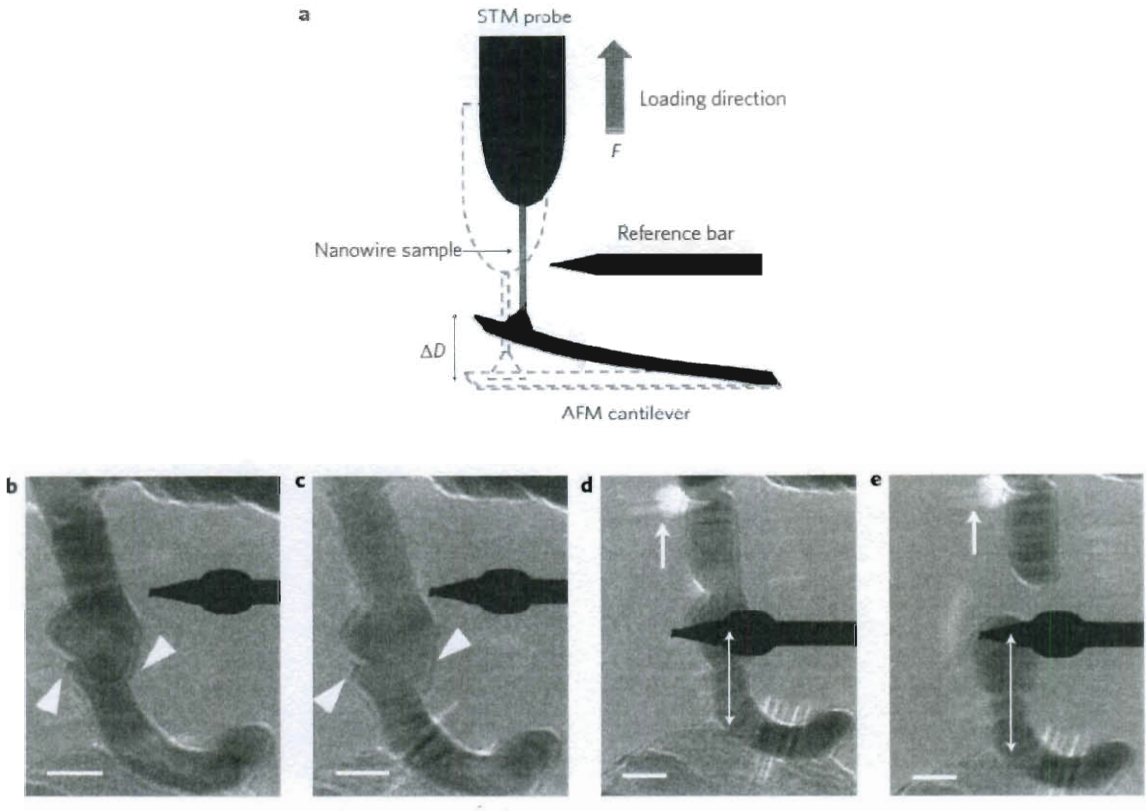

Figure 5-6 *In situ* tensile measurements. (a) A schematic illustration shows how the AFM cantilever acted as a force sensor (by measuring the deflection of the cantilever ΔD) and the STM probe acted as an actuator while attached nanowire sample was under tensile loading; (b-c) Two gold nanowires before and after cold-welding on the TEM-AFM holder; (d) The as-welded nanowire under the maximum load state and (e) The broken nanowires at the steady state (note that the breaking point was no longer the same as the initial contact point); The thin double-headed arrows in (d) and (e) indicate the relative displacements of the AFM cantilever tip with respect to the reference bar; Triangles show the edges of two nanowires before and during welding while the thicker single-headed arrows indicate the tensile loading direction. (Scale bar 10nm)

Finally *in situ* electrical measurements on the original and as-welded nanowires using the TEM-STM holder were carried out and compared for their current-voltage (I-V) responses. In Fig. 5-7 a, a gold nanowire (~130nm in length, ~7nm in diameter) was bridged between gold probes. By applying -1 to +1mV bias, we repeated I-V measurements for total nine times, and obtained an average electrical resistivity 292.6±5.8Ω•nm. The subsequent as-welded nanowires were then obtained by breaking the original nanowire and re-welding together, such as shown in Fig. 5-7 b-c. Total eleven times of breaking and re-welding were performed, through either side-to-side or head-to-head modes at different welding locations (since as-welded nanowires oftentimes broke at a different location than the previous welding spot). Electrical measurements were performed at least twice for each as-welded nanowire. The corresponding averaged I-V curves were plotted in Fig. 5-7 d, along with that of the original nanowire. An average electrical resistivity 298.1±14.5Ω•nm was obtained from all eleven successfully welded nanowires. It clearly demonstrated that the electrical resistivity had little change for each successful welding, and the average resistivity of as-welded samples was indeed very close to that of the original nanowire. These results also compare very well with the resistivity data (260Ω•nm) in Ref. [41] for the same micron-long ultrathin gold nanowires. Even without full correction of contact resistance, the electrical resistivities of these original and as-welded nanowires were already lower than many other types of gold nanowires with diameter ranging from 4nm to 90nm [e.g. 184-186], clearly suggesting great potentials of using ultrathin gold nanowires as future interconnects and cold-welding as an efficient nanoscale assembly technique.

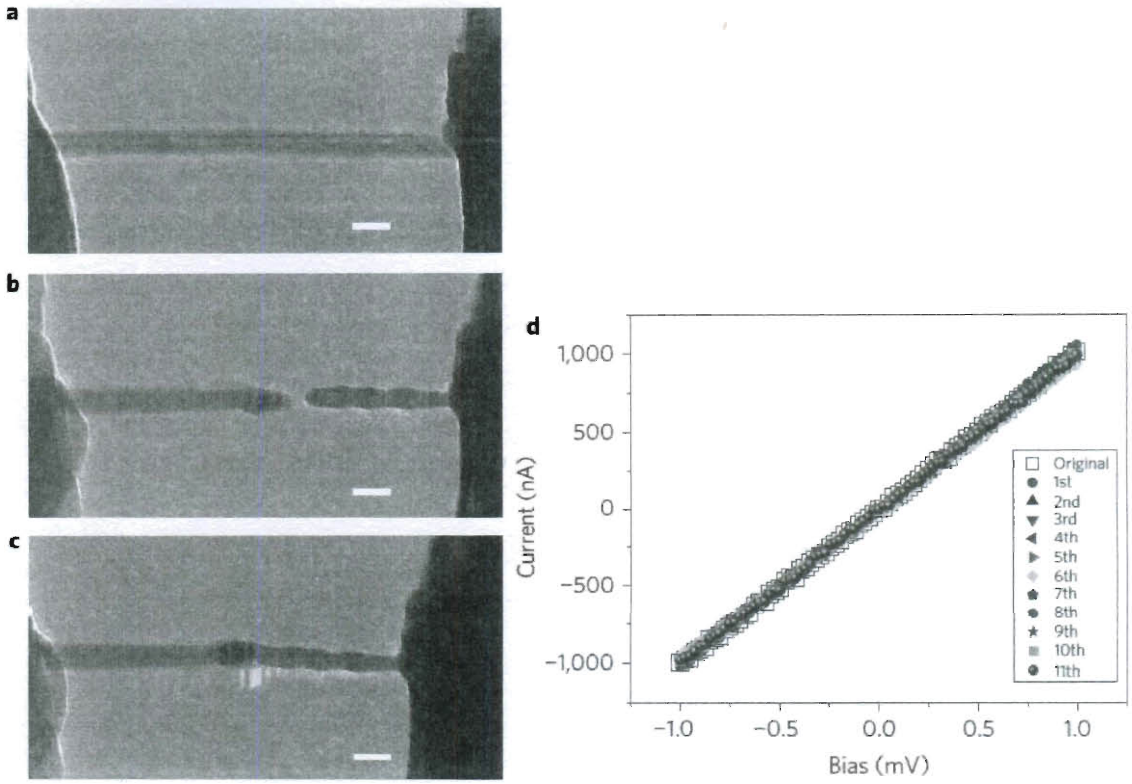

Figure 5-7 *In situ* electrical measurements. (a-c) For a gold nanowire with 130 nm in length and 7 nm in diameter bridged between gold probes at initial, broken, and welding states (Scale bar 10nm); (d) The comparison of the averaged I-V curves of the original and as-welded gold nanowires; Cold-welding was successfully performed eleven times with the same sample by breaking and re-welding the nanowire, such as shown in (a-c); The Y-axis (current) error was ~2% for the original nanowire measurement and ~5% for each measurement of as-welded nanowire.

5.4. Comparison with heating-involved welding and macroscopic cold-welding

In contrast to other existing techniques for joining individual nanostructures, the demonstrated technique distinguished itself by requiring no local heating process, i.e. no need to apply bias or to use dedicated heating stage. Additional heating effects from the electron beam can be ruled out [187-188], since only low intensity spread electron beams were used for imaging (First of all, it might be noted that cold-welding experiments were also successfully performed at 100KV low dose condition as well as the beam-blank condition. However, even when the TEM was operated at 300KV, according to [187] and the Supporting Information of [177], temperature increase due to electron beam irradiation effect will be limited within about 10 °C with low intensity electron beam condition. In addition, as estimated from the energy-loss spectrum [188], the increasing of temperature associated with electron beam irradiation can be really small (less than 7K) for gold nanoparticles with radius above 2nm on substrates with good thermal conductivity. Considering that the radii of the ultrathin nanowires used in this study were right all above 2 nm, and samples were attached to gold or tungsten probes with conductive silver paste, electron beam heating effects were thought to be not significant in current study.).

The cold-welding processes were also faster than most other welding processes involving heating [e.g. 173, 175-177] and were completed at near room temperature with no observable fusion occurred at the welding interface. As a result, the single crystalline structures of the original and as-welded nanowires were well maintained during the welding process, with almost no defects or impurities introduced. The strength of as-welded nanowires was at least as strong as that of original nanowires, due to the fact that the welding zone had the same lattice structure and connected to the original wires with

no observable grain boundaries. It also appears that the cold-welding had very little effect on electron conduction---this could again be attributed to the near perfect welding zone formed during this process.

More importantly, we have successfully extended this technique to other metal systems, that is, cold-welding also occurs between silver-silver nanowires, (Fig. 5-8), as long as they are single crystals with matching orientation and clean surfaces, and with small diameters (usually less than 20nm).

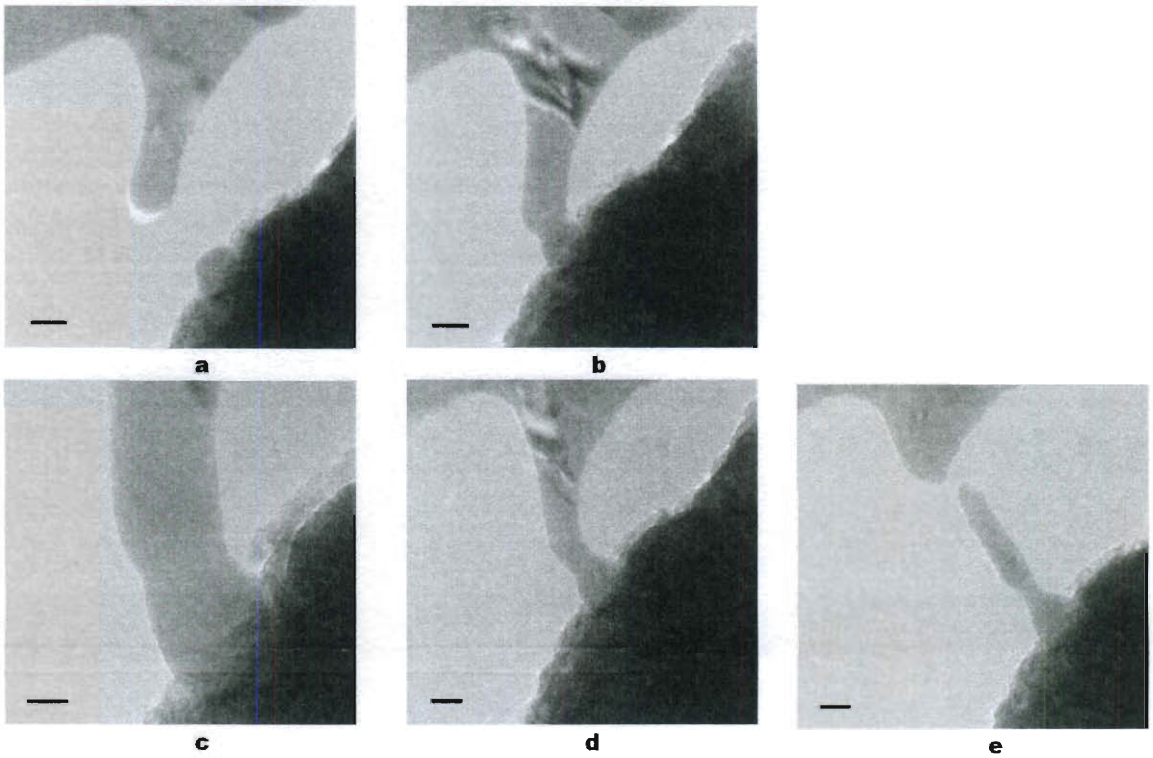

Figure 5-8 Cold-welding of ultrathin silver nanowires/nanorods. (a) a silver nanowire (top) was approaching to a silver nanorod (bottom); (b) cold-welding occurred once their front surfaces touched each other; (c) high magnification images of the welding zone; (d) the as-welded silver nanowire after relaxation; (e) in situ pulling test was performed and the as-welded silver nanowire broke at a different location rather than the welding section. Scale bars in (a), (b), (d), (e) are 10nm, and in (c) is 5nm.

On the other hand, for joining between dissimilar materials, so far we observed that cold-welding could easily occur between gold and silver (Fig. 5-9), which should be attributed to their similar crystalline structures and lattice spacing

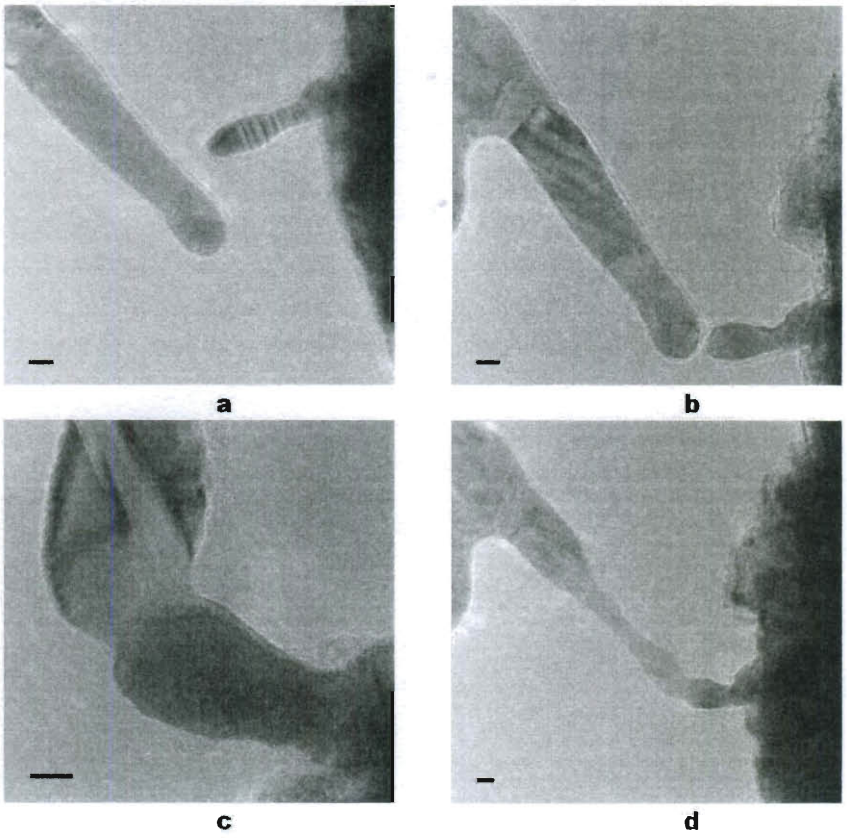

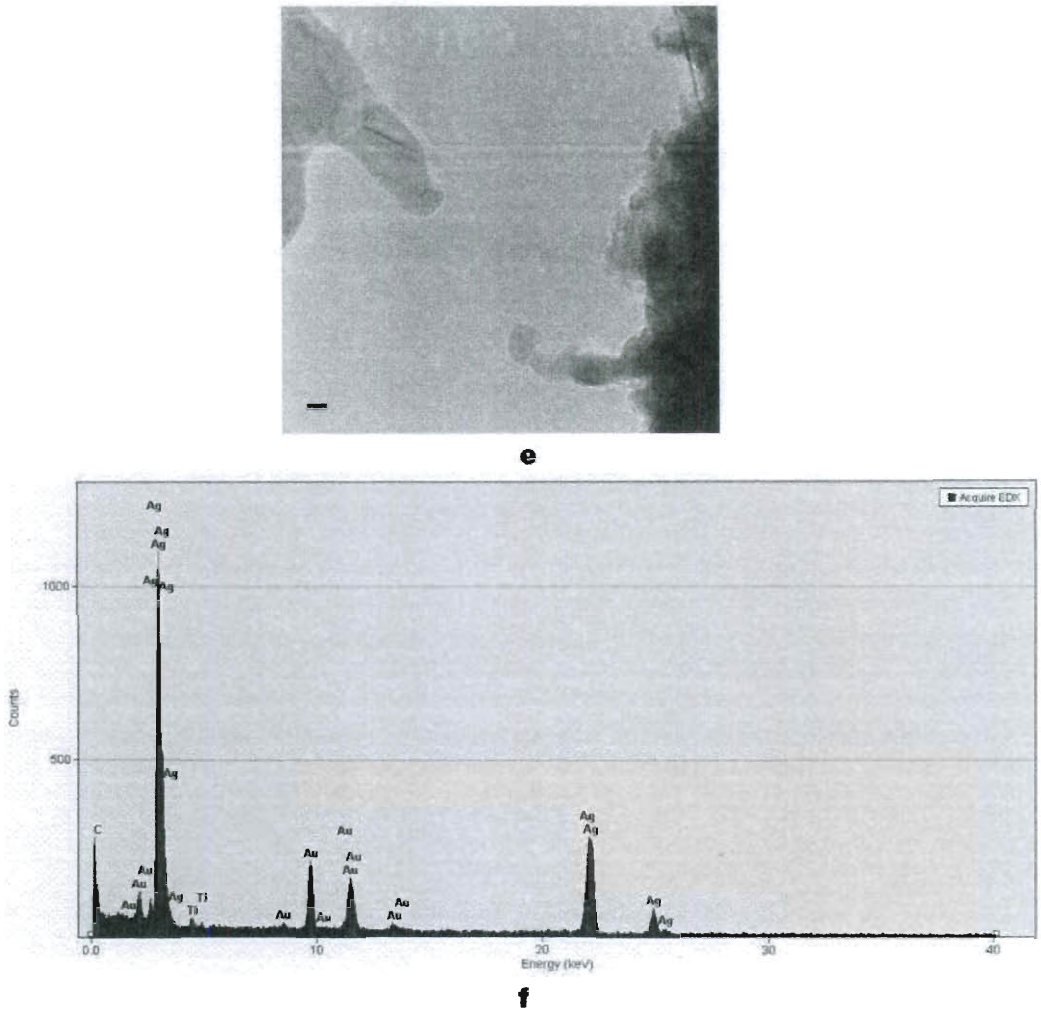

Figure 5-9 Cold-welding process between a silver nanowire and a gold nanowire. (a) an ultrathin gold nanowire (right, diameter ~10nm) was approaching to a silver nanowire (left, diameter ~15-20nm); (b) cold-welding didn't occur instantly as they touched each other due to the existence of surface surfactants on gold nanowires; (c) after removal of the surface layer on their front edges, cold-welding occurred quickly; (d) the as-welded Au-Ag nanowire structure after relaxation; (e) *in situ* pulling of the as-welding nanowire structures was performed and the breaking point was in the original silver nanowire section, rather than at the Au-Ag welding zone; (f) EDAX showing the composition of the nanowires. Scale bars in (a), (b), (d) and (e) are 10nm and in (c) is 5nm.

Unlike the traditional cold-welding of bulk materials which normally requires high load, the cold-welding of ultrathin nanowires described in this paper could occur easily for "head-to-head" welding experiments with matching crystalline orientations and little external force was needed. While for "side-to-side" welding mode, the joining could occur by only making mechanical contact between the nanowires to be welded and no significant deformation due to contact was found in all experiments. Although the exact contact geometry and applied load were difficult to quantify at the joining interface, an estimation of the applied stress to join nanowires in the side-to-side geometry (Fig. 5-2 b) was attempted using simple beam theory. Assuming a small lateral deflection of δ=1nm for an 100nm-long nanowire sample (Fig. 5-2 c) resulted from the side-to-side contact with contact surface area of ~10nm2, and using Young's modulus ~70GPa for common gold nanowires [16], the calculated applied stress is only ~4.7MPa. This value is considered as the upper limit of the actual applied stress, since very little lateral deflection was seen in the actual experiments using the side-to-side welding. This value, not only much smaller than the requirement for traditional cold-welding of bulk metals, is also smaller than the required pressure for cold-welding of metallic thin film (larger than 100MPa in [167]). It should be noted that, the reported pressure for cold-welding of gold thin film (0.1g/cm2, i.e. 9.8Pa in [166]) represents the average stress over a large 1cm-by-1cm area which could have many local contact points due to surface asperities. The actual pressure for individual asperities would likely be much higher. Therefore, this work may offer a nanoscopic view of the initial stages of macroscopic cold-welding for either bulk metals or metallic thin film.

5.5. Mechanisms of nanoscale cold-welding

Atomic diffusion and surface relaxation that were considered as important factors in macroscopic cold-welding were obviously at play in aforementioned nanoscale process [165, 166, 178]. It is well recognized that the diffusion barrier of a single metal atom on metal surface is quite low (typically less than 1ev) [189]. Thermal activation at even room temperature is enough to overcome such low barriers, so isolated metal atoms can diffuse rapidly through surface diffusion. However, to create such isolated atoms requires much higher energy cost. It is the combination of the formation and diffusion energy barriers that determine the cold-welding observed in this work. The mechanical manipulation clearly provided the necessary extra driving force which facilitates the cold-welding and unification of two nanowires.

Additionally, we believe that the "oriented attachment" mechanism as reported for PdSe nanocrystal [177, 190], was also playing an important role in welding occurring at near room temperature. One evidence is that cold-welding always occurred easily and instantly between two nanowires with the same growth orientation, especially for those that were obtained by breaking one original nanowire into two segments. The matching orientation is therefore a key to realize successful welding. It will certainly be very interesting future work to verify if the aforementioned mechanically assisted surface atom diffusion alone could facilitate cold-welding of nanowires with different crystal orientations. On the other hand, while PbSe nanocrystal particles still require a low temperature heating (100°C-150°C [177]) for unification, the welding process reported here had no such requirement. This could be understood as following: Firstly, the mechanical manipulation of the nanowire, instead of local heating, helped samples to

match their orientation with each other, as the beginning of the "oriented attachment" process [177]. Secondly, as in traditional cold-welding, clean surface in high vacuum is an important factor [165, 166] and gold nanowire samples (especially for freshly broken nanowires) in TEM chamber clearly satisfied this requirement.

5.6. Conclusion

Herein, the cold-welding technique demonstrates the capability of joining ultrathin gold nanowires without introducing defects. The welding occurred at near room temperature with exceptional quality is attributed to nanoscale sample dimensions, oriented attachment mechanisms as well as mechanically assisted surface atom diffusions. This process requires no heating or high load, and can be done relatively fast. More importantly, both mechanical and electrical properties of nanowires were not affected by the cold-welding. These results provide the first atomic scale visualization of the cold-welding process, revealing for the first time the physical mechanisms of cold-welding of nanowires. Combining with other nano/micro-fabrication technologies [191-193], nano-scale cold-welding is expected to have potential applications for future bottom-up assembly of metallic 1-D nanostructures and next-generation interconnects for extreme dense logic circuits.

Chapter 6

Concluding Remarks

In the past decade, a tremendous amount of experimental and theoretical research has been conducted to characterize one dimensional nanostructures. However, the characterization of 1-D metallic nanostructures remains very challenging, especially for *in situ* tensile testing for samples with different diameters. In this thesis study, we present the usage of two dedicated platforms, based on (1) a novel micro mechanical device (MMD) assisted with a quantitative nanoindenter and (2) a TEM-AFM sample holder system, to perform *in situ* tensile tests within a SEM and a TEM on gold and nickel nanowires with diameter ranging from a few nanometers to hundreds of nanometers.

Size dependent mechanical behavior was clearly revealed through our systematical study on gold nanowires. Figure 6-1 shows that the dependence of engineering tensile breaking strength as a function of nanowire diameter. We found that, while "smaller is stronger" still holds in general, the increases in the breaking strength (the slope through linear fitting in the log-log scale) for nanowires with 100-300nm diameters were higher than that of ultrathin gold nanowire (D<15nm), as shown in Figure 6-1.

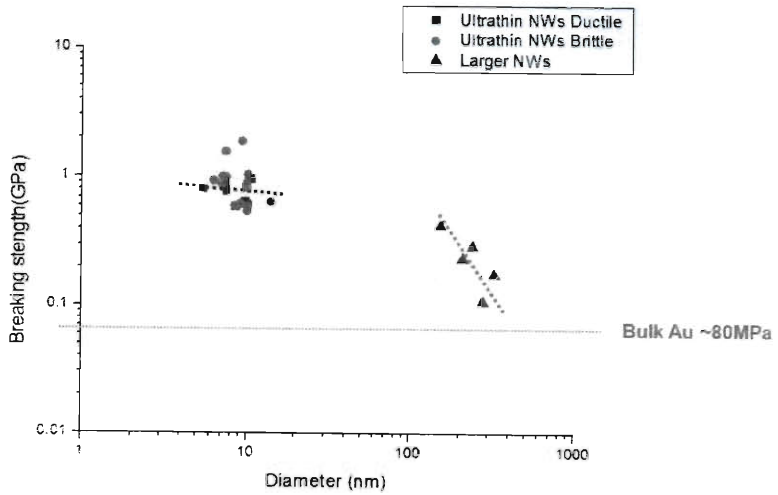

Figure 6-1 Size dependence of mechanical behavior of gold nanowires (Engineering breaking strength versus Diameter in log scale): the black squares and red circles were from ultrathin gold nanowire tests inside a TEM and the blue triangles were from the larger diameter gold nanowire tested by micro mechanical devices inside a SEM.

These trends well agree to those obtained via previously conducted pillar compression studies [145], confirming the different deformation mechanisms for 1-D metallic nanostructures within different diameter ranges. According to the [145], for 1-D metallic nanostructures with smaller diameters (i.e. less than 20nm), surface dislocation nucleation would be expected to dominate the deformation process. Our in situ HRTEM experiments on ultrathin gold nanowires further confirmed this phenomenon and the quantitative measurements clearly showed that, for nanowire with ultra-small diameters, a lower strain rate would result in higher strength values (Figure 6-2), which also agree very well with the theoretical studies [4].

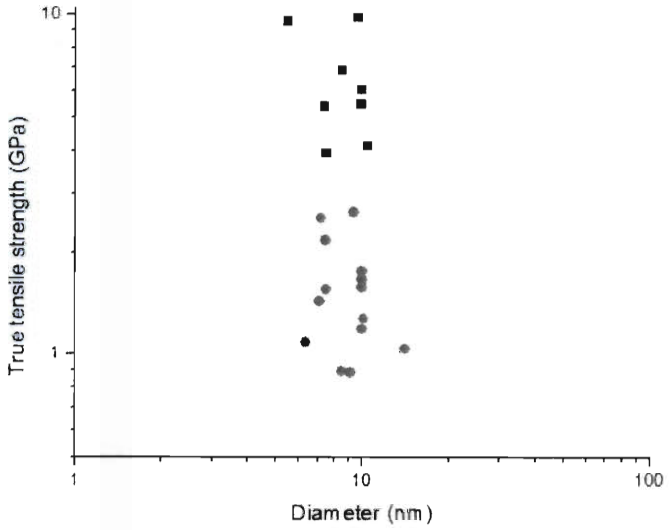

Figure 6-2 Strain rate effects on true breaking strength for ultrathin gold nanowires: the black square were from testing results with high strain rate (average ~0.0013/s) while the red circles were from low strain rate tests (average ~0.0004/s).

Furthermore, due to the tensile testing geometry, fractures of 1-D nanomaterials were characterized. With *in situ* testing, we were able to clearly observe the fracture morphology of the sample during and after breaking. We found that, for larger diameter gold nanowires (200-300nm in diameter), samples underwent typical ductile fracture; for larger diameter nickel nanowires (200-300nm in diameter) samples usually broke in very brittle mode. More interestingly, systematical study on ultrathin gold nanowires showed that the same pristine single crystalline samples can break with distinctively different fracture morphologies. In-depth HRTEM experiments showed that the unusual brittle fractures were associated with twin structures formed during initial loading with misalignment. Due to the small sample sizes for ultrathin gold nanowires tested, we were able to perform molecular dynamics (MD) simulations for similar the experiments and directly compare the results. Via MD simulation, it was shown that a small amount of

initial misalignment can indeed introduce multiple twin structures as appear in the experiments. In addition, the comparison for nanowires with and without initial twin boundaries under tensile loading in MD simulations showed that nanowire with twin structures would break with much less strain and appear more "brittle-like". These results can potentially offer significant insights towards the reliability of future nano electronic and electromechanical devices consisting of these fascinating nanoscale building blocks.

Finally, "cold welding" phenomenon was discovered for gold and silver nanowires with diameters less than 20nm. This novel physical phenomenon is attributed to the nanoscale sample dimensions, oriented-attachment mechanisms, as well as mechanically assisted surface atom diffusions. Thus it can be considered as another size dependent property for nanomaterials. Combined with other nano- and microfabrication technologies [191-193], nanoscale cold welding is anticipated to have potential applications in the future bottom-up assembly of metallic one-dimensional nanostructures and next-generation interconnects for extremely dense logic circuits.

Further work in the direction of this thesis may include:

(1) Use the micro mechanical device to test more gold and nickel nanowires with smaller diameters for size effect study. For example, there remains a gap between 20 and 100nm in Figure 6-1. At present, we can grow gold nanowires with diameter in this range but cannot grow them to be long enough for tests with the micro mechanical device. In addition, the sample clamping technique needs to be improved for nanowires with smaller diameters (less than 100nm).

(2) Perform *in situ* tensile testing on larger diameter Ni and Au nanowires inside TEM. While we can observe morphology evolution in SEM, TEM imaging (with appropriate orientation) can provide much more information about the change in crystalline structures and reveal the underlying deformation mechanisms.

(3) Perform in situ quantitative mechanical and electrical measurements for Ni nanowires with unique twin structures (lamellar/parallel twin and five-fold twin) and compare their properties to that of single crystalline Ni nanowires. In addition, the formation mechanisms for these twin structures and how they interact with other defects such as dislocations will be particular interesting.

(4) Further develop cold welding technique into a scalable nanowire integration process. Current setup, involving in situ manipulation by STM probes within TEM remains low efficient and expensive. However, by combining with other available bottom-up assembly techniques, such as Langmuir-Blodgett (LB) method [192] for example, it is possible to pattern ultrathin gold nanowire crossbar arrays, as illustrated in Figure 6-3.

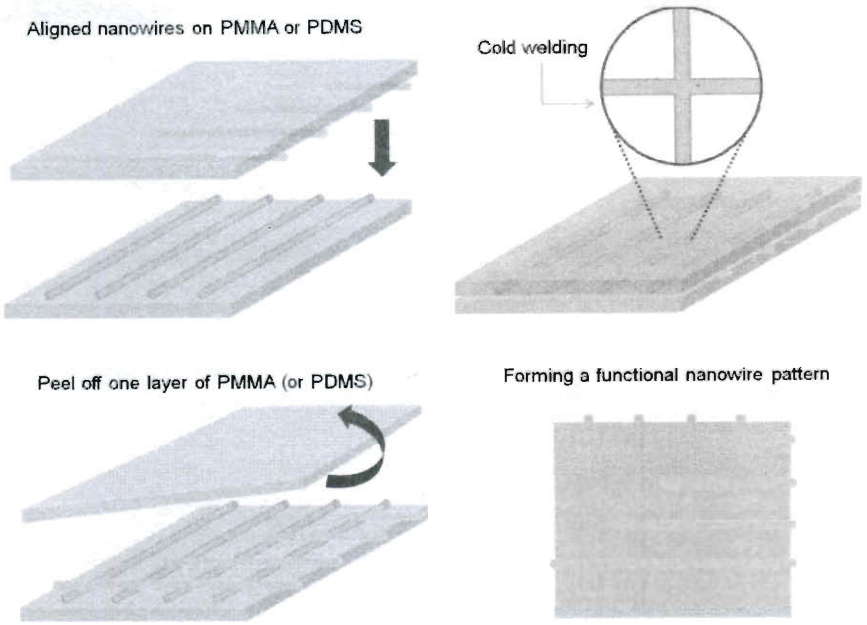

Figure 6-3 Schematic illustration of cold welding for crossbar nanowire arrays (nanowires could be initially aligned by Langmuir-Blodgett (LB) method [181])

References

[1] Meyer, M.A. and Chawla, K.K. "Mechnical Behavior of Materials," (Upper Saddle River, NJ: Prentic-Hall, 1998)

[2] Li, J. "The Mechanics and Physics of Defect Nucleation," MRS Bulletin (2007) 32, 151-159

[3] Rabkin, E. and Srolovitz, D.J. "Onset of plasticity in gold nanopillar compression," Nano Lett. (2007) 7, 101-107

[4] Zhu, T., Li, J., Samanta, A., Leach, A. and Gall, K. "Temperature and Strain-Rate Dependence of Surface Dislocation Nucleation," Phys. Rev. Lett. (2008) 100, 025502

[5] Cao, A., Wei, Y. and Mao, S.X. "Alternating starvation of dislocations during plastic yielding in metallic nanowires," Scripta Mater. (2008) 59, 219–222

[6] Froseth, A., Van Swygenhoven, H. and Derlet, P.M. "The influence of twins on the mechanical properties of nc-Al," Acta Mater. (2004) 52, 2259-2268

[7] Afanasyev, K.A. and Sansoz, F. "Strengthening in Gold Nanopillars with Nanoscale Twins," Nano Lett. (2007) 7, 2056–2062

[8] Diao, J., Gall, K. and Dunn, M.L. "Yield Strength Asymmetry in Metal Nanowire," Nano Lett. (2004) 4, 1863–1867

[9] Liang, W. And Zhou, M. "Shape Memory Effect in Cu Nanowires" Nano Lett. (2005) 5, 2039–2043

[10] Arzt, E. "Size effects in materials due to microstructural and dimensional constraints: a comparative review," Acta Mater. (1998) 46, 5611-5626

[11] Nix, W.D. "Mechanical properties of thin films," Metall. and Mater. Trans. A (1989) 20, 2217-2245

[12] Brotzen, F.R. "Mechanical testing of thin films," Inter. Mater. Rev. (1994) 39, 24-45

[13] Kraft, O. and Volkert, C.A. "Mechanical Testing of Thin Films and Small Structures," Adv. Eng. Mater. (2001) 3, 99-110

[14] Lou, J., Allameh, S., Buccheit, T. And Soboyejo, W.O. "An investigation of the effects of thickness on mechanical properties of LIGA nickelMEMS structure," J. Mater. Sci. (2003) 38, 4129-4135

[15] Uchic, M.D., Dimiduk, M.D., Florando, J.N. and Nix, W.D. "Sample Dimensions Influence Strength and Crystal Plasticity," Science (2004) 305, 986-989

[16] Wu, B., Heidelberg, A. and Boland, J.J. "Mechanical properties of ultrahigh-strength gold nanowires," Nature Mater. (2005) 4, 525 – 529

[17] Greer, J.R. and Nix, W.D. "Size dependence of mechanical properties of gold at the sub-micron scale," Appl. Phys. A (2005) 80, 1625-1629

[18] Greer, J.R. and Nix, W.D. "Nanoscale gold pillars strengthened through dislocation starvation," Phys. Rev. B. (2006) 73, 245410

[19] Gall, K., Diao, J. and Dunn, M.L. "The Strength of Gold Nanowires," Nano Lett. (2004) 4, 2431–2436

[20] Cui, Y. and Lieber, C. M. "Functional nanoscale electronic devices assembled using silicon nanowire building blocks," Science (2001) 291, 851-853

[21] Duan, X.F., Huang, Y., Cui, Y., Wang, J.F. and Lieber, C.M. "Indium phosphide nanowires as building blocks for nanoscale electronic and optoelectronic devices," Nature (2001) 409, 66-69

[22] Narayanan, T.N., Shaijumon, M.M., Ci, L., Nayak, S. and Ajayan, P.M. "On the growth mechanism of Ni and Co nanowires and comparison of their magnetic properties," Nano Research (2008) 1, 465-473

[23] Cui, Y., Wei, Q.Q., Park, H.K. and Lieber, C.M. "Nanowire nanosensors for highly sensitive and selective detection of biological and chemical species," Science (2001) 293, 1289-1292

[24] Huang, M.H. et al. "Room-temperature ultraviolet nanowire nanolasers," Science (2001) 292, 1897-1899

[25] Wang, Z.L. "ZnO nanowire and nanobelt platform for nanotechnology," Mater. Sci. & Eng. R. (2009) 64, 33-71

[26] Law, M., Goldberger, J. and Yang, P.D. "Semiconductor nanowires and nanotubes," Ann. Rev. Mater. Res. (2004) 34, 83-122

[27] Fang, X.S. et al. "Ultrafine ZnS Nanobelts as Field Emitters," Adv. Mater. (2007) 19, 2593-2596

[28] Pan, Z.W., Dai, Z.R. and Wang, Z.L. "Nanobelts of semiconducting oxides," Science (2001) 291, 1947-1949

[29] Xia, Y. et al. "One-Dimensional Nanostructures: Synthesis, Characterization, and Applications," Adv. Mater. (2003) 15, 353-389

[30] Huynh, W.U., Janke J. Dittmer,J.J. and Alivisatos, P.A. "Hybrid Nanorod-Polymer Solar Cells," Science (2002) 295, 2425-2427

[31] Wang, X., Summers, C.J. and Wang, Z.L. "Large-Scale Hexagonal-Patterned Growth of Aligned ZnO Nanorods for Nano-optoelectronics and Nanosensor Arrays" Nano Lett. (2004) 4, 423-426

[32] Liu, Z., Winters, M., Holodniy, M. and Dai, H. J. "siRNA delivery into human T cells and primary cells with carbon-nanotube transporters," Angew. Chem.-Int. Edit. (2007) 46, 2023-2027

[33] Sadrzadeh, A., Farajian,A.A. and Yakobson, B.I. "Electron transport of nanotube-based gas sensors—An ab initio study," Appl. Phys. Lett. (2008) 92, 022103

[34] Kang, J.S. et al. "High-performance electronics using dense, perfectly aligned arrays of single-walled carbon nanotubes," Nature Nanotech. (2007) 2, 230 - 236

[35] Endo, M., Strano, M.S. and Ajayan, P.M. "Potential applications of carbon nanotubes," Carbon nanotubes, Topics in Applied Physics (Springer-Verlag Berlin Heidelberg, 2008) 111, 13-62

[36] Wu, Y., Xiang, J., Yang, C., Lu, W. and Lieber, C.M. "Single-crystal metallic nanowires and metal/semiconductor nanowire heterostructures," Nature (2004) 430, 61-65

[37] Husain, A. et al. "Nanowire-based very-high-frequency electromechanical resonator," Appl. Phys. Lett. (2003) 83, 1240-1242

[38] Lu, W. and Lieber, C.M. "Nanoelectronics from the bottom up," Nature Mater. (2007) 6, 841–850

[39] Xiong, Y., Liu, Z. and Zhang, X. "A simple design of flat hyperlens for lithography and imaging with half-pitch resolution down to 20 nm," Appl. Phys. Lett. (2009) 94, 203108

[40] Cademartiri, L. and Ozin, G. A. "Ultrathin Nanowires-A Materials Chemistry Perspective," Adv. Mater. (2009) 21, 1013-1020

[41] Wang, C., Hu, Y., Lieber, C. M. and Sun, S. "Ultrathin Au nanowires and their transport properties," J. Am. Chem. Soc. (2008) 130, 8902–8903

[42] Huo, Z., Tsung, C., Huang, W., Zhang, X. and Yang, P. "Sub-Two Nanometer Single Crystal Au Nanowires," Nano Lett. (2008) 8, 2041-2044

[43] Lu, X., Yavuz, M.S., Tuan, H., Kogel, B.A. and Xia, Y. "Ultrathin Gold Nanowires Can Be Obtained by Reducing Polymeric Strands of Oleylamine-AuCl Complexes Formed via Aurophilic Interaction," J. Am. Chem. Soc. (2008) 130, 8900–8901

[44] Feng, H. et al. "Simple and rapid synthesis of ultrathin gold nanowires, their self-assembly and application in surface-enhanced Raman scattering," Chem. Commun. (2009) 1984-1986

[45] Hong, B. H., Bae, S.C., Lee, C.W., Jeong, S. and Kim, K.S. "Ultrathin single-crystalline silver nanowire arrays formed in an ambient solution phase," Science (2001) 294, 348-351

[46] Zhao, J.J., Buia, C.L., Han, J. and Lu, J.P. "Quantum transport properties of ultrathin silver nanowires," Nanotechnology (2003) 14, 501-504

[47] Tang, Z.Y. and Kotov, N.A. "One-Dimensional Assemblies of Nanoparticles: Preparation, Properties and Promise," Adv. Mater. (2005) 17, 951-962

[48] Liu, J.W., Zhu, J.H., Zhang, C.L., Liang, H.W. and Yu, S.H. "Mesostructured Assemblies of Ultrathin Superlong Tellurium Nanowires and Their Photoconductivity," J. Am. Chem. Soc. (2010) 132, 8945–8952

[49] Liang, H. et al. "Ultrathin Te Nanowires: An Excellent Platform for Controlled Synthesis of Ultrathin Platinum and Palladium Nanowires/Nanotubes with Very High Aspect Ratio," Adv. Mater. (2009) 21, 1850-1854

[50] Teng, X., Han, W., Ku, W. and Hucker M. "Synthesis of Ultrathin Palladium and Platinum Nanowires and a Study of Their Magnetic Properties," Angew. Chem. Int. Ed. (2008) 47, 2055-2058

[51] Lu, Y., Huang, J.Y., Wang, C., Sun, S., Lou, J. "Cold Welding of Ultrathin Gold Nanowires," Nature Nanotech. (2010) 5, 218-224

[52] Sadeghian, R.B. and Kahrizi,M. "A novel miniature gas ionization sensor based on freestanding gold nanowires," Sensors and Actuators A. (2007) 137, 248–255

[53] Aravamudhan, S., Ramgir, N.S. and Bhansali, S. "Electrochemical biosensor for targeted detection in blood using aligned Au nanowires," Sensors and Actuators B (2007) 127, 29–35

[54] Bauer, L.A., Birenbaum,N.S. and Meyer,G.J. "Biological applications of high aspect ratio nanoparticles," J. Mater. Chem. (2004) 14, 517 – 526

[55] Zhang, X. et.al. "Optical polarizers based on gold nanowires fabricated using colloidal gold nanoparticles," Nanotechnology (2008) 19, 285202

[56] Schmidt, M.A., Prill Sempere, L.N., Tyagi, H.K. and Poulton, C.G. "Waveguiding and plasmon resonances in two-dimensional photonic lattices of gold and silver nanowires," Phys. Rev. B. (2008) 77, 033417

[57] Chou, C.H., Chen, C.D. and Wang,C.R. "Highly efficient, wavelength-tunable, gold nanoparticle based optothermal nanoconvertors" J. Phys. Chem. B. (2005) 109, 11135-11138

[58] Huang, X., Neretina, S. And El-Sayed, M.A. "Gold Nanorods: From Synthesis and Properties toBiological and Biomedical Applications," Adv. Mater. (2009) 21, 4880-4910

[59] Tanase, M. et al. "Magnetic Alignment of Fluorescent Nanowires," Nano Lett. (2001) 1, 155–158

[60] Zhang, L. et al. "Controlled Propulsion and Cargo Transport of Rotating Nickel Nanowires near a Patterned Solid Surface," ACS Nano (2010) 4, 6228-6234

[61] Walter, E.C. et al. "Sensors from electrodeposited metal nanowires," Surface and Interface Analysis (2002) 34, 409-412

[62] Salem, A.K., Searson, P.C. and Leong, K.W. "Multifunctional nanorods for gene delivery," Nature Mater. (2003) 2, 668-671

[63] Reich, D.H. et al. "Biological applications of multifunctional magnetic nanowires," J. Appl. Phys. (2003) 93, 7275

[64] Hurst, S.J., Payne, E.K., Qin, L. and Mirkin, C.A. "Multisegmented One-Dimensional Nanorods Prepared by Hard-Template Synthetic Methods," Angew. Chem. Int. Ed. (2006) 45, 2672-2692

[65] Brenner, S.S. "Tensile strength of whiskers," J. Appl. Phys. (1956) 27, 1484–1491

[66] Fisher, J.C. and Hollomon, J.H. "A statistical theory of fracture," Trans. Amer. Inst. Mining Metall. Eng. (1947) 171, 546–561

[67] Fleck, N.A., Muller, G.M., Ashby, M.F. and Hutchinson J.W. "Strain Gradient Plasticity: Theory and Experiment," Acta Metall. Mater. (1994) 42, 475-487

[68] Fleck, N.A. and Hutchinson, J.W. "Strain Gradient Plasticity," Adv. in Appl. Mech. (1997) 33, 295-361

[69] Acharya, A. And Bassani, J.L. "Lattice incompatibility and a gradient theory of crystal plasticity," J. Mech. Phys. Solids (2000) 48, 1565-1595

[70] Gao, H. and Huang, Y. "Geometrically necessary dislocation and size-dependent plasticity" Scripta Mater. (2003) 48, 113-118

[71] Volkert, C.A. and Lilleodden, E.T. "Size effects in the deformation of sub-micron Au columns," Philos. Mag. (2006) 86, 5567–5579

[72] Gilman, J.J. "Deformation of symmetric zinc bicrystals," Acta Metallurgica (1953) 1, 426-427

[73] Maa□, R. et al. "Defect structure in micropillars using x-ray microdiffraction" Appl. Phys. Lett. (2006) 89, 151905

[74] Bei, H., Shim, S., Miller, M.K., Pharr, G.M. and George, E.P. "Effects of focused ion beam milling on the nanomechanical behavior of a molybdenum-alloy single crystal," Appl. Phys. Lett. (2007) 91, 111915

[75] Deshpande, V.S., Needleman, A. and Van der Giessen, E. "Plasticity size effects in tension and compression of single crystals," J. Mech. Phys. Solids (2005) 53, 2661-2691

[76] Zhang, H., Schuster, B.E., Wei, Q. and Ramesh, K.T. "The Design of Accurate Micro-compression Experiments," Scripta Mater. (2006) 54, 181–186

[77] Jing, G.Y., Ji, H., Yang, W.Y., Xu, J. and Yu, D.P. "Study of the bending modulus of individual silicon nitride nanobelts via atomic force microscopy," Appl. Phys. A (2006) 82, 475-478

[78] Wu, B., Heidelberg, A., Boland, J.J., Sader, J.E., Sun, X. and Li, Y. "Microstructure-hardened silver nanowires," Nano Lett. (2006) 6, 468-472

[79] Li, X., Wang, X., Xiong, Q. and Eklund, P.C. "Mechanical Properties of ZnS Nanobelts," Nano Lett. (2005) 5, 1982–1986

[80] Kumar, K.S., Van Swygenhoven, H. and Suresh, S. "Mechanical behavior of nanocrystalline metals and alloys," Acta Mater. (2003) 51, 5743–5774

[81] Tjong, S.C. and Chen, H. "Nanocrystalline materials and coatings," Mater. Sci. Eng. R (2004) 45, 1-88

[82] Lu, L., Shen, Y., Chen, X., Qian, L. and Lu, K. "Ultrahigh Strength and High Electrical Conductivity in Copper" Science (2004) 304, 422-426

[83] Wu, X., Zhu, Y.T., Chen, M.W. and Ma, E. "Twinning and stacking fault formation during tensile deformationof nanocrystalline Ni" Scripta Mater. (2006) 54, 1685-1690

[84] Diao, J., Gall, K. and Dunn, M.L. "Surface-stress-induced phase transformation in metal nanowires," Nat. Mater. (2003) 2, 656-660

[85] Shrotriya, P., Allameh, S.M. and Soboyejo, W.O. "On the evolution of surface morphology of polysilicon MEMS structures during fatigue," Mechanics of Mater. (2004) 36, 35-44

[86] Stolken, J.S. and Evans, A.G. "Elastic and tensile behavior of nanocrystalline copper and palladium," Acta Mater. (1998) 46, 5109-5115

[87] Treacy, M.M.J., Ebbesen, T.W. and Gibson, J.M. "Exceptionally high Young's modulus observed for individual carbon nanotubes," Nature (1996) 381, 678-680

[88] Poncharal, P., Wang, Z.L., Ugarte, D. and de Heer, W.A. "Electrostatic Deflections and Electromechanical Resonances of Carbon Nanotubes," Science (1999) 283, 1513-1516

[89] Huang, Y., Duan, X.F., Wei, Q.Q. and Lieber, C.M. "Directed assembly of one-dimensional nanostructures into functional networks," Science (2001) 291, 630-633

[90] Wong, E.W., Sheehan, P.E. and Lieber, C.M. "Nanobeam Mechanics: Elasticity, Strength, and Toughness of Nanorods and Nanotubes," Science (1997) 277, 1971-1975

[91] Walters, D.A. et al. "Elastic strain of freely suspended single-wall carbon nanotube ropes," Appl. Phys. Lett. (1999) 74, 3803-3805

[92] Shen, W.D., Jiang, B., Han, B.S. and Xie, S.S. "Investigation of the radial compression of carbon nanotubes with a scanning probe microscope," Phys. Rev. Lett. (2000) 84, 3634-3637

[93] Waters, J.F. et al. "Shell buckling of individual multiwalled carbon nanotubes using nanoindentation," Appl. Phys. Lett. (2005) 87, 103109

[94] Williams, P. A. et al. "Fabrication of nanometer-scale mechanical devices incorporating individual multiwalled carbon nanotubes as torsional springs" Appl. Phys. Lett. (2003) 82, 805

[95] Wang, M.S. et al. "In situ TEM measurements of the mechanical properties and behavior of WS 2 nanotubes," Nano Research (2008) 1, 22-31

[96] Hsin, C.L. et al. "Elastic properties and buckling of silicon nanowires," Adv. Mater. (2008) 20, 1–5

[97] Shan, Z.W., Mishra, R.K., Syed, A.S.A., Warren, O.L. and Minor, A.M. "Mechanical annealing and source-limited deformation in submicrometre-diameter Ni crystals," Nature Mater. (2008) 7, 115-119

[98] Richter, G. et al. "Ultrahigh strength single crystalline nanowhiskers grown by physical vapor deposition," Nano Lett. (2009) 9, 3048-3052

[99] D. Zhang, et al. "In situ tensile testing of individual Co nanowires inside a scanning electron microscope" Nanotechnology (2009) 20, 365706

[100] Zhu, Y., Moldovan, N. and Espinosa, H.D. "A microelectromechanical load sensor for in situ electron and x-ray microscopy tensile testing of nanostructures," Appl. Phys. Lett. (2005) 86, 013506

[101] Peng, B. et al. "Measurements of near-ultimate strength for multiwalled carbon nanotubes and irradiation-induced crosslinking improvements," Nature Nanotech. (2008) 3, 626 – 631

[102] Eppell, S., Smith, B., Kahn, H. and Ballarini, R. "Nano measurements with micro-devices: mechanical properties of hydrated collagen fibrils," J. the Royal Society Interface (2006) 3, 117-121,

[103] Haque, M.A. and Saif, M.T.A. "Deformation mechanisms in free-standing nanoscale thin films: A quantitative in situ transmission electron microscope study," Proc. Natl. Acad. Sci. U.S.A. (2004) 101, 6335–6340

[104] Lu, Y., Ganesan, Y. and Lou, J. "A Multi-step Method for In Situ Mechanical Characterization of 1-D Nanostructures Using a Novel Micromechanical Device," Exp. Mech. (2010) 50, 47-54

[105] Ganesan, Y. et al. "Development and Application of a Novel Microfabricated Device for the In Situ Tensile Testing of 1-D Nanomaterials," J. Microelectromechanical Systems (2010) 19, 675-682

[106] Guo, H. et al. "Tensile ductility and necking of metallic glass," Nature Mater. (2007) 6, 735-739

[107] Agrait, N., Rubio, G. and Vieira, S. "Plastic Deformation of Nanometer-Scale Gold Connective Necks," Phys. Rev. Lett. (1995) 74, 3995-3998

[108] Kizuka, T. "Atomistic visualization of deformation in gold," Phys. Rev. B. (1998) 57, 11158 - 11163

[109] Boyce, B.L., Huang, J.Y., Miller, D.C. and Kennedy, M.S. "Deformation and Failure of Small-scale Structure," JOM (2010) 62, 62-63

[110] Hirayama, H., Kawamoto, Y., Ohshima, Y. and Takayanagi, K. "Nanospot welding of carbon nanotubes," App. Phys. Lett. (2001) 79, 1169-1171

[111] Dong, L.X., Tao, X.Y., Zhang, L., Zhang, X.B. and Nelson, B.J. "Nanorobotic spot welding: Controlled metal deposition with attogram precision from copper-filled carbon nanotubes," Nano Lett. (2007) 7, 58–63

[112] Hyman, D. and Mehregany, M. "Contact physics of gold microcontacts for MEMS switches," IEEE Trans. on Components and Packaging Tech. (1999) 22, 357-364

[113] Chan, J.W. "Nano-wire Fabrication Using Anodic Aluminum Oxide as Template," MS thesis (1997), University of Toronto

[114] Bentley, A.K. "Template Synthesis and Magnetic Manipulation of Nickel Nanowires," Journal of Chemical Education (2005) 82, 765-768

[115] Yin, A. J., Li, J., Jian, W., Bennett, A. J. and Xu, J. M. "Fabrication of highly ordered metallic nanowire arrays by electrodeposition," Appl. Phys. Lett. (2001) 79, 1039-1041

[116] Liu, L., Lee, W., Huang, Z., Scholz, R. and Gosele, U. "Fabrication and characterization of a flow-through nanoporous gold nanowire/AAO composite membrane," Nanotechnology (2008) 19, 335604

[117] Xu, C.X., Su, J.X., Xu, X.H., Liu, P.P., Zhao, H.J., Tian, F. and Ding, Y. "Low temperature CO oxidation over unsupported nanoporous gold," J. Am. Chem. Soc. (2007) 129, 42–43

[118] Zhang, X., Li, D., Bourgeois, L., Wang, H. and Webley, P.A. "Direct Electrodeposition of Porous Gold Nanowire Arrays for Biosensing Applications," Chem. Phys. Chem. (2009) 10, 436 – 441

[119] Rouya, E., Reed, M., Kelly, R., Bart-Smith, H., Begley, M. and Zangari, G. "Synthesis of nanoporous gold structures via dealloying of electroplated Au-Ni alloy films," Int. 211th Electrochemical Society Transactions (2007) 6, 41–50

[120] Karim, S., Tomil-Molares, M. E., Balogh, A. G., Ensinger, W., Cornelius, T. W., Khan, E. U. and Neumann, R. "Morphological evolution of Au nanowires controlled by Rayleigh instability," Nanotechnology (2006) 17, 5954–5959

[121] Ji, C. and Searson P.C. "Synthesis and Characterization of Nanoporous Gold Nanowires," J. Phys. Chem. B (2003) 107, 4494-4499

[122] Khanal, B.P. and Zubarev E.R. "Purification of High Aspect Ratio Gold Nanorods: Complete Removal of Platelets," J. Am. Chem. Soc. (2008) 130, 12634–12635

[123] Laocharoensuk, R., Sattayasamitsathit, S., Burdick, J., Kanatharana, P., Thavarungkul, P. and Wang J. "Shape-Tailored Porous Gold Nanowires: From Nano Barbells to Nano Step- Cones," ACS Nano (2007) 1, 403–408

[124] Oldenburg, S. J., Jackson, J. B., Westcott, S. L. and Halas, N. J. "Infrared extinction properties of gold nanoshells," Appl. Phys. Lett. (1999) 75, 2897

[125] Bianca M. I., Zande, V.D., Bo1hmer, M.R., Fokkink, L.G. J. and Scholnenberger, C. "Aqueous Gold Sols of Rod-Shaped Particles," J. Phys. Chem. B (1997) 101, 852854

[126] Mitamura K. and Imae, T. "Functionalization of Gold Nanorods Towards Their Applications," Plasmonics (2009) 4, 23–30

[127] Plateau, J. "Experimental and theoretical researches on the figures of equilibrium of a liquid mass withdrawn from the action of gravity," Annu. Reports of the Smithsonian Inst. (1873) 270

[128] Rayleigh, L. "On the instability of jets," Lond. Math. Soc. Proc. (1878) 4-12

[129] Gurski, K. F. and McFadden, G. B. "The effect of anisotropic surface energy on the Rayleigh instability," Proc. R. Soc. London, A (2003) 459, 2575

[130] Shin, H.S., Yu, J. and Song, J.Y. "Size-dependent thermal instability and melting behavior of Sn nanowires," Appl. Phys. Lett. (2007) 91, 173106

[131] Lu, L., Chen, X., Huang, X. and Lu, K. "Revealing the Maximum Strength in Nanotwinned Copper," Science (2009) 323, 607-610

[132] Wu, X., Ma, E. and Zhu, Y.T. "Deformation defects in nanocrystalline nickel," J Mater Sci (2007) 42, 1427–1432

[133] Jing, G.Y. et al. "Surface effects on elastic properties of silver nanowires: contact atomic-force microscopy," Phys Rev B Condens Matter Mater Phys (2006) 73235409

[134] Ni, H., Li, X.D. and Gao, H.S. "Elastic modulus of amorphous SiO2 Nanowires," Appl. Phys. Lett. (2006) 88043108

[135] Boyce, B.L., Grazier, J.M. Buchheit, T.E. and Shaw, M.J. "Strength distributions in polycrystalline silicon MEMS," Journal of Microelectromechanical Systems (2007) 162, 179–190

[136] Naraghi, M., Chasiotis, L., Kahn, H., Wen, Y. and Dzenis Y. Novel method for mechanical characterization of polymeric nanofibers," Rev Sci Instrum (2007) 78085108

[137] Muhlstein, C.L., Stach, E.A. and Ritchie, R.O. "A reaction-layer mechanism for the delayed failure of micron-scale polycrystalline silicon structural films subjected to high-cycle fatigue loading," Acta Mater. (2002) 50, 3579–3595

[138] Kahn, H., Chen, L., Ballarini, R. and Heuer, A.H. Mechanical fatigue of polysilicon: effects of mean stress and stress amplitude," Acta Mater. (2006) 54, 667–678

[139] Ganesan ,Y., Lu, Y., Lu, H. and Lou, J. "In situ mechanical characterization of one dimensional nanoscale building blocks using novel microfabricated devices," IEEE-Nano Conf. Proc. (2008) 8, 783–786

[140] Durelli, A.J., Morse, S. and Parks, V. "The theta specimen for determining tensile strength of brittle materials," Mater. Res. Stand. (1962, ASTM) 2, 114–117

[141] Quinn, G.D. et al. "A novel test method for measuring mechanical properties at the small-scale: the theta specimen," Ceram. Eng. Sci. Proc. (2005) 262, 117–126

[142] Guckel, H., Burns, D., Rutigliano, C., Lovell, E. and Choi, B. "Diagnostic microstructures for the measurement of intrinsic strain in thin films," J. Micromech. Microeng. (1992) 2, 86–95

[143] Schneider, D. and Tucker, M.D. "Non-destructive characterization and evaluation of thin films by laser-induced ultrasonic surface waves," Thin Solid Films (1996) 290–291, 305–311

[144] Howatson, A.M., Lund, P.G. & Todd, J.D. Engineering Tables and Data (Chapman and Hall, London, 2nd, 1991), pp41

[145] Zhu, T., Li, J., Ogata, S. and Yip, S. "Mechanics of Ultra Strength Materials" MRS Bulletin (2009) 34, 167-172

[146] M.A. Haque, H.D. Espinosa and H.J. Lee, "MEMS for In Situ Testing-Handling, Actuation, Loading, and Displacement Measurements," MRS Bulletin (2010) 35, 375-381

[147] Ganesan, Y. et al."Effect of Nitrogen Doping on the Deformation and Failure Mechanisms of Individual Catalytically Grown Multi-Wall Carbon Nanotubes," ACS Nano (2010) 4, 7637-7643

[148] Nafari A. et al. "MEMS Sensor for In Situ TEM Atomic Force Microscopy," Journal of Microelectromechanical Systems (2008) 17, 328-333

[149] Agrawal, R., Peng, B. and Espinosa, H.D. "Experimental-Computational Investigation of ZnO nanowires Strength and Fracture," Nano Lett. (2009) 9, 4177-4183

[150] Zheng, H. et al. "Discrete Plasticity in Sub-10-nm-sized Gold Crystals," Nature Comm. 1, 144

[151] Rubio, G., Bahn, S.R., Agrait, N., Jacobsen, K.W. and Vieira, S. "Mechanical properties and formation mechanisms of a wire of single gold atoms," Phys. Rev. Lett. (2001) 87, 026101

[152] Ogata, S., Li, J., Hirosaki, N., Shibutani, Y. and Yip, S. "Ideal shear strain of metals and ceramics," Phys. Rev. B. (2004) 70, 104104

[153] Steinhardt, P. J., Nelson, D. R. and Ronchetti, M. "Bond-Orientational Order in Liquids and Glasses," Phys. Rev. B (1983) 28, 784

[154] Nose, S. A "Unified Formulation of the Constant Temperature Molecular-Dynamics Methods," J. Chem. Phys. (1984) 81, 511

[155] Daw, M. S. and Baskes, M. I. "Embedded-Atom Method - Derivation and Application to Impurities, Surfaces, and Other Defects in Metals," Phys. Rev. B (1984) 29, 6443

[156] Foiles, S. M., Baskes, M. I. and Daw, M. S. "Embedded-Atom-Method Functions for the Fcc Metals Cu, Ag, Au, Ni, Pd, Pt, and Their Alloys," Phys. Rev. B (1986) 33, 7983

[157] Cai, J. and Ye, Y. Y. "Simple analytical embedded-atom-potential model including a long-range force for fcc metals and their alloys," Phys. Rev. B (1996) 54, 8398

[158] Deng, C. and Sansoz, F. "Enabling Ultrahigh Plastic Flow and Work Hardening in Twinned Gold Nanowires" Nano Lett. (2009) 9, 1517-1522

[159] Lagos, M. J., Sato, F., Galvao and D. S., Ugarte, D. "Mechanical Deformation of Nanoscale Metal Rods: When size and shape matters," (2009) arXiv:0910.4139v1

[160] Song, J. and Srolovitz, D. J. "Effect of temperature on single asperity contact and separation in Au," Scripta Mater. (2007) 57, 885

[161] Song, J. and Srolovitz, D. J. "Mechanism for material transfer in asperity contact," J Appl. Phys. (2008) 104, 124312

[162] Song, J. and Srolovitz, D. J. "Atomistic simulation of multicycle asperity contact," Acta Mater. (2007) 55, 4759

[163] Thompson N. "Dislocation Nodes in Face-Centred Cubic Lattices," Proceedings Proc. Phys. Soc. B (1953) 66, 481-492

[164] Opening remarks. J. Am. Welding Soc. (1919) 1, 3

[165] Freitas, R. A. and Gilbreath, W. P. (eds) "Advanced Automation for Space Missions: Proceedings of the 1980 NASA/ASEE Summer Study," (NASA, 1980) Appendix 4C.1.

[166] Ferguson, G. S., Chaudhury, M. K., Sigal, G. B. and Whitesides, G. M. "Contact adhesion of thin gold films on elastomeric supports: cold welding under ambient conditions," Science (1991) 253, 776–778

[167] Kim, C., Burrows, P. E. & Forrest, S. R. "Micropatterning of organic electronic devices by cold-welding," Science (2000) 288, 831–833

[168] Jin, C., Suenaga, K. and Iijima, S. "Plumbing carbon nanotubes," Nature Nanotech. (2008) 3, 17–21

[169] Wang, M., Wang, J., Chen, Q. and Peng, L. M. "Fabrication and electrical and mechanical properties of carbon nanotube interconnections," Adv. Funct. Mater. (2005) 15, 1825–1831

[170] Madsen, D. N. et al. "Soldering of nanotubes onto microelectrodes," Nano Lett. (2003) 3, 47–49

[171] Wu, Y. and Yang, P. "Melting and welding semiconductor nanowires in nanotubes," Adv. Mater. (2001) 13, 520–523

[172] Dong, L., Tao, X., Zhang, L., Zhang, X. & Nelson, B. J. "Nanorobotic spot welding: controlled metal deposition with attogram precision from copper-filled carbon nanotubes" Nano Lett. (2007) 7, 58–63

[173] Misra, A. and Daraio, C. "Sharp carbon-nanotube tips and carbon-nanotube soldering irons," Adv. Mater. (2008) 20, 1–4

[174] Rodrı´guez-Manzo, J. A. et al. "Heterojunctions between metals and carbon nanotubes as ultimate nanocontacts," Proc. Natl Acad. Sci. USA (2009) 106, 4591–4595

[175] Xu, S. et al. "Nanometer-scale modification and welding of silicon and metallic nanowires with a high-intensity electron beam," Small (2005) 1, 1221–1229

[176] Tohmyoh, H., Imaizumi, T., Hayashi, H. and Saka, M. "Welding of Pt nanowires by Joule heating," Scripta Mater. (2007) 57, 953–956

[177] van Huis, M. A. et al. "Low-temperature nanocrystal unification through rotations and relaxations probed by in situ transmission electron microscopy" Nano Lett. (2008) 8, 3959–3963

[178] Kizuka, T., Yamada, K., Deguchi, S., Naruse, M. and Tanaka, N. "Time-resolved high-resolution electron microscopy of atomic scale solid-state direct bonding of gold tips," J. Electron Microsc. (1997) 46, 151–160

[179] Tohmyoh, H. "A governing parameter for the melting phenomenon at nanocontacts by Joule heating and its application to joining together two thin metallic wires" J. Appl. Phys. (2009) 105, 014907

[180] Kim, S. J. and Jang, D. J. "Laser-induced nanowelding of gold nanoparticles," Appl.Phys. Lett. (2005) 86, 033112

[181] Moskalenko, A. V., Burbridge, D. J., Viau, G. & Gordeev, S. N. "Electron-beaminduced welding of 3D nano-objects from beneath," Nanotechnology (2007) 18, 025304

[182] Peng, Y., Cullis, T. and Inkson, B. "Bottom-up nanoconstruction by the welding of individual metallic nanoobjects using nanoscale solder," Nano Lett. (2009) 9, 91–96

[183] Gu, Z., Ye, H., Smirnova, D., Small, D. and Gracias, D. H. "Reflow and electrical characteristics of nanoscale solder" Small (2006) 2, 225–229

[184] Ramsperger, U., Uchihashi, T. and Nejoh, H. "Fabrication and lateral electronic transport measurements of gold nanowires," Appl. Phys. Lett. 78, 85–87 (2001)

[185] Calleja, M., Tello, M., Anguita, J., Garcia, F. and Garcia, R. "Fabrication of gold nanowires on insulating substrates by field-induced mass transport" Appl. Phys. Lett. (2001) 79, 2471–2473

[186] Song, J. H., Wu, Y., Messer, B., Kind, H. and Yang, P. "Metal nanowire formation using Mo3Se3 as reducing and sacrificing templates. J. Am. Chem. Soc. (2001) 123, 10397–10398

[187] Jose´-Yacaman, M. et al. "Surface diffusion and coalescence of mobile metal Nanoparticles," J. Phys. Chem. B (2005) 109, 9703–9711

[188] Rez, P. and Glaisher, R. W. "Measurement of energy deposition in transmission electron microscopy," Ultramicroscopy (1991) 35, 65–69

[189] Sanders, D. E. and DePristo, A. E. "Predicted diffusion rates on fcc (001) metal surfaces for adsorbate/substrate combinations of Ni, Cu, Rh, Pd, Ag, Pt, Au." Surf. Sci. (1992) 260, 116–128

[190] Cho, K. S., Talapin, D. V., Gaschler, W. and Murray, C. B. "Designing PbSe nanowires and nanorings through oriented attachment of nanoparticles," J. Am. Chem. Soc. (2005) 127, 7140–7147

[191] Zhong, Z., Wang, D., Cui, Y., Bockrath, M. W. and Lieber, C. M. "Nanowire crossbar arrays as address decoders for integrated nanosystems" Science (2003) 302, 1377–1379

[192] Whang, D., Jin, S., Wu, Y. and Lieber, C. M. "Large-scale hierarchical organization of nanowire arrays for integrated nanosystems," Nano Lett. (2003) 3, 1255–1259

[193] Huo, F. et al. "Polymer pen lithography," Science (2008) 321, 1658–1660